ISSN en trámite

Geofísica Internacional

Revista Trimestral Publicada por el Instituto de Geofísica de la Universidad Nacional Autónoma de México

México
Volume 56 Number 4
October - December
2017

— Geofísica Internacional —

GEOFÍSICA INTERNACIONAL, Año 56, Vol. 56, Núm. 4, octubre - diciembre de 2017 es una publicación trimestral, editada por la Universidad Nacional Autónoma de México, Ciudad Universitaria, Alcaldía Coyoacán, C.P. 04150, Ciudad de México, a través del Instituto de Geofísica, Circuito de la Investigación Científica s/n, Ciudad Universitaria, Alcaldía Coyoacán, C.P. 04150, Ciudad de México, Tel. (55)56 22 41 15. URL: http://revistagi.geofisica.unam.mx, correo electrónico: revistagi@igeofisica.unam.mx. Editora responsable: Andrea Rostan Robledo. Certificado de Reserva de Derechos al uso Exclusivo del Título: 04-2022-081610251200-102, ISSN: en trámite, otorgados por el Instituto Nacional del Derecho de Autor (INDAUTOR). Responsable de la última actualización Saúl Armendáriz Sánchez, Editor Técnico. Fecha de la última modificación: 30 de septiembre 2017, Circuito de la Investigación Científica s/n, Ciudad Universitaria, Alcaldía Coyoacán, C.P. 04150, Ciudad de México.

Geofísica Internacional

Vol. 56, Núm. 4, octubre-diciembre de 2017

Contents

Hydraulic conductivities identification via Ensemble Kalman Filtering with transformed data considering the risk of systematic bias.
F. Vázquez-Guillén, Guichard Auvinet

317

The effect of salinity and gas saturation of a geothermal fluid on the reservoir permeability reduction.
Juán Flores, Onésimo Meza, Sara L., Alfonso Aragón

335

DC resistivity investigation in a fractured aquifer system contaminated by leachate from an old dump.
César Augusto Moreira, Carolina Gonçalves Leandro, Camila Trindade Lopes, Lenon Melo Ilha

345

Effects of the soil properties on the sea pressure profile due to seismic motions.
Alejandro Rodríguez-Castellanos, Rafael Ávila-Carrera, Ernesto Pineda-León, Víctor Martínez-Calzada, Francisco José Sánchez-Sesma

359

A Simplified Method to Invert Slow Slip Events: Examples for the 2002, 2006 and 2014 events in Guerrero, Mexico.
Oscar A. Castro Artola, Arturo Iglesias, Vladimir Kostoglodov, Sara I. Franco-Sánchez, Vala Hjörleifsdóttir, Enrique Cabral-Cano, Miguel A. Santoyo

377

Geofísica Internacional (2017) 56-4: 317-333

Original paper

Hydraulic conductivities identification via Ensemble Kalman Filtering with transformed data considering the risk of systematic bias

F. Vázquez-Guillén*, Guichard Auvinet

Received: February 02, 2016; accepted: September 12, 2017; published on line: October 01, 2017

Resumen

En hidrología subterránea, el conjunto de filtros Kalman (EnKF) se acopla con modelos del flujo y transporte de agua subterránea para resolver el problema inverso. Se han propuesto varias extensiones del EnKF para mejorar su desempeño al tratar con campos aleatorios no multi-gaussianos de la conductividad hidráulica. Una de esas variantes es el EnKF con transformación de datos (tEnKF), el cual utiliza la anamorfosis gaussiana dentro de una etapa de condicionamiento. Aunque esta transformación se ha utilizado en el pasado para identificar conductividades hidráulicas, estudios previos han ignorado el riesgo de introducir un sesgo sistemático en la evolución espaciotemporal del campo de la carga hidráulica durante las etapas de pronostico que las etapas de condicionamiento podrían no corregir conforme trascurre el tiempo. Este artículo propone que la aplicación del tEnKF en medios porosos aleatorios generados sintéticamente debe tener en cuenta este riesgo incorporando en el conocimiento *a priori* una estructura de correlación multi-gaussiana para las conductividades y adoptando un campo de referencia con estructura de correlación asimétrica. Como un ejemplo de esta aplicación, en este artículo se identifican conductividades hidráulicas utilizando el tEnKF resolviendo un problema de flujo monofásico, unidimensional, en un medio poroso aleatorio continuo. Se utilizan conceptos comunes en geoestadística para explicar las hipótesis en las que se basan el EnKF y el tEnKF y también para establecer un vínculo claro entre el tEnKF y la simulación estocástica de campos aleatorios condicionales.

Key words: Simulación estocástica, campos aleatorios condicionales, anamorfosis gaussiana, problema inverso, campos aleatorios no multi-gaussianos.

Abstract

In subsurface hydrology, Ensemble Kalman Filtering (EnKF) has been coupled with groundwater flow and transport models to solve the inverse problem. Several extensions of the EnKF have been proposed to improve its performance when dealing with non-multi-Gaussian random field models of the hydraulic conductivity. One such variant is the EnKF with transformed data (tEnKF), which uses Gaussian anamorphosis within a conditioning step. Although this transformation has been used in the past to identify hydraulic conductivities, previous studies have ignored the risk of introducing a systematic bias in the spatiotemporal evolution of the hydraulic head field during the forecast steps that the update steps may not correct over time. This paper proposes that in order to evaluate the performance of tEnKFs, applications in synthetically generated random porous media should take into account this risk by incorporating prior knowledge with a multi-Gaussian conductivity correlation structure, and by adopting a reference field with asymmetric correlation structure. As an example of this application, hydraulic conductivities using the tEnKF were identified by solving a one-dimensional, single phase flow problem in a continuous random porous medium. Common concepts in Geostatistics are used to explain the hypothesis underlying both EnKF and tEnKF and to establish a clear link between the tEnKF and the stochastic simulation of conditional random fields.

Palabras clave: Stochastic simulation, conditional random fields, Gaussian anamorphosis, inverse problem, Non multi-Gaussian random fields.

F. Vázquez-Guillén*
G. Auvinet
Coordinación de Geotecnia y Estructuras
Instituto de Ingeniería
Universidad Nacional Autónoma de México
Ciuidad Universitaria
Delegación Coyoacán 04510
México CDMX, México.
Corresponding author: fvazquezg@exii.unam.mx

Introduction

Groundwater modeling as a tool for sustainable development and utilization of groundwater resources in land subsidence studies requires knowledge of the hydrogeologic properties of the medium. A number of studies have shown that parameters such as hydraulic conductivity and porosity of porous media exhibit spatial variations. Most of the times, these variabilities can only be determined at few and sparse locations. Thus, there is uncertainty in the characterization of the spatial variability of those properties. Owing to this uncertainty, predictions conducted with groundwater flow models are also uncertain. To make plausible predictions and reduce the associated uncertainty, stochastic inverse modeling techniques are frequently applied. These techniques allow the identification of parameters and the quantification of parameter and prediction uncertainty consistent with the measured data and the groundwater flow model.

In subsurface hydrology, hydraulic conductivity fields are often characterized assuming that its spatial variability can be interpreted as a realization of a random field model (Dagan, 1989; Gelhar, 1993). The parameterization of the random field is obtained through the observations of the realization itself assuming the field is ergodic (Deutsch and Journel, 1992; Chilés and Delfiner, 1999). Then, inferences at unobserved locations and the uncertainty of these inferences are determined on the basis of the direct observations by either estimation or simulation techniques (e.g. Journel and Huijbregts, 1978; Chilés and Delfiner, 1999). While estimation techniques provide one single "best" estimate of the hydraulic conductivity field, simulation techniques yield multiple realizations of that field (Journel and Huijbregts, 1978). In order to reduce the uncertainty in the inference of the hydraulic conductivity field, indirect observations of it, e.g., of hydraulic heads, are also taken into account in these tasks by solving the typical inverse problem of hydrogeology (Chilés and Delfiner, 1999). Other informative variables such as flow rates and species concentrations may also be incorporated in the inference process to further constrain the spatial fluctuations of the conductivities. Although solutions to the inverse problem lead to hydraulic conductivity fields which are compatible with the measured hydraulic head data, it is recognized that there are an infinite number of other conductivity fields which may also match the same hydraulic head data (RamaRao *et al*., 1995). The inverse problem is therefore ill-posed and a unique, exact solution is generally not available. Instead, a solution which coincides with the observations is commonly sought (Tarantola, 2005).

The inverse problem can be solved under steady conditions or under transient conditions using estimation or simulation techniques (Gómez-Hernández and Wen, 1994; Chilés and Delfiner, 1999). A comprehensive review of the evolution of several methods for solving the stochastic inverse problem in hydrogeology has been presented elsewhere (Zhou *et al*. 2014). Among these approaches, simulation-based inversion techniques are often preferred over estimation-based inversion techniques because it has been proven that the single "best" estimate provided by the latter does not capture the range of variability of real fields of conductivities. As a result, flow and transport predictions conducted in these fields are very poor (Gómez-Hernández and Wen, 1994). The most widely accepted simulation-based inversion techniques in groundwater modeling use the Monte Carlo (MC) method. Within the MC framework, the available observations of the state variables are integrated into a prior random field of conductivities through an iterative procedure to obtain a posterior random field of conductivities expressed as a set of conditional simulations. Examples of such kinds of approaches are: the self-calibration method (Sahuquillo *et al*., 1992; Gómez-Hernández *et al*., 1997), the pilot-point method (RamaRao *et al*., 1995), the Markov-Chain MC method (Oliver *et al*., 1997), the gradual deformation method (Hu, 2000; Capilla and Llopis-Albert, 2009; Hu *et al*., 2013) and the random mixing method (Bárdossy and Hörning, 2016). One common characteristic to all of these MC-based inversion methods is that they are formulated as optimization problems where the unknown parameter field is represented by the nodes of a mesh. Thus, the use of dimensional reduction techniques is indispensable in large dimensional problems. The main difference among the approaches is the way the optimization problem is solved.

An alternative MC-based inversion technique that can be used to integrate available observations of the hydraulic head into a prior random field model of conductivities is the Ensemble Kalman Filter (EnKF). In this approach, the observations are integrated sequentially in time using the groundwater model itself to evolve the hydraulic head field in a physically plausible manner (Katzfuss *et al*., 2016). The EnKF was developed by Evensen (1994) as an extension of the Kalman Filter (KF) (Kalman, 1960) to deal with non-linear

systems. The main difference between EnKF and KF is that the former uses an ensemble representation for the state variables from which any statistical moment can be calculated whenever it is needed. Instead of using the MC method, earlier extensions of the KF used perturbation theory to handle non-linear dynamics. This is the case of the Extended KF (EKF) (Evensen, 1992; Leng and Yeh, 2003). However, it has been found that the EnKF outperformed the EKF, especially in highly non-linear systems (Miller *et al*., 1999; Reichle *et al*., 2002). The EnKF differs from other MC-based filters, such as particle filters, in the process by which the observations are integrated into the prior random field model.

The EnKF procedure consists of two main steps. The first is the forecast step, which uses MC sampling to propagate the uncertainty in the hydraulic conductivity field through the groundwater model to approximate the spatiotemporal evolution of the hydraulic head field at the time the observations are available. The second is the update step that integrates the measured hydraulic head data into the prior random field model of conductivities by conditioning each prior realization to the available observations. The conditioning process is performed only on the basis of the available data at the time of analysis using a linear estimation technique. Thus, only the mean, auto-covariance and cross-covariance functions are used when computing the posterior random field of conductivities. This strategy lends the scheme computational efficiency and makes it suitable for large dimensional problems, yet the forecast step may still be highly demanding in terms of computation. Since the conditional simulations thus obtained are consistent with the system dynamics, predictions of response variables and an investigation of the uncertainty of these predictions can also be conducted simultaneously.

The EnKF only converges to an optimal solution when the random fields involved are multi-Gaussian and when the functional relationship between state and parameter variables is linear. Due to the non-linearity of the groundwater equations, it seems reasonable to expect that state fields will be non multi-Gaussian even in multi-Gaussian parameter fields. Thus, assuming joint multi-Gaussian distributions between conductivities and heads is often not correct in practice. Moreover, in multi-Gaussian random fields the spatial correlation structure is symmetric; i.e., the values at opposite percentiles with respect to the mean present exactly the same spatial correlation structure (Journel and Deutsch, 1993; Journel and Zhang, 2006). The highest continuity is observed at mean values and the extreme high/low values appear as isolated clusters. As a result, connected paths of extreme values do not occur in multi-Gaussian random fields (Gómez-Hernández and Wen, 1998; Knudby and Carrera, 2005). On the contrary, field evidence suggests that the patterns of spatial variability in natural soil formations differ significantly from such multi-Gaussian dependence characteristics. Journel and Alabert (1989) found stronger spatial correlation structures at low values than at high values in field measurements of air permeability taken on a vertical slab of Berea sandstone; this stronger correlation was even stronger than that imposed by a multi-Gaussian random field model. Asymmetric correlation structures have also been found in conductivity fields with relatively small heterogeneity (Haslauer *et al*., 2012). Thus, natural porous media seem to be non multi-Gaussian with respect to their spatial distribution of conductivities independently of their degree of heterogeneity.

Several extensions of the EnKF have been examined in the last decade in order to achieve a more versatile tool capable of handling non multi-Gaussian random field models in parameter identification problems. Sun *et al*. (2009) reformulated the update step of the EnKF using Gaussian mixture models and clustering techniques. Sarma and Chen (2009) developed a generalization of the EnKF based on kernel principal component analysis. Emerick (2017) presented an investigation of the performance of different principal component analysis-based approaches. Bertino *et al*. (2003) modified the update step of the EnKF by applying Gaussian transformations. The advantages of this last extension compared to the classical EnKF method were confirmed in several studies (Zhou *et al*. 2011; Li *et al*. 2012; Schöniger *et al*. 2012; Erdal *et al*. 2015). One common characteristic to all of these EnKF-based methods is the use of auto-covariance and cross-covariance functions as unique descriptors of the spatial dependence at each update step. Unlike these approaches, Zhou *et al*. (2012) developed the so-called Ensemble PATtern matching method (EnPAT) based on multiple-point geostatistical simulation techniques which use multiple-point covariance functions rather than traditional two-point covariance functions to determine the spatial correlations. Extensions of this approach were developed later (Li *et al*. 2013, 2014, 2015). Although the EnPAT method outperforms the classical EnKF and eliminates the multi-Gaussian assumption implicit in the update step of the latter (Li *et al*. 2015), it strongly

relies on the concept of training image; i.e. a conceptual model of the geological structure of the formation under study, the construction of which can be problematic, especially in 3D applications, and the benefit of which is more evident in fluvial deposits than in other type of geologic formations.

The EnKF with Gaussian transformations (tEnKF) has been particularly well accepted in several geophysical areas (Bertino *et al*. 2003; Simon and Bertino, 2009, 2012; Béal *et al*. 2010; Zhou *et al*. 2011; Li *et al*. 2012; Schöniger *et al*. 2012; Xu *et al*. 2013; Erdal *et al*. 2015; Zovi *et al*. 2017). In subsurface hydrology, it has been applied to the identification of the hydraulic conductivity of synthetically generated channelized aquifers that display the same asymmetry as the prior random field model (Zhou *et al*. 2011; Li *et al*. 2012; Xu *et al*. 2013). Thus, the domain under study has the same spatial variability characteristics as those of the set where the spatiotemporal evolution of the hydraulic head field is sought. As a result, the performance of tEnKF is promising because the deviations from the reference field are then corrected, up to a certain extent, with the update steps. However, these studies do not take into account the risk of introducing a systematic bias in the spatiotemporal evolution of the hydraulic head field during the forecast steps that the update steps may not correct over time. While they attribute the promising performance of tEnKF to Gaussian transformations, they disregard the implications of the information incorporated in the prior conductivity fields. This information should be taken into account to explain the performance of the tEnKF because the update step remains suboptimal and is performed under the multi-Gausian model which is unable to capture channelized structures with the covariance function as the sole descriptor of an evolving spatial dependence. The absence of knowledge about higher order moments of the parameter field inevitably implies a risk of introducing such systematic bias.

This paper proposes that in order to evaluate the performance of tEnKFs, applications in synthetically generated random porous media should take into account the risk of systematic bias by incorporating prior knowledge with a multi-Gaussian conductivity correlation structure, and by considering the spatial distribution of the hydraulic conductivity of a reference field as having an asymmetric correlation structure. This view of the problem follows the idea of Kerrou *et al*. (2008), yet differs significantly from its mathematical framework and scope. Our experimental setting is closer to a common situation found in practice where one has access to a rough approximation to the mean, variance and auto-covariance function of the real field, but the asymmetry of the spatial correlation structure of that field is unknown. As an example of this application, this paper identifies hydraulic conductivities using the tEnKF by solving a one-dimensional, single phase flow problem in a continuous random porous medium. To explain the hypothesis underlying both EnKF and tEnKF and to establish a clear link between the tEnKF and the stochastic simulation of conditional random fields, common concepts in Geostatistics are used. Ultimately, the aim of this paper is to motivate further discussions about the benefit of incorporating transient hydraulic head responses in the identification of hydraulic conductivity fields subject to this kind of constraint and about further potential improvements to the update step of the EnKF to overcome the multi-Gaussian assumption.

Groundwater flow equations

In this section, the dynamic model describing single-phase fluid flow in a one-dimensional, vertical, fully saturated porous medium with spatially variable hydraulic conductivity is analyzed:

$$\frac{\partial}{\partial x}\left[K_s(\mathbf{x})\frac{\partial H}{\partial x} \right] = S_s \frac{\partial H}{\partial t} \qquad (1)$$

subject to initial and boundary conditions

$$H_{t=0} = h_0,\ H_{\Gamma_D} = h_1 \qquad (2)$$

where H is the hydraulic head [L] in the domain Ω, $\mathbf{x}$ is the spatial coordinate ($\mathbf{x} = x_3$ [L], where x_3 represents the vertical coordinate which is positive upward), $K_S(\mathbf{x})$ is the saturated hydraulic conductivity [L/T], S_S is the specific storage [L^{-1}], h_0 represents the initial head and h_1 the prescribed head at Dirichlet boundary Γ_D.

In the present example, specific storage as well as initial and boundary conditions are treated as deterministic constants. An error-free dynamic model is also assumed. Hence, the model prediction is only affected by the uncertainty in $K_S(\mathbf{x})$. To model this uncertainty, a stationary random field model is adopted. In such an approach, $Y(\mathbf{x})$ defines the collection of n continuous scalar random variables of the natural logarithm of the saturated hydraulic conductivity, i.e. $Y(\mathbf{x}) = \ln(Y_S(\mathbf{x}))$ indexed at the spatial locations $\mathbf{x}$ in the domain Ω_x with $\Omega_x \in \Re^1$. Since $K_S(\mathbf{x})$ is a random field, equation (1)

becomes a stochastic differential equation and the flow response H becomes a spatiotemporal random field. $K_S(\chi, t)$ is defined as the collection of N continuous scalar random variables of the hydraulic head indexed at the spatial locations χ in the domain Ω_χ with $\Omega_\chi \in \Re^1$ and times $t \in \{0, 1, 2,...\}$. Although $Y(\mathbf{x})$ is assumed as stationary, $H(\chi, t)$ will be non-stationary in space and time because the domain is bounded (Zhang, 2002). In the following formulations, an ensemble interpretation of both random fields is applied.

The EnKF method

In this section, an alternative formulation for parameter estimation of the EnKF based on common concepts in Geostatistics is presented.

Forecast step

The EnKF uses MC sampling to approximate $H(\chi, t)$ assuming that it evolves like a first order Markov process (Evensen, 2003), i.e. $P[H(\chi, t)]|, H(\chi, t-1), H(\chi, t-2),...] = P[H(\chi, t)]|, H(\chi, t-1)]$. Hence, only the most recent past determines the multivariate conditional Cumulative Distribution Function (CDF) of $H(\chi, t)$ given the whole past. This simplified evolution of $H(\chi, t)$ can be written as:

$$H\left(\chi, t\right) = \Im\left(H\left(\chi, t-1\right); \theta\right) \qquad (3)$$

where $\Im(\cdot)$ is a forecast operator representing the dynamic model, i.e. the behavior of the state process as time evolves, and θ is a vector of parameters involved in that description. For example, to determine $H(\chi, t=1)$, it is necessary to specify initial and boundary conditions, a prior ensemble of saturated hydraulic conductivity fields, and the specific storage coefficient. The information incorporated in the prior conductivity fields is thus a key issue in the performance of EnKFs. Finally, note that in equation (3) there are no assumptions about the type of CDF of the parameters or about the linearity of the considered dynamic model.

Update step

The update step of the EnKF approximates the univariate conditional CDFs of $Y(\mathbf{x})$ given that N_h observations of $H(\chi, t=1)$ are known, i.e. $F_{Y_i|H_1,...,H_{N_h}}(y_i; \mathbf{x}_i|D) = P[Y(\mathbf{x}_i) \leq y_i | H(\chi_\alpha, t=1) = h_{\alpha, t=1}, t=1, \alpha=1,... N_h]$

by conditioning each realization of $Y(\mathbf{x})$ under the hypothesis that the joint multivariate distributions of $Y(\mathbf{x})$ and $H(\chi, t = 1)$, as well as the multivariate distributions of $H(\chi, t=1)$ and $Y(\mathbf{x})$, are Gaussian. Thus, the problem is reduced to the stochastic simulation of one conditional random field assuming a multi-Gaussian model. This update step is performed according to:

$$\mathbf{U}_t^u = \mathbf{U}_0 + \mathrm{K}_t[\mathbf{Z}_t - \mathbf{H}_t^f] \qquad (4)$$

where $\mathbf{U}_t^u = [\hat{y}(\mathbf{x}_1), \hat{y}(\mathbf{x}_2),..., \hat{y}(\mathbf{x}_n)]^{\mathrm{T}}$ is an n-dimensional vector of updated realizations of the log-conductivity at $t=1$, $\mathbf{U}_0 = [y(\mathbf{x}_1), y(\mathbf{x}_2),..., y(\mathbf{x}_n)]^{\mathrm{T}}$ is an n-dimensional vector of simulated realizations of the log-conductivity (realizations *a priori*), $\mathbf{Z}_t = [h_{1,t=1}, h_{2,\ t=1},..., h_{N_h,t=1}]^T$ is the vector of observations with dimension N_h, $\mathbf{H}_t^f = [h(\chi_1, t=1), h(\chi_2, t=2),..., h(\chi_{N_h}, t=1)]^{\mathrm{T}}$ is a reduced vector of forecasted states (realizations of the hydraulic head at the locations of the observations) of dimension N_h, and $\mathbf{K}_t = [\lambda_1(\mathbf{x}_1), \lambda_1(\mathbf{x}_2),..., \lambda_1(\mathbf{x}_{N_h}); ...\lambda_n(\mathbf{x}_1), \lambda_n(\mathbf{x}_2),..., \lambda_n(\mathbf{x}_{N_h})]$ is a matrix of dimension nxN_h called "Kalman gain", with $\lambda_l(\mathbf{x}_\alpha)$ representing the relative importance of the observations in estimating the value of $Y(\mathbf{x}_i)$. These weighting functions are solutions of the following systems of linear equations:

$$\sum_{l=1}^{n}\sum_{\alpha=1}^{N_h} \lambda_l(\chi_\alpha) C_H(s, \tau) = C_{YH}(s, \tau) \qquad (5)$$

where $C_H(s, \tau)$ represents the spatiotemporal auto-covariance functions between hydraulic heads with $s=(\chi_\alpha, \chi_j)$ for $j = 1,..., N$ and $\tau=(t=1, t=1)$, and $C_{YH}(s, \tau)$ represents the spatiotemporal cross-covariance functions between log-conductivities and hydraulic heads at $s=(\mathbf{x}, \chi_j)$ with $\tau=(t=0, t=1)$. In the EnKF, both covariance functions are determined statistically over the ensemble of realizations of $Y(\mathbf{x})$ and $H(\chi, t=1)$. These covariance functions are therefore empirical, but on average over several realizations, they can be expected to lead to positive definite matrices and may be used directly without modeling. On the other hand, given their statistical origin, they lead to the "filter inbreeding effect", i.e. the underestimation of variance over time after several update steps (Hendricks and Kinzelbach, 2008). As a result, the final updated realizations may look almost identical to each other and are virtually equal to the ensemble mean (Zhou *et al*., 2011). Xu *et al*. (2013) showed, through hydrogeology applications, that filter inbreeding can be reduced with covariance localization and covariance inflation techniques. Alternative strategies for reducing this problem were presented earlier by Hendricks

and Kinzelbach (2008). The implementation of these techniques in the present application is beyond the scope of this paper.

In most applications of the EnKF method, the observations are affected by random errors which are characterized by a normal distribution with zero mean and a diagonal covariance function which represents that, at different measurement locations, these errors are also independent. Adding random errors to the observations serves the purpose of increasing the ensemble variance over time (Burgers *et al*., 1998). Hence, considering noisy observations contributes somehow to the reduction of the filter inbreeding effect. Some authors also find it useful to add random errors to the observations to stabilize the inversion of the covariance functions and avoid small singular values dominating the solution. Other authors address this last problem formally by means of the Tikhonov regularization functional (e.g. Johns and Mandel, 2008; Elsheikh *et al*. 2013). In the present paper, extensive numerical experiments performed by the authors showed that the Gaussian transformations presented in the following section contribute significantly to the stabilization of the inversion of the covariance functions. Thus, adding random errors to the observations for this purpose is not necessary within the Gaussian space. Moreover, systematic errors affecting the observations could also be considered in the update step because instruments may induce biases which introduce fictitious correlations between variables. Furthermore, errors might not be Gaussian. Therefore, error-free measurements were considered in this study. In future investigations, it will be important to address the evaluation of the effect of both types of errors on the spatial distribution of the uncertainty and its interpretation, as well as the quantitative impact of adding white noise to the observations on the filter inbreeding effect.

The EnKF method with transformed data (tEnKF)

There are two additional steps and one modified update step that have to be implemented in the EnKF method with transformed data (tEnKF). These three steps are described in this section using common concepts in Geostatistics. Then, some useful formulas for post-processing the results and recommendations for the numerical implementation of the tEnKF are presented.

Gaussian transformation step

Under the multi-Gaussian hypothesis implicit in the classical EnKF procedure, the univariate conditional CDF of $Y(\mathbf{x})$, given that N_h observations of $H(\chi_1, t{=}1)$ are known, will be Gaussian with conditional expectation and conditional variance given by the simple Kriging (cokriging) estimates (Journel and Huijbregts, 1978). However, for the Kriging variance to be an unbiased estimate, both $Y(\mathbf{x})$ and $H(\chi_1, t{=}1)$ have to be zero-mean Gaussian random fields (Shinozuka and Zhang, 1996). Bertino *et al*. (2003) realized this situation and therefore proposed to apply Gaussian transformations, at least locally, to both random fields. The Gaussian transformation maps non-Gaussian distributed random variables into Gaussian random variables (with zero mean and unity variance) according to:

$$\tilde{Y}(\mathbf{x}_i) = \Phi^{-1}(F_Y(y; \mathbf{x}_i)) \qquad (6)$$

$$\tilde{H}(\mathbf{x}_i, t{=}1) = \Phi^{-1}(F_H(h; \mathbf{x}_i; t{=}1)) \qquad (7)$$

where $\Phi^{-1}(\cdot)$ is the inverse of the univariate Gaussian distribution function, and $F_Y(y; \mathbf{x}_i)$ and $F_H(h; \mathbf{x}_i; t{=}1)$ are the local distribution functions of $Y(\mathbf{x})$ and $H(\chi_1, t{=}1)$, respectively. In the tEnKF the empirical versions of these distribution functions are used. The empirical distribution function is defined by $F_n(c) = 1/n_r \sum_{j=1}^{n_r} I\left\{C_j \le c\right\}$, where $I\{\cdot\}$ stands for an indicator random variable that takes a value equal to 1 whenever its argument is true, and 0 otherwise with n_r equal to the number of log-conductivity fields. It should be recalled that the empirical distribution function will converge to its theoretical counterpart as the number of realizations in the ensemble tends to infinity (Billingsley, 1995). The variables with the tilde in equations 6-7 symbolize the transformed random variables. In addition to the transformations expressed by these equations, a standardization of the observations at each location have to be applied. The function relating y to $\tilde{y}$ or h to $\tilde{h}$ in the x-y Cartesian plane, is called the Gaussian anamorphosis function and was introduced by Rosenblatt (1952) (Figure 1).

Note that since only marginal transformations are applied, the joint multivariate distributions of $Y(\mathbf{x})$ and $H(\chi_1, t{=}1)$, as well as the multivariate distributions of $H(\chi_1, t{=}1)$ and $Y(\mathbf{x})$, are not modified.

Modified update step

Once the transformations described in the previous section have been applied, the update step of the tEnKF method can now be written in terms of the anamorphosed variables:

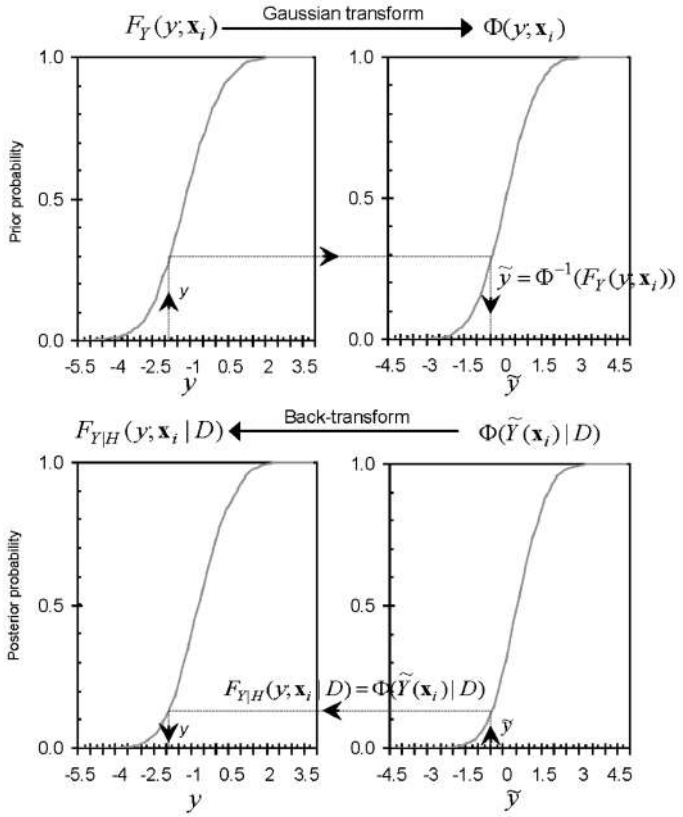

Figure 1. Transformation step of the EnKF method: a) Gaussian transformation process, b) Back-transformation process.

$$\tilde{U}_t^u = \tilde{U}_0 + \left[\tilde{K}_t \quad \tilde{Z}_t - \tilde{H}_t^f\right] \tag{8}$$

where the weighting functions $\lambda_l(\mathbf{x}_\alpha)$ of matrix $\tilde{\mathbf{K}}_t$ are obtained from the following system of linear equations which is written in terms of the auto-covariances and cross-covariances of the anamorphosed variables:

$$\sum_{l=1}^{n}\sum_{\alpha=1}^{N_h}\lambda_l(\chi_\alpha)C_{\tilde{H}}(s,\tau) = C_{\tilde{Y}\tilde{H}}(s,\tau) \tag{9}$$

Back-transformation step

After applying the modified update step, it is necessary to return to the original space for interpretative purposes. The mapping of the conditioned anamorphosed random variables into the original non-Gaussian distributed variables is made with:

$$\left(Y\left(\mathbf{x}_i\right)\middle|D\right) = F_{\tilde{Y}|\tilde{H}}^{-1}\left(\Phi\left(\tilde{Y}\left(\mathbf{x}_i\right)\middle|D\right)\right) \tag{10}$$

This means that the conditional CDF value of the original variable is identified with the conditional CDF value at its corresponding Gaussian transform value (Goovaerts, 1997) (Figure 1). The inverse of the univariate conditional CDF, i.e. $F_{\tilde{Y}|\tilde{H}}^{-1}(\cdot)$, is in fact a pseudoinverse function of its theoretical counterpart, but when the latter is strictly increasing, the pseudoinverse equals the usual inverse (Nelsen, 1997).

Computation of conditional moments

The conditional mean $\mu_{Y|H}(\mathbf{x})$ and conditional variance $\sigma^2_{Y|H}(\mathbf{x})$ of $Y(\mathbf{x})$, given that N_h observations of $H(\chi_1, t{=}1)$ are known, may be computed from:

$$\mu_{Y|H}(\mathbf{x}){=}E\{Y^c(\mathbf{x})\} \tag{11}$$

$$\sigma^2_{Y|H}(\mathbf{x}){=}E\{(Y^c(\mathbf{x}){-}E\{(Y^c(\mathbf{x})\})(Y^c(\mathbf{x}){-}E\{(Y^c(\mathbf{x})\})\} \tag{12}$$

where $Y(\mathbf{x})|D){=}Y^c(\mathbf{x})$.

Numerical implementation

The mathematical model described in the previous sections is coded in FORTRAN

programming language on the LINUX platform and run in the HPC cluster "Tonatiuh" at the Institute of Engineering, UNAM. A block diagram describing its numerical implementation is depicted in Figure 2. Note that the conditioning process is repeated at the next time at which observations are available, but the new prior log-conductivity random field becomes the posterior one at time t=1.

Application of the tEnKF to the identification of conductivities

Multivariate spatiotemporal random fields have been used in a variety of geophysical applications. For example, Bodas-Salcedo *et al*. (2003) combined spatiotemporal random fields with the Kalman filter method to predict solar radiation in the earth-atmosphere system; Suciu (2014) used a diffusion model to predict solutes transport in groundwater under uncertainty about spatiotemporal evolution of velocity fields; a similar approach was used by Suciu *et al*. (2016) to model reactive transport; Sanchez *et al*. (2016) developed a spatiotemporal dynamic model based on the classical EnKF for Bayesian inference of rainfall; and Liang *et al*. (2016) used a stochastic groundwater flow model to analyze the effect of uncertainty in recharge and transmissivity on the spatiotemporal variations of groundwater level in an unconfined aquifer. Finally, Moslehi and de Barros (2017) investigated the impact of uncertainty in spatial variability of soil hydraulic conductivity on several environmental performance metrics that are relevant for environmental risk assessments, such as species concentrations and arrival times, using a stochastic advection-dispersion model to represent the spatiotemporal evolution of the concentration field.

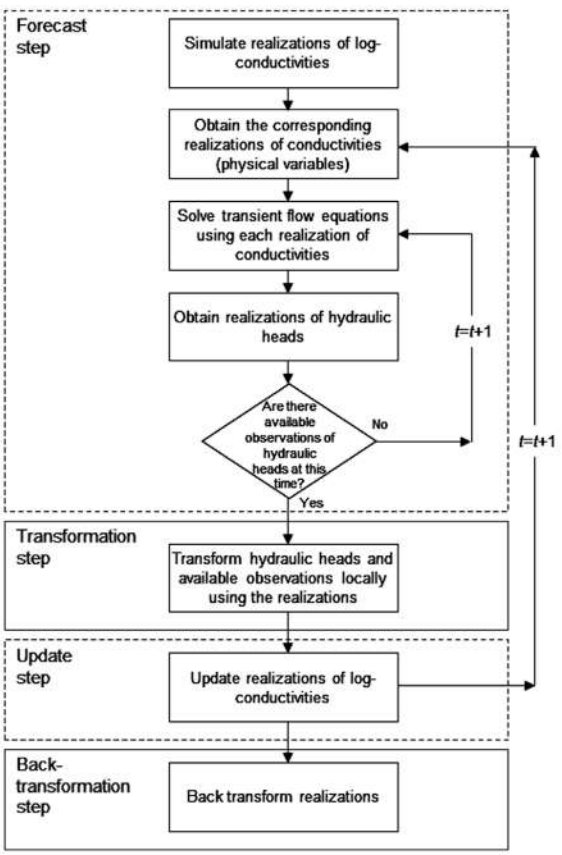

Figure 2. Block diagram of the EnKF with transformed data (tEnKF).

In this paper, the tEnKF is applied to infer the hydraulic conductivity field in a confined porous medium on the basis of the observed spatiotemporal variations of the hydraulic head field. For the sake of simplicity, groundwater flow through a one-dimensional, vertical, fully saturated random porous medium is considered (equations 1–2). It is assumed that hydraulic head at the lower boundary of the porous medium diminishes at a constant rate known from historical records and that this decrement is associated with groundwater withdrawal from wells located farther away. This simplified setting allows useful preliminary evaluations of the tEnKF. However, it is recognized that these two hypotheses can be avoided by 3D modeling of the system including the wells, and by considering that the spatial variability of the hydraulic conductivity in porous media is in fact 3D. The coupling of this dynamic model within the tEnKF is being developed and the results will be presented in further publications.

The porous medium is 40m deep and is discretized into 80 finite elements each with a length of 0.5m. Each finite element e_i for i=1,…,80 is assigned a log-conductivity value $y^{ref}(\mathbf{x}_i)$ according to the following procedure. First, a multi-Gaussian field $g(\mathbf{x})$ with exponential auto-covariance function and correlation scale a=2.5m is simulated using a modified version of the SGSIM random field generator (Deutsch and Journel, 1992) (Figure 3a). Second, the *V*-transform is applied in the following manner (Bárdossy and Li, 2008):

$$v(\mathbf{x}) = \begin{cases} k(g(\mathbf{x})m) \text{ if } g(\mathbf{x}) \geq m \\ k(g(\mathbf{x})m) \text{ if } g(\mathbf{x}) \geq m \end{cases} \quad (13)$$

with arbitrarily chosen parameters m=0 and k=1, to the previously generated $g(\mathbf{x})$ field to obtain the transformed $v(\mathbf{x})$ field (Figure 3b). Third, a Gaussian distribution is imposed to the $v(\mathbf{x})$ field as $y'=\Phi^{-1}[F_V(v)]$ where $F_V(v)$ is

the empirical CDF of the $v(\mathbf{x})$ field. Finally, this $y'(\mathbf{x})$ field is scaled to a normally distributed $y^{ref}(\mathbf{x})$ field with mean value m_Y=-1.654 and variance s^2_Y=0.997 as: $y^{ref}(\mathbf{x})=m_Y+y'(\mathbf{x})s_Y$. Each one of these values is assumed to be constant within its finite element e_j. This log-conductivity field, which is displayed in Figure 3c, is called the reference field and is considered the "true state of nature".

Several interesting properties of the *V*-transformation should be mentioned. First, the symmetric distribution function of the Gaussian field $g(\mathbf{x})$ is transformed into an asymmetrical distribution function through parameters m and k. Second, the empirical auto-covariance function of $g(\mathbf{x})$ is not preserved in $v(\mathbf{x})$ because the *V*-transformation is non-monotonous (Figure 4). Third, the spatial correlation of $v(\mathbf{x})$ is stronger for the values above the median than for the values below the median, i.e. the spatial correlation of $v(\mathbf{x})$ is asymmetric. This characteristic of the field holds after imposing the Gaussian (normal) distribution function onto it because the Gaussian transformation is monotonous (Deustch and Journel, 1992).

In the present example, since $y^{ref}(\mathbf{x})$ is normally distributed, $k_s(\mathbf{x})=\exp(y^{ref}(\mathbf{x}))$ is lognormally distributed with expected value μ_{Ks}=0.315 m/day and variation coefficient CV_{Ks}= 1.31. Conductivity fields with lognormal univariate distributions and asymmetric spatial correlation are considered to be more representative of natural porous media (Gómez-Hernández and Wen, 1998; Journel and Zhang, 2006). Specific storage coefficient is assumed to be equal to 0.001m^{-1} throughout the porous medium.

Using the reference field of conductivities, groundwater head responses are generated by solving a transient flow condition with finite elements (Smith and Griffiths, 2004). At t=0 days, the initial distribution of heads is hydrostatic. At t>0 days, hydraulic head decreases with time at a rate of 0.15 m/day during 150 days at the lower boundary. For the purpose of the present numerical example, the distribution of heads at t=90 days is assumed to be the initial condition (denoted as t=0 days in Figure 5 and henceforth). It is further assumed that groundwater head responses are available at times t=3, t=18 and t=60 days at the two locations indicated in Figure 5. Thus, two histories with three hydraulic head values are generated. These indirect, informative variables of the hydraulic conductivity of the reference field are considered available transient piezometric observations. At each one of these three times, the update step of the tEnKF scheme is performed.

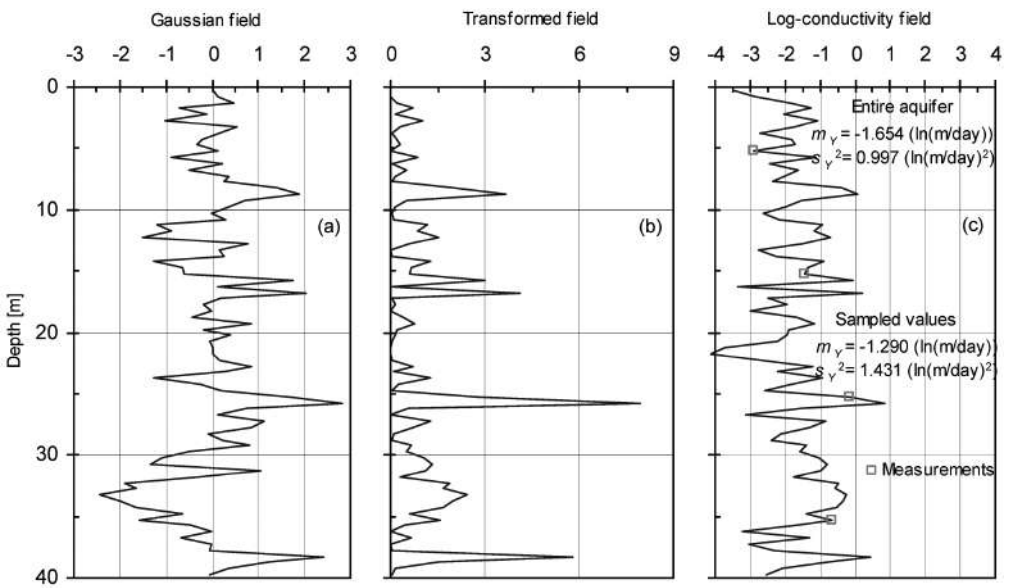

Figure 3. One dimensional fields: a) Initial Gaussian field, b) Field after applying the *V*-transform with parameters m=0 and k=1 to the initial Gaussian field, c) Final log-conductivity field after imposing a marginal normal distribution with expected value m_Y=-1.654 and variance s_Y^2=0.997 to the *V*-transformed field. Statistics of sampled values (empty squares) are also reported.

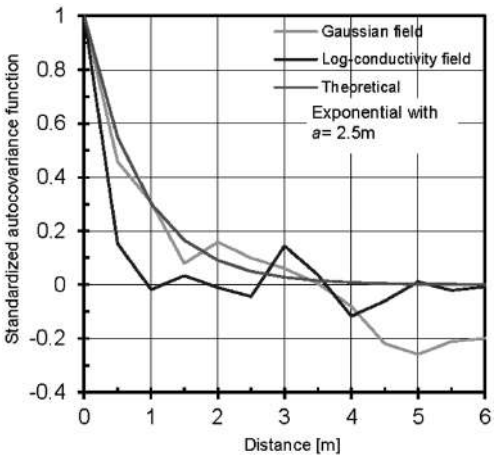

Figure 4. Standardized auto-covariance functions of the initial Gaussian field and reference log-conductivity field. An exponential function is also shown for comparison.

The reference field is sampled at four locations indicated in Figure 3c and the values are considered direct log-conductivity measurements. The mean and variance of the set of sampled values are reported in the same figure. Observe that these statistics overestimate the mean and variance of the reference field. Observe also in Figure 4 that an exponential auto-covariance function with correlation scale a=2.5m overestimates the correlation scale of the reference field as well. The sampled mean and variance, as well as the auto-covariance function mentioned above, are used to simulate two thousand unconditional multi-Gaussian log-conductivity realizations. Since the realizations are multi-Gaussian, they do not exhibit the asymmetric spatial correlation structure of the reference field (Journel and Deutsch, 1993). This set of log-conductivity fields attempts to model a situation in which the mean value, variance and auto-correlation function of the reference field are only roughly estimated *a priori* and the asymmetry of this field is ignored. It represents, in fact, the prior uncertainty about spatial variability of the conductivity in the porous medium.

The chosen number of simulated realizations ensures the stability of the following two error measures, according to preliminary computations:

$$RMSE = \sqrt{\frac{1}{n}\sum_{i=1}^{n}\left(y^*(\mathbf{x}_i) - y^{ref}(\mathbf{x}_i)\right)^2} \quad (14)$$

where n is the number of log-conductivities in the flow domain, $y^*(\mathbf{x}_i)$ is the estimated mean log-conductivity at location $\mathbf{x}_i$, and $y^{ref}(\mathbf{x}_i)$ is the reference log-conductivity also at location $\mathbf{x}_i$.

The SPREAD is computed as:

$$SPREAD = \sqrt{\frac{1}{n}\sum_{i=1}^{n} s_{en}^2(\mathbf{x}_i)} \quad (15)$$

where $s^2_{en}(\mathbf{x}_i)$ is the variance of the estimation of the log-conductivity at location $\mathbf{x}_i$ computed statistically over the ensemble of realizations.

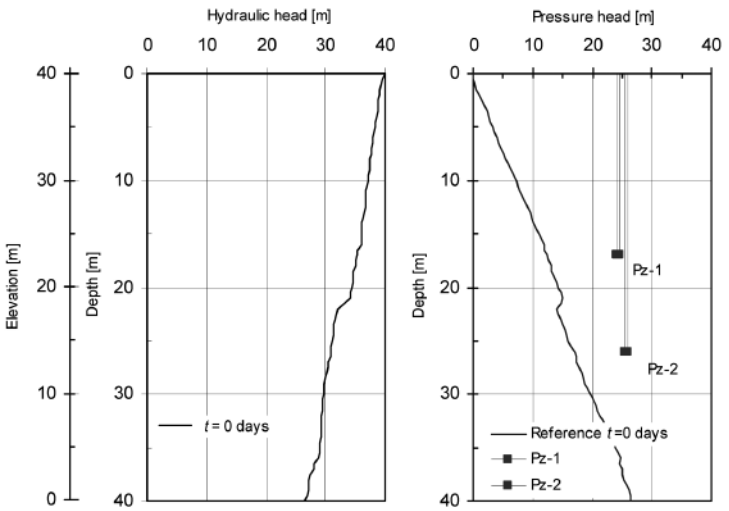

Figure 5. Profile of hydraulic heads in the reference field at t=0 days. The depths of the tips of two piezometers (Pz-1 and Pz-2) are indicated with filled squares.

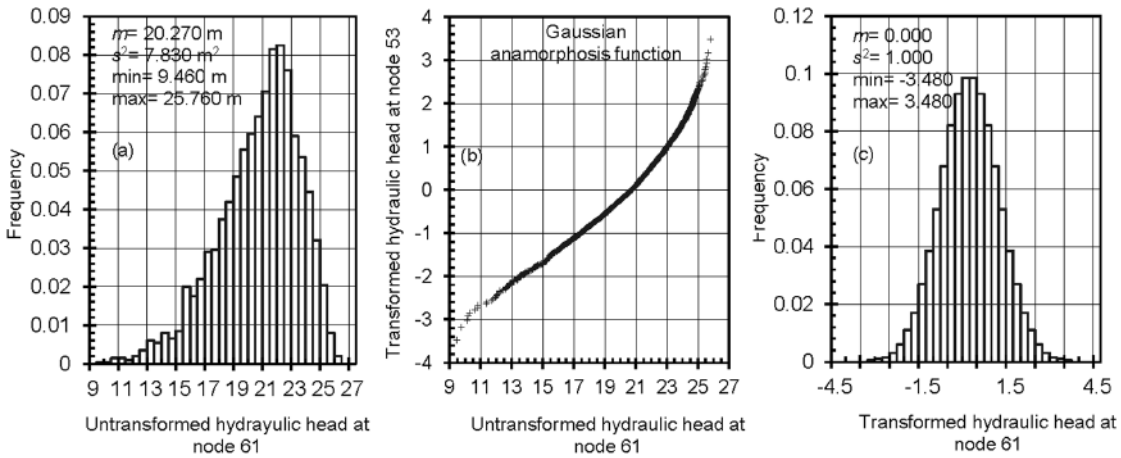

Figure 6. Gaussian transformation of hydraulic heads at node 61: a) Histogram of untransformed hydraulic heads, b) Gaussian anamorphosis function (with zero mean and unity variance), c) Histogram of hydraulic heads after the Gaussian anamorphosis.

It is worth mentioning that RMSE is a measure of the difference of the means of the estimated and reference fields and SPREAD is a measure of the dispersion of the estimated field around the reference field. Therefore, they can be viewed as measures of accuracy and precision of the estimations, respectively.

Results and discussion

Effect of the Gaussian transformation

Figure 6 illustrates the Gaussian transfor-mation process of the hydraulic head at an arbitrarily selected node before the first update step. In general, the shape of the local distributions depends on the location of the node in the flow domain and on the boundary conditions of the problem at hand. In all cases, the local distribution functions can be transformed into Gaussian distributions by building local Gaussian anamorphosis functions numerically, as explained earlier. As can be seen in Figure 6(a), although the original values exhibit a skewed distribution, the transformed variable becomes symmetric around the mean showing the well-known bell-shape of the Gaussian anamorphosis (Figures 6b and 6c).

Figure 7 represents the relationship between log-conductivities and heads at arbitrarily selected locations, before (Figure 7a) and after (Figure 7b) applying the respective Gaussian transformations. Given that the Gaussian transformation is monotonous, the bivariate characteristics of the dependence, such as the correlation structure at different percentiles, are not modified (Deutsch and Journel, 1992; Chilès and Delfiner, 1999). However, the linear correlation coefficient, which depends on the kind of marginal distributions of the random variables, might be different before and after transformations. In the particular case of the variables at the locations indicated in Figure

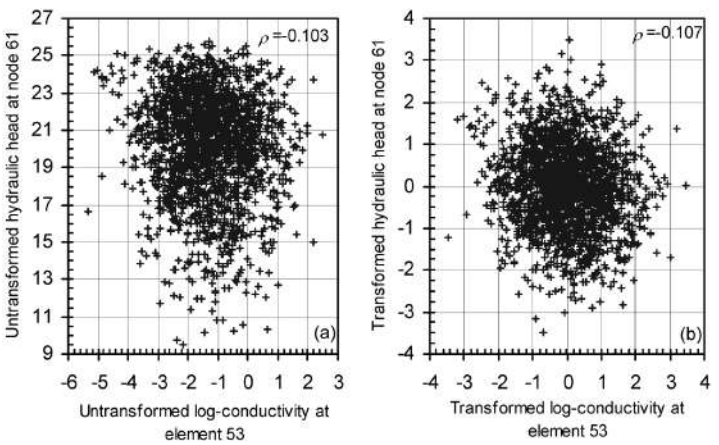

Figure 7. Relationship between log-conductivity and hydraulic head at two arbitrary selected locations (ρ is the Pearson correlation coefficient): a) Before the Gaussian transformation of both variables, b) After the Gaussian transformation of both variables.

7 (at the upper right corner of each figure), this coefficient presents nearly the same value before and after transformations. Therefore, the implicit pseudo-linearization effect associated to the Gaussian anamorphosis reported by Shöniger *et al*. (2012) should be considered application dependent.

Effects of conditioning on log-conductivities alone

The impact of conditioning realizations of log-conductivities to direct measurements only is analyzed. Figure 8 displays comparisons between the reference field of log-conductivities and the mean of the conditional realizations of log-conductivities. Contrasting both fields, it is observed that at the measurement locations the conditional value is the measured value.

Figure 9 reproduces profiles of standard deviations (uncertainty) computed with the conditional realizations of log-conductivities. Observe that the effect of conditioning is to reduce, overall, the prior uncertainty and to collapse it to zero at the locations of the measurements.

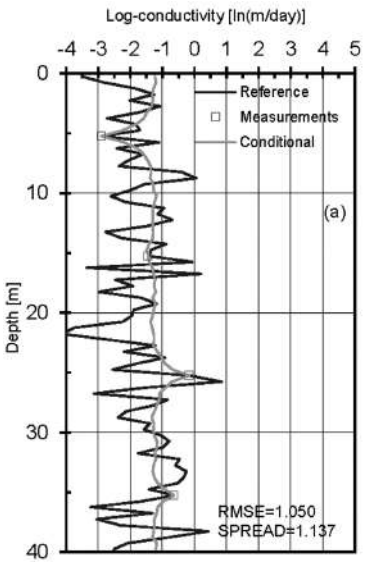

Figure 8. Log-conductivity fields conditional to log-conductivities alone. The reference field is also shown.

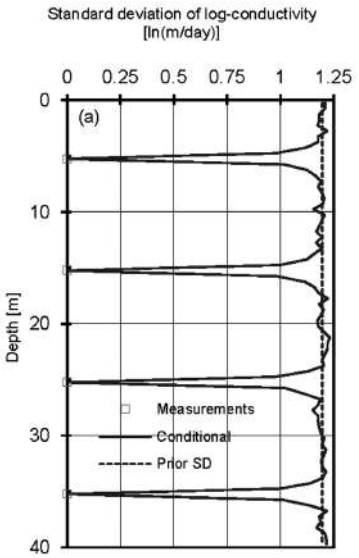

Figure 9. Profiles of conditional standard deviations of log-conductivities with respect to depth (empty squares indicate the locations of known values).

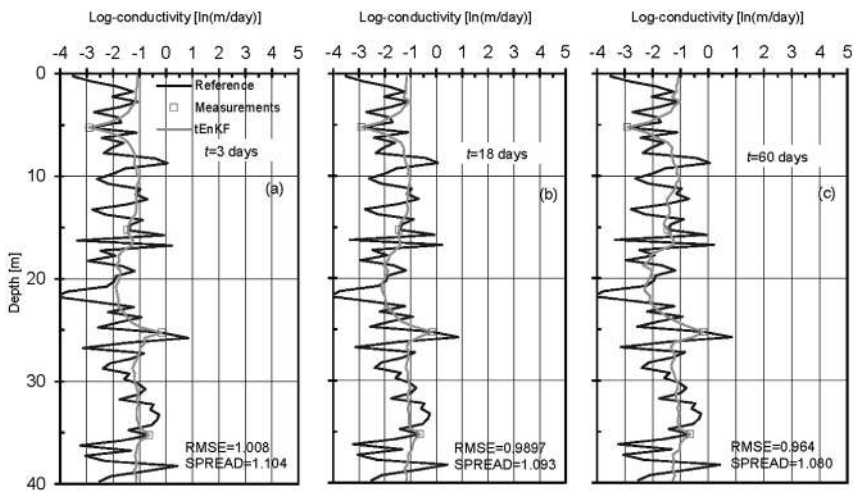

Figure 10. Log-conductivity fields conditional to histories of hydraulic heads with the tEnKF method. The reference field is also shown: a) At t=3 days, b) At t=18 days, c) At t=60 days.

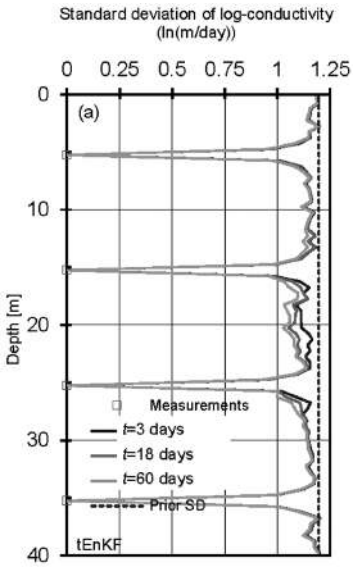

Figure 11. Profiles of conditional standard deviation of log-conductivities with respect to depth at different times (empty squares indicate the locations of known values).

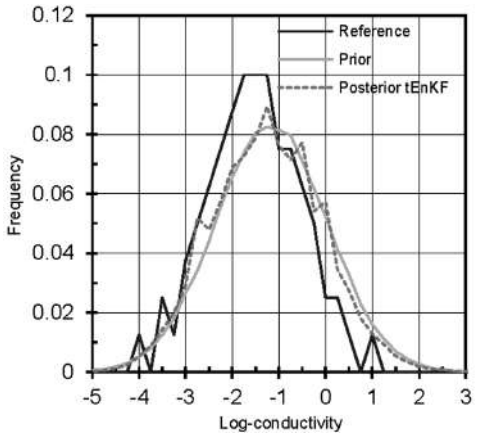

Figure 12. Frequency distributions of log-conductivities of the reference field, set of prior realizations and sets of posterior realizations at t=60 days.

Effects of conditioning on log-conductivities and transient heads

In what follows, the additional impact of conditioning the realizations of log-conductivities to transient heads responses is examined. Comparisons of the reference field of log-conductivities with the mean of the conditional realizations of log-conductivities of the tEnKF at times t=3, t=18 and t=60 days are shown in Figures 10a, b and c, respectively.

Contrasting the RMSE and SPREAD values shown at the bottom right corner of Figure 10a with the same two error measures shown in Figure 8, it can be observed that the estimation of the hydraulic head field becomes more accurate and precise after assimilating the first pair of measured hydraulic heads with the tEnKF. Further improvements in the estimation of the reference field are observed as more measured hydraulic head data are assimilated. For instance, the RMSE and SPREAD values for the conditional mean log-conductivity field of the tEnKF at time t=60 days are 0.964 and 1.080, whereas before the filtering process they were equal to 1.050 and 1.137, respectively. The accuracy of the estimation with the tEnKF can be attributed to the fluctuations that occur between measurements which follow the variability of the reference medium more closely. However, it should be recalled that the RMSE and SPREAD values measure the quality of the local estimation only, i.e. they do not indicate anything about the quality of the multivariate estimation. Bivariate empirical copulas can be used to perform this evaluation (Bárdossy and Li, 2008).

The standard deviation profiles calculated with the realizations of log-conductivities of the tEnKF are reported in Figure 11. The overall uncertainty decreases as longer groundwater head records are incorporated into the update step, except at the locations of direct measurements where uncertainty is zero at all times. The Figure shows that uncertainty is smaller around depths of 17 m and 26 m (where the tips of the two piezometers are located) than at other depths.

Figure 12 displays the frequency distributions of log-conductivities of the reference field and of the prior and posterior ensembles at the end of the conditioning process. Recall that the mean value of the conductivity of the reference field was overestimated by the prior random field; hence, the distribution function of this field is located to the right of the field's frequency function. Looking at the distributions of the posterior fields, it is observed that they exhibit some features of the reference frequencies (like some of the "peaks" of both branches) and that they are slightly displaced toward the left of the frequencies of the prior random field. This result illustrates the attempt of the filter to lead the prior frequencies toward the reference frequencies when a small

number of instruments and short records of measured hydraulic head responses (t=3, t=18 and t=60 days) are used in the conditioning process and when the initial representation of the asymmetric correlation structure of the true field is ignored by the prior random field model. Although there is a benefit, the degree of improvement of the initial approximation should be further investigated because the depth and distance between instruments, as well as the times at which observations are available, and the length of the histories of hydraulic head responses may also have an effect on the results.

Conclusions

This paper proposed that in order to evaluate the performance of tEnKFs in synthetically generated fields of the hydraulic conductivity, it is necessary to take into account the risk of introducing a systematic bias in the spatiotemporal evolution of the hydraulic head field by incorporating prior knowledge with a multi-Gaussian conductivity correlation structure, and by adopting a reference field with asymmetric correlation structure. This setting aims to offer a truer representation of common situations in practice in which the first two moments and the auto-covariance function of the real field are roughly known, but the asymmetry of the spatial correlation structure of that field is unknown.

As an example of the proposed approach, hydraulic conductivities were identified using the tEnKF by solving a one-dimensional, single phase flow problem in a continuous random porous medium. Three effects on the reproduction of the reference field were evaluated: the effect of the Gaussian transformation process, the effect of incorporating only measured hydraulic conductivities and the effect of incorporating measured hydraulic conductivities and hydraulic heads data. The results of this example indicate that when the asymmetry of the spatial correlation structure of the reference field was unknown *a priori*, the tEnKF was still capable of improving the initial approximation. However, no definitive conclusions can be drawn from this study in terms of the performance of tEnKF under this constraint since the degree of improvement of the initial approximation may further depend on the configuration of the array of instruments, the times at which observations are available and the length of time series of hydraulic heads.

Further research is needed to fully assess the performance of the EnKF with transformed data. For example, its effect on the reproduction of the multivariate spatial dependence of a non multi-Gaussian reference field using a multi-Gaussian random field model of conductivities in the prior approximation should be explored

Acknowledgments

The authors sincerely thank the four anonymous reviewers for improving the clarity of the original manuscript with their comments. We would also like to thank the people at the Academic Writing Office at the Coordinación de Estudios de Posgrado, UNAM, for their help revising our manuscript.

References

Bárdossy A., Li J., 2008, Geostatistical interpolation using copulas, *Water Resour. Res.*, 44, W07412, (1 of 15).

Bárdossy A., Hörning S., 2016, Gaussian and non-Gaussian inverse modeling of groundwater flow using copulas and random mixing, *Water Resour. Res.*, 52, pp. 4504–4526.

Béal D., Brasseur P., Brankart J., Ourmieres Y., Verron J., 2010, Characterization of mixing errors in a coupled physical biogeochemical model of the North Atlantic: implications for nonlinear estimation using Gaussian anamorphosis, *Ocean Sci.*, 6, pp. 247–62.

Bertino L., Evensen G., Wackernagel H., 2003, Sequential Data Assimilation Techniques in Oceanography, *Int. Statis. Rev.*, 71, 2, pp. 223–241.

Billingsley P., 1995, Probability and measure, 3rd ed. Wiley, New York.

Bodas-Salcedo A., López-Baeza E., Martinez F., Mateu J., Montes F., 2003, Spatiotemporal modeling and prediction of solar radiation, *J. of Geophys. Res.*, 108, D24, 8777.

Burgers G., van Leeuwen P.J., Evensen G., 1998, Analysis scheme in the Ensemble Kalman Filter, *Mon. Weather Rev.*, 126, 6, pp. 1719-1724.

Capilla J., Llopis-Albert C., 2009, Gradual conditioning of non-Gaussian transmissivity fields to flow and mass transport data: 1, Theory, *J. Hydrol.*, 371, pp. 66–74.

Chilès C., Delfiner P., 1999, Geostatistics: modeling spatial uncertainty, Wiley, New York.

Dagan G., 1989, Flow and transport in porous formations, Springer-Verlag, Berlin, Germany.

Deutsch C.V., Journel A.G., 1992, GSLIB, Geostatistical Library and User's Guide, Oxford University Press, Oxford, N. Y., USA.

Elsheikh A.H., Wheeler M.F., Hoteit I., 2013, An iterative stochastic ensemble method for parameter estimation of subsurface flow models, *J. of Comput. Phys.*, 242, pp. 696–714.

Emerick A.A., 2017, Investigation on Principal Component Analysis Parameterizations for History Matching Channelized Facies Models with Ensemble-Based Data Assimilation, *Mathematical Geosciences*, 49, pp. 85–120.

Erdal D., Rahman M.A., Neuweiler I., 2015, The importance of state transformations when using the ensemble Kalman filter for unsaturated flow modeling: Dealing with strong nonlinearities, *Adv. Water Resour.*, 86, pp. 354–365.

Evensen, G., (1992). Using the extended Kalman filter with a multilayer quasi-geostrophic ocean model, *J. Geophys. Res.*, 97, 11, pp. 17905–17924.

Evensen G., 1994, Sequential data assimilation with a nonlinear quasi-geostrophic model using Monte Carlo methods to forecast error statistics, *J. Geophys. Res.*, 99, pp. 10143–10162.

Evensen G., 2003, Data assimilation: the ensemble Kalman Filter, Springer, New York.

Gelhar L.W., 1993, Stochastic subsurface hydrology, Pentrice Hall, New Jersey.

Goovaerts P., 1997, Geostatistics for natural resources evaluation, Oxford University Press, New York.

Gómez-Hernández J.J., Wen X., 1994, Probabilistic assessment of travel times in groundwater modeling, *Stoch. Hydrol Hydraul.*, 8, 1, pp. 19–55.

Gómez-Hernández J., Wen X., 1998, To be or not to be multi-Gaussian? A reflection on stochastic hydrogeology, *Adv. Water Resour.*, 21, 1, pp. 47-61.

Gómez-Hernández J.J., Sahuquillo A., Capilla J.E., 1997, Stochastic Simulation of Transmissivity Fields Conditional to Both Transmissivity and Piezometric Data, 1, Theory, *J. Hydrol.*, 203, pp. 162–174.

Haslauer C., Guthke P., Bárdossy A., Sudicky E., 2012, Effects of non-Gaussian copula-based hydraulic conductivity fields on macrodispersion, *Water Resour. Res.*, 48, W07507.

Hendricks F.H.J., Kinzelbach W., 2008, Real-time groundwater flow modeling with the Ensemble Kalman Filter: Joint estimation of states and parameters and the filter inbreeding problem, *Water Resour. Res.*, 44, W09408

Hu L.Y., 2000, Gradual deformation and iterative calibration of Gaussian-related stochastic models, *Math. Geol.*, 32, 1, pp. 87–108.

Hu L.Y., Zhao Y., Liu Y., Scheepens C., Bouchard A., 2013, Updating multipoint simulations using the ensemble Kalman filter, *Compu. Geosci.*, 51, pp. 7–15.

Johns C.J., Mandel J., 2008, A two-stage ensemble Kalman filter for smooth data assimilation, *Environ. Ecol. Stat.*, 15, pp. 101–110.

Journel A., Alabert F., 1989, Non-Gaussian data expansion in the earth sciences, Terra Nova, 1, pp. 123-134.

Journel A.G., Deutsch C.V., 1993, Entropy and spatial disorder, *Math. Geol.*, 25, 3, pp. 329–55.

Journel A.G., Huijbregts C., 1978, "Mining geostatistics", Academic Press, San Diego, Calif.

Journel A., Zhang T., 2006, The necessity of a multiple point statistical model, *Math. Geol.*, 38, 5, pp. 591-610.

Kalman R.E., 1960, A new approach to linear filtering and prediction problems, *J. Basic Eng.*, 82, pp. 35–45.

Katzfuss M., Stroud J.R., Wikle C.K., 2016, Understanding the Ensemble Kalman Filter, *Am. Stat.*, 70, 4, pp. 350-357.

Kerrou J., Renard P., Hendricks Franssen H.J., Lunati I., 2008, Issues in characterizing heterogeneity and connectivity in non-multiGaussian media, *Adv. Water Resour.*, 31, pp. 147–159.

Knudby C., Carrera J., 2005, On the relationship between indicators of geostatistical flow and transport connectivity, *Adv. Water Resour.*, 28, pp. 405–421.

Leng C.H., Yeh H.D., 2003, Aquifer parameter identification using the extended Kalman filter, *Water Resour. Res.*, 39, 3, 1062.

Li L., Zhou H., Hendricks F.H.J., Gómez-Hernández J.J., 2012, Groundwater flow inverse modeling in non-MultiGaussian media: performance assessment of the normal-score Ensemble Kalman Filter, *Hydrol. Earth Sys. Sci.*, 16, pp. 573–590.

Li L., Srinivasan S., Zhou H., Gómez-Hernández J.J., 2013, A pilot point guided pattern matching approach to integrate dynamic data into geological modeling, *Adv. Water Resour.*, 62, pp 125–38.

Li L., Srinivasan S., Zhou H., Gómez-Hernández J.J., 2014, Simultaneous estimation of geologic and reservoir state variables within an ensemble-based multiple-point statistic framework, *Math. Geosci.*, 46, 5, pp. 597–623.

Li L., Srinivasan S., Zhou H., Gómez-Hernández J.J., 2015, Two-point or multiple point statistics? A comparison between the ensemble Kalman filtering and the ensemble pattern matching inverse methods, *Adv. Water Resour.*, 86, pp. 297–310.

Liang X., Zhang Y.K., Schilling K., 2016, Effect of heterogeneity on spatiotemporal variations of groundwater level in a bounded unconfined aquifer, *Stoch. Environ. Res. Risk Assess.*, 30, pp. 1–8.

Miller R.N., Carter E.F., Blue S.T., 1999, Data assimilation into nonlinear stochastic models, *Tellus* A, 51, pp. 167–194.

Moslehi M., de Barros F., 2017, Uncertainty quantification of environmental performance metrics in heterogeneous aquifers with long-range correlations, *J. Contam. Hydrol.*, 196, pp. 21–29.

Nelsen R.B., 1997, An introduction to copulas, Springer, Berlin.

Oliver D., Cunha L., Reynolds A., 1997, Markov chain Monte Carlo methods for conditioning a permeability field to pressure data, *Math. Geol.*, 29, 61–91.

RamaRao B., LaVenue A., De Marsily G., Marietta M., 1995, Pilot point methodology for automated calibration of an ensemble of conditionally simulated transmissivity fields, 1, theory and computational experiments, *Water Resour. Res.*, 31, 3, pp. 475–93.

Reichle R.H., Walker J.P., Koster R.D., Houser P.R., 2002, Extended versus ensemble Kalman filtering for land data assimilation, *J. Hydrometeorol.*, 3, pp. 728–740.

Rosenblatt M., 1952, Remarks on a multivariate transformation, The Annals of Mathematical Statistics, 23, 3, pp. 470-472.

Sahuquillo A., Capilla J.E., Gómez-Hernández J.J., Andreu J., 1992, Conditional simulation of transmissivity fields honoring piezometric head data, In: Hydraulic Engineering Software IV, Fluid Flow Modeling, edited by: Blair, W. R. and Cabrera, E., Vol. II, Elsevier Applied Science, London, UK, pp. 201–214.

Sanchez L., Infante S., Griffina V., Reya D., 2016, Spatio-temporal dynamic model and parallelized ensemble Kalman filter for precipitation data, *Braz. J. Probab. Stat.*, 30, 4, pp. 653–675.

Sarma P., Chen W.H., 2009, Generalization of the Ensemble Kalman Filter using kernels for non-Gaussian random fields, SPE 119177, pp. 1-20.

Schöniger A., Nowak W., Hendricks F.H., 2012, Parameter estimation by ensemble Kalman filters with transformed data: Approach and application to hydraulic tomography, *Water Resour. Res.*, 48, W04502, pp. 1-18.

Shinozuka M., Zhang R., 1996, Equivalence between Kriging and CPDF Methods for Conditional Simulation, *J. Eng. Mech.*, 122, 6, pp. 530-538.

Simon E., Bertino L., 2009, Application of the Gaussian anamorphosis to assimilation in a 3D coupled physical ecosystem model of the North Atlantic with the EnKF: a twin experiment, *Ocean Sciences*, 5, pp. 495–510.

Simon E., Bertino L., 2012, Gaussian anamorphosis extension of the DEnKF for combined state parameter estimation: application to a 1D ocean ecosystem model, *J. Marine Syst.*, 89, 1, pp.1–18.

Smith I., Griffiths D., 2004, Programming the finite element method, John Wiley and Sons Ltd., England.

Suciu N., 2014, Diffusion in random velocity fields with applications to contaminant transport in groundwater, *Adv. Water Resour.*, 69, pp. 114–133.

Suciu N., Schüler L., Attinger S., Knabner P., 2016, Towards a filtered density function approach for reactive transport in groundwater, *Adv. Water Resour.*, 90, pp. 83–98.

Sun A.Y., Morris A.P., Mohanty S., 2009, Sequential updating of multimodal hydrogeologic parameter fields using localization and clustering techniques, *Water Resour. Res.*, 45, W07424.

Tarantola A., 2005, Inverse problem theory and methods for model parameter estimation. SIAM, USA.

Xu T., Gómez-Hernández J., Zhou H., Li L., 2013, The power of transient piezometric head data in inverse modeling: An application of the localized normal-score EnKF with covariance inflation in a heterogeneous bimodal hydraulic conductivity field, *Adv. Water Resour.*, 54, pp. 100–118.

Zhang D., 2002, Stochastic methods for flow in porous media, Academic Press, USA.

Zhou H., Gómez-Hernández J., Hendricks Franssen H., Li L., 2011, An approach to handling nongaussianity of parameters and state variables in ensemble Kalman filtering, *Adv. Water Resour.*, 34, 7, pp. 844–864.

Zhou H., Gómez-Hernández J.J., Li L., 2012, A pattern-search-based inverse method, *Water Resour. Res.*, 48, W03505.

Zhou H., Gómez-Hernández J.J., Li L., 2014, Inverse methods in hydrogeology: Evolution and recent trends, *Adv. Water Resour.*, 63, pp. 22–37.

Zovi F., Camporese M., Hendricks Franssen H.J., Huisman J.A., Salandin P., 2017, Identification of high-permeability subsurface structures with multiple point geostatistics and normal score ensemble Kalman filter, *J. Hydrol.*, 548, pp. 208–224.

Geofísica Internacional (2017) 56-4: 335-343

Original paper

The effect of salinity and gas saturation of a geothermal fluid on the reservoir permeability reduction

Juán Flores, Onésimo Meza, Sara L. Moya and Alfonso Aragón*

Received: March 08, 2016; accepted: August 22, 2017; published on line: October 01, 2017

Resumen

Los yacimientos geotérmicos altamente salinos muestran precipitación de sales en las formaciones rocosas que influyen en la reducción de su permeabilidad y por lo mismo en la productividad de los pozos. En este trabajo se muestran curvas teóricas de productividad másica de pozos geotérmicos (curvas de influjo), las cuales fueron obtenidas considerando mezclas ternarias de H_2O-CO_2-NaCl con hasta 25% de salinidad en peso y bajo diferentes condiciones iniciales de saturación de gas en el fluido. Se llevó a cabo el análisis de sensibilidad para la concentración inicial de sales y saturación inicial de gas usando el simulador TOUGH2. A partir del procesamiento de los resultados se obtuvieron curvas tipo que corresponden a yacimientos con características críticas, como baja permeabilidad, alta precipitación de sales y alta saturación de gas. Las curvas obtenidas muestran tres zonas muy bien definidas como función de la etapa de explotación del pozo: zona sin precipitación de sal; zona de transición; y zona con precipitación de sal. Se encontró que la zona con precipitación de sal en el yacimiento ocurre con mayor frecuencia a altas concentraciones iniciales de sales disueltas y alta saturación de gas. En algunas ocasiones se llegan a obstruir los poros de la formación rocosa, lo que influye en una reducción drástica de su permeabilidad. Se propone en este trabajo que las curvas tipo se pueden usar como una herramienta complementaria para el análisis de los pozos y para el diseño de las estrategias apropiadas para la explotación de campos geotérmicos.

Key words: Yacimientos geotérmicos salinos, curvas-tipo de influjo, precipitación de sales, reducción de permeabilidad, saturación de gas.

Abstract

Highly saline geothermal reservoirs show problems of salt precipitation on the rock formation reducing its permeability and the well's productivity. In this study, theoretical curves of mass productivity of geothermal wells (inflow type curves) were obtained considering ternary mixtures of H_2O-CO_2-NaCl of up to 25% salinity in weight and under different initial conditions of gas saturation of the fluid. The sensitivity analysis to the initial concentration of salts and initial gas saturation was carried out using the simulator TOUGH2. The developed type curves are focused to reservoirs with criti-cal characteristics such as, low permeability, ranges of high salt precipitation and high gas saturation. The obtained curves show three clearly defined zones as a function of the degree of exploitation of the well: no salt precipitation zones; transition zones; and salt precipitation zones. It was found that salt precipitation in the reservoir occurs in greater intensity at higher initial concentrations of dissolved salts and higher gas saturation. In some cases, scale obstructs the pores of the rock formation drastically reducing its permeability. It is proposed that type curves could be used as complementary tools for the analysis of wells and for the selection of pertinent strategies for the exploitation of geothermal fields.

Palabras clave: Saline geothermal reservoirs, inflow type-curves, salts precipitation, permeability reduction, gas saturation.

J. Flores
S. L. Moya
Centro Nacional de Investigación
y Desarrollo Tecnológico
Tecnológico Nacional de México
Interior Internado Palmira s/n
Col. Palmira, 62490
Cuernavaca, Morelos, México

O. Meza
Universidad Autónoma del Carmen
Calle 56 #4, Col. Benito Juárez
Cd. del Carmen 24180
Campeche, México

A. Aragón*
Instituto Nacional de Electricidad y Energías Limpias,
Reforma 113 Col. Palmira, 62490
Cuernavaca Morelos, México
Corresponding author: aaragon@iie.org.mx

Introduction

The chemical composition of geothermal fluids depends on the type of rocks in which they are stored. The two-phase flow appears due to the pressure drop which occurs when the reservoir fluid ascends through the production pipe, from the bottom to well head. Depending on several factor as: concentrations of salts, solubility of minerals, saturation states of characteristic minerals, temperature and pH of the system, super-saturated solutions can be produced from which solid phases precipitate as scaling. The most abundant gases found in geothermal reservoirs are carbon dioxide (CO_2), hydrogen sulfide (H_2S), nitrogen (N_2), hydrogen (H_2), and methane (CH_4). The salts present in the liquid phase are sodium chloride (NaCl), potassium chloride (KCl), calcium carbonate ($CaCO_3$), calcium chloride ($CaCl_2$) and silica (SiO_2).

The most representative ternary mixture of a geothermal fluid is H_2O-NaCl-CO_2 (Battistelli *et al*., 1997). CO_2 represents the effect of the non-condensable gases (Battistelli *et al*., 1993; Iglesias and Moya, 1998; Pruess and Garcia, 202; Lu *et al*., 2006) whereas the term used in THOUGH2 as NaCl represents that of total salts of reservoir fluid (Pritchett, 1993; Battistelli *et al*., 1997). The concentration of salts in the geothermal reservoirs is variable. Cases have been reported with salinities of relatively low percentages, between 0 and 3% by weight, up to high percentages of 28% by weight. The former, is the case of most Mexican geothermal fields (Bernard-Romero and Taran, 2010); whereas the latter encompasses the cases of the hypersaline geothermal reservoirs of Salton Sea (Sanyal *et al*., 2011) and of Tuzla in Turkey (Demir *et al*., 2014; Baba *et al*., 2015). The salts precipitation occur because of complex reactions that take place either at the reservoir or in the well because of pressure drops during production, in such cases clogging of pipes and generation equipment can occur. However, the most severe effect is the significant decrease in the well's productivity caused by scaling formed in the porous matrix of the rock formation, affecting its permeability. Understanding the behavior of the parameters productivity and permeability, may allow to take the pertinent precautionary actions to maintain a good well exploitation (Newton and Manning, 2002).

One of the most utilized tools to characterize the behavior of the productivity of a well is the analysis of its pressure and its mass flow, whose correlation leads to the creation of production curves of the well. Using the parameters measured at wellhead conditions, characteristics or output curves can be obtained. Whereas by using measurements at bottom hole conditions, inflow curves are obtained (IPR, Inflow Performance Relationships). The behavior of these curves reflects the thermophysical conditions of the reservoir at the region surrounding the well, at its feeding stratum. In order to obtain a complete characteristic curve in field, it is required for the well to be disconnected from the generation power plant. This can be time consuming and lead to economic losses. However, alternative methodologies relying on numerical simulations allow the generation of theoretical IPR curves, denominated inflow type-curves. Inflow type-curves were initially developed for oil reservoirs (Gilbert, 1954; Vogel, 1968) considering reservoir models of radial flow and an ample interval of fluid properties. Klins and Majcher (1992) developed and proposed a dimensionless IPR with damage effect using field information of 1400 oil wells.

Iglesias and Moya (1990) developed the first inflow type-curve for geothermal reservoirs (theoretical GIPR, Geothermal Inflow Performance Relationships) considering the existence of pure water at the reservoir. In a later study, Moya (1994) incorporated the effect of non-condensable gases developing a solubility model for the binary mixture H_2O-CO_2 (Moya and Iglesias, 1992; Iglesias and Moya, 1992). The applicability of these type-curves for the estimation of the productivity of geothermal wells was discussed by Moya *et al*. (1998) and Iglesias and Moya (1998). This methodology to estimate the productivity of geothermal wells was automated (Moya and Uribe, 2000) and later complemented with the estimation of the permeability of the rock formation adjacent to the well (Moya *et al*., 2001; 2003). Montoya (2003) developed inflow type curves for the ternary mixture H_2O-CO_2-NaCl with salinity of 0.5% by weight, applying the solubility model of Batistelli *et al*., (1997). Meza (2005) generated inflow type-curves for the same ternary mixture considering a high salt content by using the geothermal simulator TOUGH2 (Pruess *et al*., 1999), which includes the model of Batistelli *et al*., (1997). The initial temperature and gas saturation conditions were of 300°C and 0.005, respectively. The initial absolute permeability was 10 mD and a relative permeability of Corey type was considered. Flores (2007) complemented the work of Meza (2005) by incorporating the initial gas saturation effect in an interval of 0.05 to 0.45. Furthermore, inflow type curves with damage effect were developed by Aragón (2006) and applied in the determination of damage in geothermal wells (Aragón *et al*., 2008; Aragón *et al*., 2013).

This study shows geothermal inflow type-curves obtained through the numerical simulator TOUGH2 considering the ternary mixture H_2O-CO_2-NaCl with a high content of salts and under different initial gas saturation conditions of the fluid. The effects that the salts precipitation and gas saturation have on the changes of permeability in the geothermal reservoir are quantified and discussed. The practical uses of the obtained inflow curves, could be applied to geothermal fields furthermore are discussed. The developed type curves are focused to reservoirs with critical characteristics such as, low permeability, high degree of salts precipitation and high gas saturation.

Methodology

Physical Model

The physical model in this study consists of a cylindrical reservoir with 1000 m radius and 100 m depth. In its center a vertical well is situated, which produces at a constant mass flow rate (Figure 1). The flow in the porous medium is in radial direction following Darcy's law and consists of the ternary mixture H2O-CO2-NaCl. The reservoir is considered as a homogenous porous medium that is impermeable and adiabatic from above and below. The thermophysical properties of the reservoir are shown in Table 1.

Mathematical Model

Conservation Equations

The mass and energy balance equations for a system of NK mass components distributed in NPH phases, are written in the following general form (Pruess *et al*., 1999; Pruess, 1988):

Table 1. Thermophysical properties of the rock formation.

Porosity (∅)	0.10
Density (ρ)	2700 kg/m^3
Thermal conductivity (k)	2.0 W/(m ºC)
Specific heat (C)	1000 J/(kg ºC)

$$\frac{d}{dt}\int_{V_n} M^\kappa dV = \int_{\Gamma_n} F^\kappa \cdot n d\Gamma + \int_{V_n} q^\kappa dV \quad (1)$$

The integration is over an arbitrary subdomain V_n of the flow system under study, bounded by a closed surface Γ_n. In the accumulation term, M denotes mass or energy by unit of volume. $1 < \kappa <$ NK, comprises the mass components such as water, salinity and CO_2; whereas for κ = NK+1 the heat component is included. $\mathbf{F}$ represents the heat or mass fluxes. The individual phase fluxes are given through the multiphase version of Darcy's law. The sources and sinks are represented by $\mathbf{q}$. The heat flux contains conductive and convective components.

TOUGH2V2.0 allows to manage different fluid mixtures by defining the properties of each mixture separately through the modules of equations of state. The EWASG module includes the model of Battistelli *et al*. (1997) for the ternary mixture H_2O-NaCl-CO_2. In this model gas dissolution in the aqueous phase is described by Henry´s law and includes the Cramer correction (1982) to consider the effect of a decreased CO_2 solubility in the liquid phase due to the presence of salts ("salting out"). The thermophysical property correlations used in EWASG are accurate for most conditions of interest in geothermal reservoir studies (Pruess *et al*., 1999) at temperatures in the range from 100 to 350 °C, fluid pressures up to 80 MPa, CO_2 partial pressures up to 10 MPa, and salt mass fraction up to halite saturation. In the EWASG module NK = 3, NPH = 3; and κ = 1, 2, 3, 4 indicate water, salinity, noncondensible gases, and heat components respectively. The accumulation and mass flux terms for the salinity (κ = 2) are written as follows:

$$M^{(2)} = \varnothing S_S \rho_S + \varnothing S_L \rho_L X_L^{(2)} \quad (2)$$

$$F^{(2)} = -K \frac{Kr_L}{\mu_L} \rho_L X_L^{(2)} (\nabla P_L - \rho_L g) \quad (3)$$

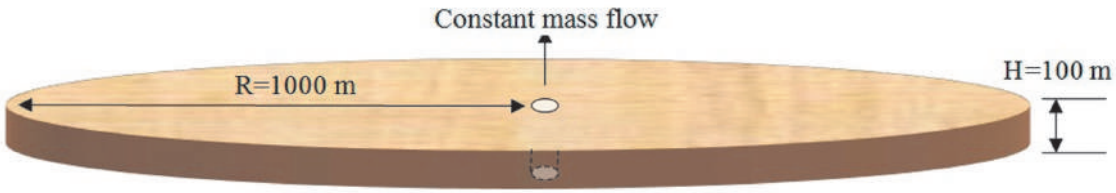

Figure 1. Schematic representation of the reservoir-well model.

where S is saturation, being S_S the solid saturation defined as the fraction of pore volume occupied by solid salt. X is the mass fraction, K the intrinsic permeability, K_r the relative permeability, μ the dynamic viscosity, P the pressure, and $\boldsymbol{g}$ the acceleration of gravity

Permeability Reduction

The EWASG module includes the Verma and Pruess (1988) model which consists of idealized geometries to correlate the permeability changes as a function of the modified porosity by the distribution of the precipitated minerals. The tubes in series geometry (alternating segments of capillary tubes with larger and smaller radii) is able to represent the presence of "bottle-necks" (Battistelli *et al*., 1997) in the flow channels and the permeability can be reduced to zero at a finite porosity (critical porosity). From this geometry the following relationship can be derived (Verma and Pruess, 1988):

$$\frac{K}{K_0} = \theta^2 \frac{1-\tau+\tau/\omega^2}{\left[1-\tau+\tau\ \theta/(+\omega-1)\right]^2} \qquad (4)$$

being

$$\theta = \frac{1-S_S-\varnothing_C}{1-\varnothing_C} \qquad (5)$$

where the parameter $\emptyset_C$ denotes the fraction of original porosity at which permeability is reduced to zero and is the fractional length of the pore bodies. The parameter ω is given by

$$\omega = 1 + \frac{1/\tau}{1/\varnothing_C - 1} \qquad (6)$$

The value of $\emptyset_C = \tau = 0.8$ is the most commonly used in simulations (Pruess and García, 2002; Pruess *et al*., 1999; Battistelli *et al*., 1995, 1997) which was estimated to reduce the permeability by 82% of its original value assuming a salt precipitation of only 2%. This study uses tubes in series model with a value of $\emptyset_C = \tau = 0.8$. A more thorough explanation of the mathematical model can be found in Battistelli *et al*. (1997) and Pruess *et al*. (1999).

Numerical Method

TOUGH2 uses the method of integral finite differences (Pruess, 1988; Narasimhan and Wintherspoon, 1976) for the spatial discretization of the conservation equations, Newton-Raphson for linearization, and a robust solver for matrix inversion.

The characteristics of the evaluated cases in this study are shown in Table 2. All cases were simulated using a 28 node radial grid. The node positions are given by $r_n = 0.1(2)^{(n-1)/2}$. Simulations for the different cases were carried out at different constant flowrates. For each run, the pressure of the inflow at the feedpoint of the well was recorded for different percentages of cumulative mass produced. In this way, geothermal inflow type-curves (theoretical GIPR) for fixed cumulative mass produced (e.g., 5, 10, …, 80%) were inferred.

Table 2. Study cases

Initial temperature (°C)	Initial pressure (bar)	K_0 (mD)	K_r	Initial % % CO_2 (by weight)	Initial % salinity (by weight)	Initial gas saturation	% cumulative mass produced
300	91.28	10	Corey	0.5	5	0.05, 0.15, 0.30, 0.45	5, 10, 15, 20, 25, 35, 40, 45, 50, 55, 60, 65, 70, 75, 80
300	84.60	10	Corey	0.5	15	0.05, 0.15, 0.30, 0.45	5, 10, 15, 20, 25, 35, 40, 45, 50, 55, 60, 65, 70, 75,80
300	76.81	10	Corey	0.5	25	0.05, 0.15, 0.30, 0.45	5, 10, 15, 20, 25, 35, 40, 45, 50, 55, 60, 65, 70, 75,80

Results

The obtained inflow type-curves of mass productivity are shown in Figures 2, 3, and 4 and cover all cases shown in Table 2. Overall, major pressure drops are observed as the cumulative mass produced percentage increases. The group of curves in black, denotes zones of conditions without salt precipitation and encompasses the lowest percentages of cumulative mass produced. As the exploitation of the well continues, the gas saturation and the salts concentration increase creating transition zones denoted in blue. In these transition zones the liquid and gaseous phases compete to flow, in agreement with the functionality of relative permeability of Corey type. Zones of salt precipitation are denoted in red and correspond to the highest percentages of cumulative mass produced with high gas saturation. The salt precipitation and transition zones make the geothermal fluid extraction difficult.

Discussion

For the case of the lowest concentration of dissolved salts (5% by weight; Figure 2), it can be observed that, as the initial gas saturation increases, the zones without salt precipitation decrease (curves in black) and disappear for an initial gas saturation of 45%. Inversely, the transition and salt precipitation zones increase, starting at earlier stages of the well exploitation (low percentages of cumulative mass produced). In this way, for the case of

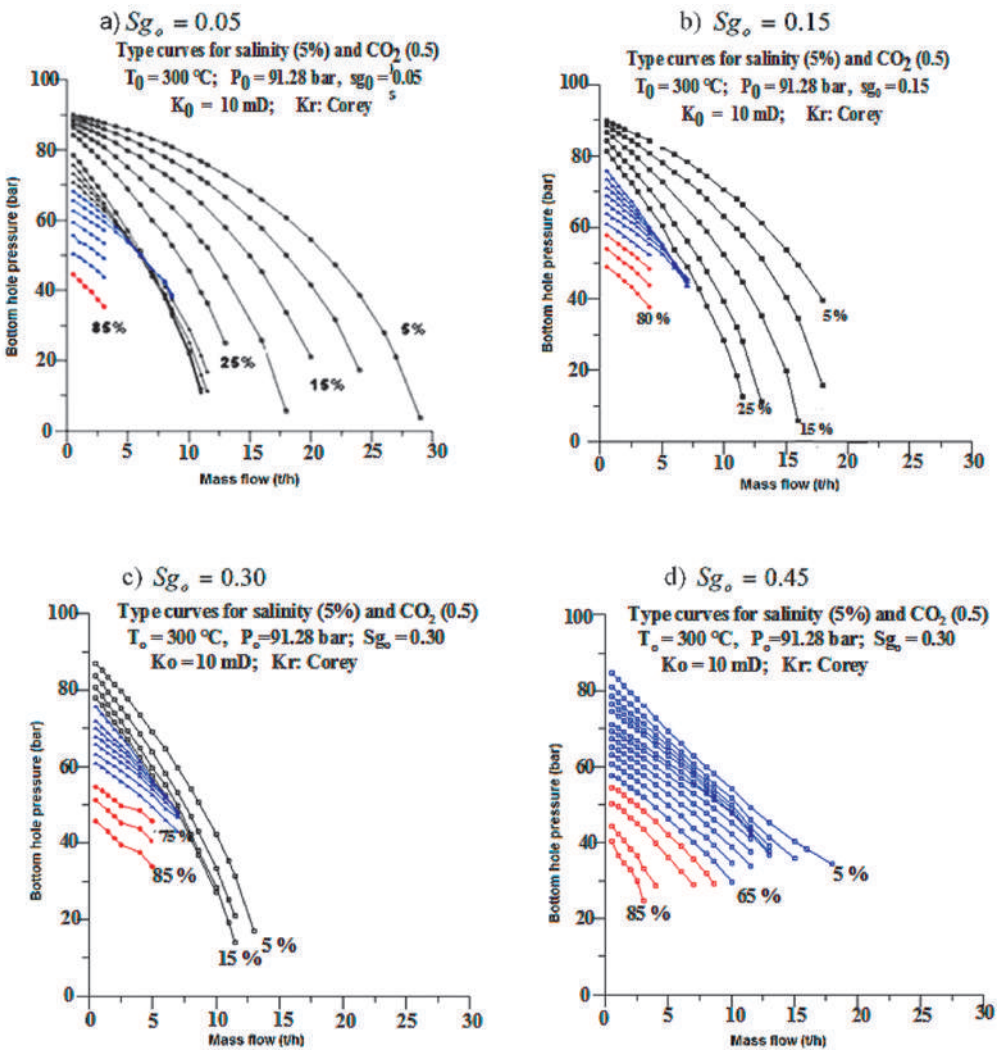

Figure 2. Type-curves of mass productivity as a function of the initial gas saturation and 5% salinity by weight.

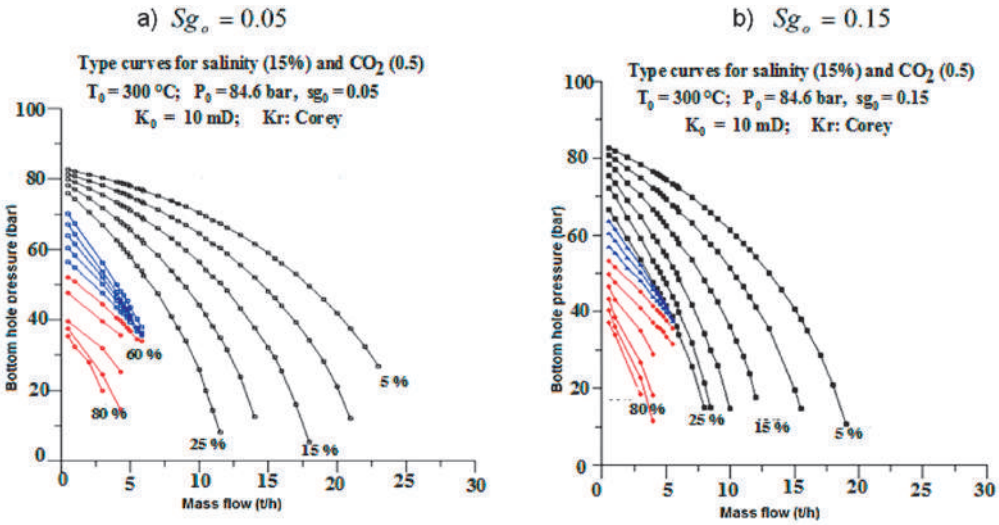

Figure 3. Type-curves of mass productivity as a function of the initial gas saturation and 15% salinity by weight.

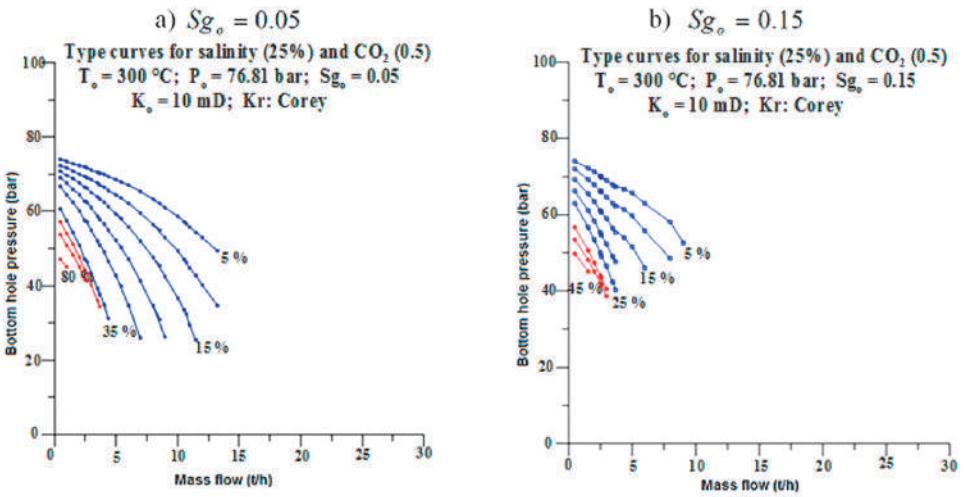

Figure 4. Type-curves of mass productivity as a function of the initial gas saturation and 25% salinity by weight.

initial gas saturation of 45%, the transition zone covers from the start of the exploitation of the well until 65% of cumulative mass produced.

The reduction of the zones without salt precipitation becomes steeper as the initial salt concentration increases, disappearing completely for the 25% salinity case at the four initial gas saturation conditions studied (Figure 4). Conversely, as the initial salinity concentration increases, the transition and salinity precipitation zones appear at earlier stages, similar to the case when the initial gas saturation increases.

For all the cases the curves of the transition zones are cut when high pressure drops appear. The competition of the two phases to flow and the increment in salinity concentration makes the numerical solution challenging, congruently to the physics reality. Meza (2005) obtained a full type-curve in the transition zone for 75% of cumulative mass produced, with the salinity precipitation starting at high values of pressure drops The salinity concentration considered by Meza (2005) was of 10% by weight and all the cases in that study correspond to 0.5% initial gas saturation. For this salinity concentration, the maximum reduction in permeability found by Meza (2005) was of 24% relative to the initial value of 10 mD. At the beginning of the precipitation the gas saturation was 82%.

The curves of the salinity precipitation zones are also cut for high value pressure drops. The truncation occurs when the salinity deposes in the rock formation, for certain critical conditions, leading to a drastic reduction in its porosity and permeability, according to Eq. (4) of the Verma and Pruess (1988) model.

A summary of all the characteristics of the salinity precipitation zones for the three cases of salinity concentration as function of the initial gas saturation is shown in Table 3; including other cases which were not graphically shown. For each initial gas saturation, the intervals of cumulative mass produced in which the precipitation occurs are specified, along with the total reduction in permeability of the rock formation. Moreover, the corresponding gas saturation in the same precipitation interval is specified. For the cases of 5 and 15% of initial salinity concentration, no complete obstruction of the pores of the rock formation occurs. The maximum reductions in permeability found were of 12 and 39% respectively; without being significantly affected by the initial gas saturation. Congruently, Meza (2005) obtained complete curves at salinity precipitation zones with maximum reductions of 10 and 40% for the same initial salinity concentrations but with a 0.005 initial gas saturation.

Complete obstruction of the pores is observed for the case of 25% salinity by weight (Figure 4; Table 3). This obstruction leads to a reduction of 100% in the permeability of the rock formation, occurring at earlier stages as the initial gas saturation increases. A reduction in permeability of 100% implies that the saturation of solids (precipitated salts) reached a value of 0.2, according to the tubes in series model of Verma and Pruess (1988); considering $\emptyset_C = \tau = 0.8$.

Conclusions

The inflow type-curves obtained in this study show the behavior of the mass productivity that may occur in a geothermal field as a function of their thermophysical parameters at different initial conditions of concentration of dissolved salts and gas saturation in the mixture.

Three well delimited zones were identified in the obtained type-curves: a) zones without salts precipitation; b) transition zones; and c) zones with salts precipitation.

It is concluded that with higher initial salts concentration and with increased gas saturation, the productivity of the well greatly decreases due to the difficulty to extract the fluid from the reservoir caused by the precipitation of salts. The precipitation of salts reduces the permeability of the rock formation and can reach critical conditions obstructing the flow in the reservoir.

The reduction in permeability is not significant for the case of lowest salt concentration (5%), independently of the initial gas saturation.

Table 3. Permeability reduction for different conditions of salinities precipitation.

	Salinity concentration (% by weight)					
	5%		15%		25%	
Sg_0	Precipitation range (cumulative mass produced)	Reduction of K (range of S_g)	Precipitation range (cumulative mass produced)	Reduction of K (range of S_g)	Precipitation range (cumulative mass produced)	Reduction of K (range of S_g)
0.05	85	10.0 – 9.7 (0.92 – 0.99)	60-80	9.7 - 6.3 (0.72 – 0.95)	40-50	3.3 – 0 (0.40- 0.67)
0.15	70-80	9.7 - 9.0 (0.87 – 0.98)	55-80	9.7 - 6.1 (0.67 – 0.95)	35-45	3.1 – 0 (0.48 – 0.70)
0.30	75-85	9.8 - 9.0 (0.88 – 0.98)	50-80	9.7 - 6.2 (0.70 – 0.95)	25-35	4.4 – 0 (0.50 – 0.69)
0.45	70-85	9.6 - 8.8 (0.90 – 0.99)	45-80	9.3 - 6.7 (0.74 – 0.96)	20-25	1.1 – 0 (0.58 – 0.67)

However, the effect becomes evident as the initial salts concentration increase, reaching complete obstruction of the pores for case of highest salts concentration (25%).

The use of these type-curves could become a complementary tool for the analysis of the productivity of the wells and for the selection of proper strategies for the correct exploitation of geothermal fields.

Acknowledgements

The authors thank CONACYT (Consejo Nacional de Ciencia y Tecnología), CENIDET-TecNM, and INEEL, for the support given for the development of this project. Also many thanks to Dra. Rosa M. Barragán whose observations improved the work quality.

References

Aragón A., 2006, La Influencia del Factor de Daño en Curvas-Tipo de Influjo Geotérmico y su Impacto en el Diagnóstico de Permeabilidades. PhD Thesis, CENIDET, Mexico. 103 pp. In Spanish.

Aragón A., Moya S.L., García-Gutiérrez A., Arellano V., 2008, A new method of damage determination in geothermal wells from geothermal inflow with application to Los Humeros, Mexico. *Geofísica Internacional* 47, 4, 371-382.

Aragón A., Barragán R.M., Arellano V., 2013, Methodologies for analysis of productivity decline: A review and application. *Geoth*., 48, 69–79.

Baba A., Demir M.M., Koc G.A., Tugcu C., 2015, Hydrogeological properties of hyper-saline geothermal brine and application of inhibiting siliceous scale via pH modification. *Geoth.,* 53, 406-412.

Battistelli A., Calore C., Pruess K., 1993, A fluid property module for the TOUGH2 simulator for saline brines with non-condensible gas. *In* Proceedings of 18th Workshop on Geothermal Reservoir Engineering, Stanford, Calif. USA, pp. 249-259.

Battistelli A., Calore C., Pruess K., 1995, Analysis of salt effects on the depletion of fractured reservoir bloks. *In* Proceedings of World Geothermal Congress, 3, 1613-1618.

Battistelli A., Calore C., Pruess K., 1997, The simulator TOUGH2/EWASG for modelling geothermal reservoirs with brines and non-condensibles gas. *Geoth*., 26, 4, 437-464.

Bernard-Romero R.A., Taran Y.A., 2010, Geochemistry of boron in fluids of LosHumeros and Los Azufres hydrothermal system, México. *In* Water Rock Interaction, 145-148.

Cramer S.D., 1982, The solubility of methane, carbon dioxide and oxygen in brines from 0 to 300° C. Report 8706, U.S. Department of the Interior, Bureau of Mines, 16 pp.

Demir M.M., Baba A., Atilla V., Inanlı M., 2014, Types of the scaling in hyper saline geothermal system in northwest Turkey. *Geoth*., 50, 1-9.

Flores J., 2007, Efecto de la saturación inicial de gas de un fluido en el diagnóstico de la permeabilidad en medios porosos. MSc Thesis, CENIDET, México, 69 pp. In Spanish.

Gilbert W.E., 1954, Flowing and gas-lift well performance. Drilling and Production Pract., API, 126 pp.

Iglesias E.R., Moya S.L., 1990, Geothermal inflow performance relationships. *In* Geothermal Resources Council Trasactions 14, II, 1201-1205.

Iglesias E.R., Moya S.L., 1992, An Accurate Formulation of the Solubility of CO_2 in Water for Geothermal Applications. Proceedings 17th Workshop on Geothermal Reservoirs Engineering, Standford University, pp. 231-238

Iglesias E.R., Moya S.L., 1998, Applicability of geothermal inflow performance reference curves to CO_2-bearing reservoirs. *Geoth*., 27, 3, 305-315.

Klins M.A., Majtcher M.W., 1992, Inflow performance relationship for damage or improve wells producing under solution gas drive. *J. Pet. Technol*., 44, 12, 1357-1363.

Lu X., Watson A., Gorin A.V., Deans J., 2006, Experimental investigation and numerical modelling of transient two-phase flow in a geysering geothermal well. *Geoth*., 35, 409-427.

Meza O., 2005, Efecto de la precipitación de sal en el diagnóstico de la permeabilidad en las formaciones rocosas. MSc Thesis, CENIDET, México, 117 pp. In Spanish.

Montoya D., 2003, Estimación de la permeabilidad de yacimientos geotérmicos a través de la application de las curvas-tipo de influjo geotérmico. MSc Thesis, CENIDET, México, 112 pp. In Spanish.

Moya S.L., Iglesias E.R., 1992, Carbon bioxide solubility in water in geothermal conditions. *Geofísica Internacional*, 31, 3, 305-313.

Moya S.L., 1994, Efecto del bióxido de Carbono sobre el transporte de masa y energía en yacimientos geotérmicos. PhD Thesis, Universidad Nacional Autónoma de México, UNAM, 204 pp. In Spanish.

Moya S.L., Aragón A., Iglesias E.R., Santoyo E., 1998, Prediction of mass deliverability from a single wellhead measurement and geothermal inflow performance reference curves. *Geoth*., 27, 3, 317-329.

Moya S.L., Uribe D., 2000, Computational system to estimate formation permeabilities by superposition of the well inflow curve with geothermal inflow type curves. *In* Proceedings of World Geothermal Congress 2000, Kyushu-Tohoku, Japan, 2731-2737.

Moya S.L., Uribe D., Aragón A., García A., 2001. Formation permeability at the feedzone of geothermal wells employing inflow type-curves. *Geofísica Internacional*, 40, 3, 163-180.

Moya S.L., Uribe D., Montoya D., 2003, Computational system to estimate formation permeabilities and output curves of geothermal wells. *Comput. Geosci.*, 29, 9, 1071-1083.

Narasimhan T.N., Witherspoon P.A., 1976, An integrated finite difference method for analyzing fluid flow in porous media. *Water Resour. Res.*, 12, 1, 57-64.

Newton R.C., Manning C.E., 2002, Experimental determination of calcite solubility in H_2O–NaCl solutions at deep crust/upper mantle pressures and temperatures: Implications for metasomatic processes in shear zones. *Am. Mineral*., 87, 1401–1409.

Pritchett J.W., 1993, Preliminary study of discharge characteristics of slim holes compared to production wells in liquid-dominated geothermal reservoirs. *In* Proceedings of 18th Workshop on Geothermal Reservoir Engineering, Stanford, Cal. USA, 181-187.

Pruess K., 1988, SHAFT, MULKOM, TOUGH: A set of numerical simulators for multiphase fluid and heat flow". GEOTERMIA, Rev. Mex. Geoenergía, 4, 1, 185-200.

Pruess K., Oldenburg C., Moridis G., 1999, TOUGH2 User's guide, Version 2.0, Report LBNL-43134, University of California.

Pruess K., García J., 2002, Multiphase flow dynamics during CO_2 disposal into saline aquifers. Environ. Geol., 42, 282-295.

Sanyal S., Steven K., Enedy L., 2011, Fifty years of power generation at The Geysers geothermal field, California - the lesson learned. *In* Proceedings of 36th Workshop on Geothermal Reservoir Engineering, Stanford, Cal. USA, pp. 41-49.

Verma A., Pruess K., 1988, Termohydrological conditions and silica redistribution near high-level nuclear wastes emplaced in saturated geological formations. J. Geophys. Res., 93, 1159-1173.

Vogel J.V., 1968, Inflow Performance Relationships for solution-gas drive wells. *J. Pet. Technol*., 20, 1, 83-92.

Geofísica Internacional (2017) 56-4: 345-358

Original paper

DC resistivity investigation in a fractured aquifer system contaminated by leachate from an old dump

César Augusto Moreira, Carolina Gonçalves Leandro, Camila Trindade Lopes and Lenon Melo Ilha

Received: August 02, 2016; accepted: August 30, 2017; published on line: October 01, 2017

Resumen

Los basureros son zonas de depósito final de desechos sólidos directamente en el suelo, en ausencia de criterios técnicos o sistemas de recolección de gases o líquidos. Una gran parte de los municipios brasileños han utilizado esta alternativa extremadamente perjudicial para el ambiente hasta el año 2010, cuando una ley federal hizo obligatoria la instalación de rellenos sanitarios. Sin embargo, una gran parte de los basureros fueron simplemente abandonados, aunque algunos finalmente tuvieron algún tratamiento después de las evaluaciones de los organismos ambientales. Este trabajo presenta los resultados de la investigación geofísica en un basurero cerrado en 2004 en una pequeña ciudad del sur de Brasil, donde las investigaciones anteriores revelaron contaminaciones del suelo y de las aguas subterráneas por lixiviación. Los análisis estructurales en la región de estudios vinculados a datos geológicos de pozos de monitoreo indican la presencia de contaminantes en la fractura de granito, con amplias variaciones en el espesor del suelo, saprolita y el nivel del agua subterránea. La integración del análisis químico de las aguas subterráneas con los datos de la tomografía eléctrica (ERT) en el procesamiento de imágenes 2D y 3D, reveló la existencia de grandes áreas contaminadas dentro de los límites del basurero y el flujo en el acuífero parcialmente libre hasta 5m de profundidad. Estas zonas pueden disminuir gradualmente con el aumento de la profundidad y entre 9m y 19m predominan zonas contaminadas claramente orientadas, asociada con el flujo en el acuífero fracturado. La indicación de zonas restringidas y dirigidos sugiere la focalización y la acumulación de contaminantes en los dos sistemas de fracturas preferenciales. El descubrimiento de estas áreas es esencial para la planificación y la instalación de sistemas de bombeo y de descontaminación de aguas subterráneas, en vista de la disminución de la producción de lixiviado desde la clausura del basurero.

Palabras claves: materia orgánica, lixiviado, contaminación, acuífero fracturado, tomografia eléctrica.

César Augusto Moreira
Geosciences and Exact Sciences Institute
Univ. Estadual Paulista
Av. 24-A, 1515, Bela Vista. ZIP 13506-900
Rio Claro, São Paulo State, Brazil
*Corresponding author: moreira@rc.unesp.br

Carolina Gonçalves Leandro
Camila Trindade Lopes
Lenon Melo Ilha
Pampa Federal University – UNIPAMPA
Av. Pedro Anunciação, s/n
Vila Batista. ZIP 96570-000
Caçapava do Sul, Rio Grande do Sul State, Brazil

Abstract

The dumps are areas of final disposal of solid wastes directly into the soil, with no technical criteria or collecting systems of gases or liquids. A large part of Brazilian municipalities have used this extreme damaging alternative to the environment up to the year 2010, when a federal law made compulsory the installation of sanitary landfills. However, large parts of the dumps were simply abandoned, although some eventually go through treatment after assessments of the state environmental agencies. This work presents the results of a geophysical investigation in a dump deactivated in 2004 in a small city in southern Brazil, where previous investigations have revealed contamination of soil and groundwater by leachate. Structural analyzes in the area of study combined to geological data from monitoring wells indicate the presence of contaminants in fractured granite, with a wide variation in the thickness of soil, saprolite and groundwater level. The integration of chemical analyses of the groundwater with electrical resistivity tomography (ERT) in 2D and 3D processing, revealed the existence of large contaminated areas within the limits of the dump flowing into the aquifer partially free up to 5m depth. Such areas may decrease gradually with the increase in depth and between 9m and 19m contaminated zones clearly predominate, associated with the flow in the fractured aquifer. The indication of restricted and oriented zones suggests the targeting and accumulation of contaminants in two systems of preferential fractures. The discovery of these zones is fundamental for planning and the installation of pumping and decontamination systems of groundwater, considering a declining production of leachate since the closure of the dump.

Palabras clave: organic matter, leachate, contamination, fractured aquifer, electric resistivity tomography.

Introduction

The intense process of urbanization started around 1960 in Brazil, was driven by the installation of several foreign automobile manufacturers, substantial investments in electricity generation and expansion of university education. The absence of urban planning has resulted in the use and occupation of the urban space in a disorderly way, with negative consequences in terms of urban mobility, basic sanitation and quality of life.

This process was accompanied by changes in consumption habits, which stimulated by means of intense advertising and encouragement in unbridled consumerism, has resulted in the expansion and the generation of waste in its different forms. The main form of final disposal of solid waste in Brazil are the sanitary landfills (59%), controlled landfills or dumps (41%), whose collection and final disposal are the responsibility of the municipalities. (IPEA, 2012; SNIS, 2013).

The organic matter generated in houses represents more than 50% of the mass of garbage collected, caused primarily from food waste, with maximum use of 3% of this material in composting (CEMPRE, 2013; ABRELPE, 2014).

The dumps are a form of packaging of waste which is characterized by its location is distant areas of urban centers, absence of any system of collection of gases or liquids produced by decomposition of organic materials, lack of coverage on the surface or soil sealing besides the lack of control on the proliferation of insects, rodents and birds that use these areas as a source for feed and shelter (Christensen, 2001; Tchobanoglous and Kreith, 2002; Reddy, 2011).

The absence of technical criteria in the planning of operation of these areas provides a broad spectrum of impacts on the environment: contamination of soil, groundwater and drainage due to gravity flow of leachate coming from the decomposition of organic waste, emissions of greenhouse gases (CH_4, CO_2); the risk of explosion by the accumulation of flammable gases (CH_4); risk of animals killing, plants and aquatic beings on the outskirts of the area; proliferation of serious human diseases caused by exposure to chemicals (metallic elements, organic and inorganic) and biological (virus, bacteria and fungi), among others (Tchobanoglous *et al*., 1993; Vesilind 2002).

In 2010 the National Policy for Solid Residues was implemented in Brazil by means of Law nr. 12.305 of 2010 (BRAZIL, 2010). This standard proposes the management of residues in face of a new system based on present concepts, explicit specifications and terms for implementation and regulation. This juridical instrument stipulated a term of 4 years, ended in 2014, for the banishing of procedures for

waste disposition without technical criteria, or conversion of dumps into sanitary landfills.

In the face of legal requirements, in 6 years of validity of this federal regulation (2010-2016), approximately 60% of Brazilian municipalities have discarded household solid waste in landfills, in addition to the deployment of several actions for the reduction, reuse and recycling of waste, in an attempt to minimize the total volume of waste to be placed in landfills.

However, the adoption of actions and technical projects of treatment and recovery of the deactivated dumps is a recurring theme, which requires investment and action plans highly complex in some cases. Several small municipalities do not have the technical and financial resources for detailed studies. Partnerships between municipalities and universities are viable alternatives, inexpensive and suitable for coping with these issues.

The degree of technical difficulty in these cases is conditioned to issues such as: volume of waste conditioning, time of use of the area, proximity of drainage, slope, thickness and mineral constituents of the soil, composition of the bedrock, type and depth of the aquifer, porosity, permeability, among others (Lehr *et al*., 2001; Sara, 2003; Twardowska *et al*., 2006; Hernández-Soriano, 2014; Yung-Tse *et al*., 2014).

Special features related to environments with soil not very thick, exhibitions of rock on the surface and fractured groundwater aquifers, are elements that represent a highly complex geological environment, requiring differentiated negotiations regarding the diagnosis and planning of technical proposals for the recovery of contaminated areas.

Quantitative determinations about the levels and dispersion of contaminants in groundwater demand direct sampling by means of monitoring wells. However, the misplaced location of drilling points and sampling in fractured aquifer systems can induce the development of inadequate technical projects, with unsatisfactory results in terms of economy and efficiency.

Preliminary diagnostics by means of indirect procedures for research are highly advantageous in those cases where the application of geophysics shows satisfactory results in the investigation of a wide range of types of contaminants and diversity of geological contexts (Knödel *et al*., 2007, Rubin and Hubbard, 2005). The contrast of electrical properties characteristic of inorganic pollutants such as leachate when present in soils and rocks, justifies the adoption of Electrical and Electromagnetic geophysical methods in these cases (Meju, 2000; Shevnin *et al*., 2005; Chambers *et al*., 2006; Dena *et al*, 2012; Belmonte-Jiménez *et al*., 2012 EN LISTADO DE REFERENCIAS; Moreira *et al*., 2013; Delgado-Rodríguez *et al*., 2014; Ochoa-González *et al*., 2015; Moreira *et al*., 2016; Arango-Galván *et al*., 2016).

This paper presents the results of geophysical research in a deactivated garbage dump and currently under technical evaluation for preparation of integrated management, which involves new conformation of the relief, planting of grasses and trees, in addition to the remediation of contamination in the aquifer. From previous geochemical studies that demonstrate the contamination of the aquifer, the data analysis of electrical resistivity tomography (ERT) in 2D and 3D visualization products, aims to define the main zones of flow in a context of fractured aquifer, in addition to enabling the planning of technically effective remediation devices appropriate to the complexity of the local geological environment.

Location and history of the study area

The city of São Sepé is located in the central region of Rio Grande do Sul State, South of Brazil, having 23.798 inhabitants, with economy based on rice growing and extensive livestock farming (IBGE, 2010).

The area of the former municipality garbage dump has a total of 10.318m², with activities that started in 1989 and finished in 2004. Between 1989 and 1998, this area functioned as a garbage dump in the open air, where the urban solid waste was launched without any planning. The establishment of minimum technical criteria requirements from 1998 resulted in the release of waste into windrows, compacted by the transit of a track tractor and later covering of soil, although without the installation of any systems of waterproofing basement, collection of gases or liquids. The total volume of residues disposed in the area is estimated at 6.000.00 m³.

The site was closed to the launch of waste in 2004 and went on to serve as an area of transshipment of waste for final disposal in sanitary landfill in the Minas do Leão city. The area was finally closed in 2007, with a history of environmental and social issues, with invasion and housing of collectors of recyclable

materials, waste incineration in the open air, with soil and groundwater contamination, and various violations of federal and state laws.

After summons and lawsuits, the municipal government has signed an agreement for the remediation of the area with the FEPAM (Rio Grande do Sul Environment Agency) in 2015. The initial studies counted with the installation of four monitoring wells for chemical analysis and verification of environmental impacts on the aquifer (Figure 1).

The regional geological context is represented by the São Sepé Granitic Complex, positioned at the northern end of the western portion of the Sul-Riograndense Shield (CPRM, 2000). The various constituent rocks are dated around 542±6Ma by U-Pb in zircon (Remus *et al*., 1997), a period corresponding to the Brasiliano orogenic cycle, tectono-magmatic responsible for intense genesis of granites recognized in various portions of the Brazilian territory (Bizzi *et al*., 2003).

The São Sepé Granitic Complex features elongated shape toward NE/SW, partially covered by sedimentary units, having dimensions of a batholith (Sartori & Rüegg, 1979). It is characterized by an acid intrusion with a wide variety of textures and reverse zonation with monzongranites in the central part and syenogranites in outlying areas (Gastal & Ferreira, 2013).

These rocks have brown-reddish color, granulation medium to coarse, and variations dominantly equigranular to porphyritic. In peripheral positions, microgranites and aplites occur in the form of dikes with fine granulation tissue, associated with quartz milky millimeter single or in swarms, which represent late magmatic manifestations. The quartz veins are centimeter to millimeter thickness and appear singly or in swarms (Sartori & Rüegg, 1979).

The regional character of structural context is defined by the predominance of fractures and faults groups in different positions in batholith granite. Directions N60° to N70° are predominant in the eastern end, in the west central portion directions between N50° and N55°predominate, in the east portion dominates the direction N25° to N40° and N115° to N130° (Gastal & Ferreira, 2013).

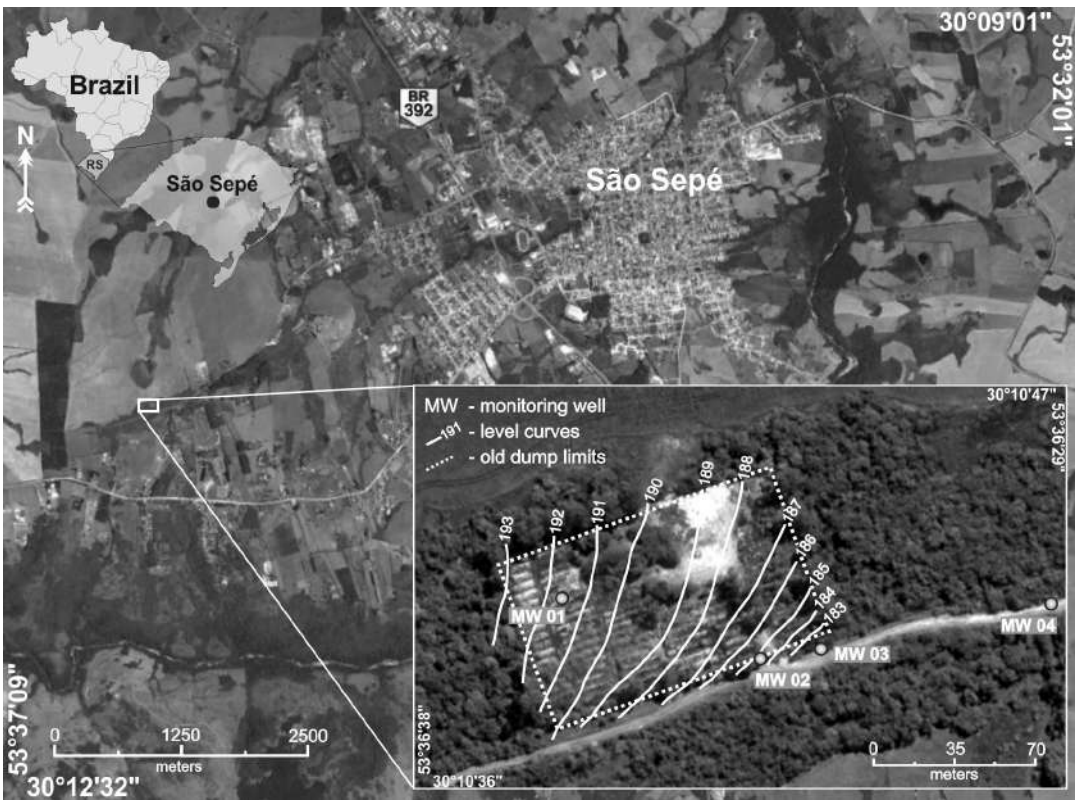

Figure 1. Location of the study area, with monitoring wells and level curves.

The location of studies is contained in the extreme northeastern part of the granitic batholith, characterized by discontinuities that are primarily oriented between N20°, N35°, N150° and N165° with clear indications of fracture joints. However, the structural discontinuity closest to the area of studies has N68° direction.

Locally it is possible to recognize the presence of soil with clay texture, with fragments of quartz, with a thickness that can reach up to 3m, as well as various surface granite exposures, with the presence of fractures and joints, and quartz in veins (Figure 2).

Initial studies of research for preparation of a remediation counted on the installation of four monitoring wells, by means of which it was possible to define the thickness of soil and groundwater level.

Well MW - 01 was placed in one of the highest places in the area, positioned at 191.7m of altitude and presented about 2m layer of soil and saprolite, with 0.84 m of additional fractured rock positioned 2.84m deep from the groundwater level. Well MW - 02 is positioned at 185m altitude and has about 0.25m thickness between soil and fractured rock, with basal contact that defines the position of groundwater level. Well MW - 03 is positioned at 182m altitude and 30m from well MW - 02, with approximately 1.45m layer of soil and saprolite, and 3.90m interval of fractured rocks, with the groundwater level positioned at 5.35m (Figure 3).

Well MW - 04 is positioned at approximately 100m from the area of study, scheduled to serve as a reference pattern for chemical groundwater analyses. It has a 3.00m layer of soil and saprolite, in addition to approximately 7.05m thick layer of fractured rocks, with the groundwater level positioned at 10.05m depth (Figure 3).

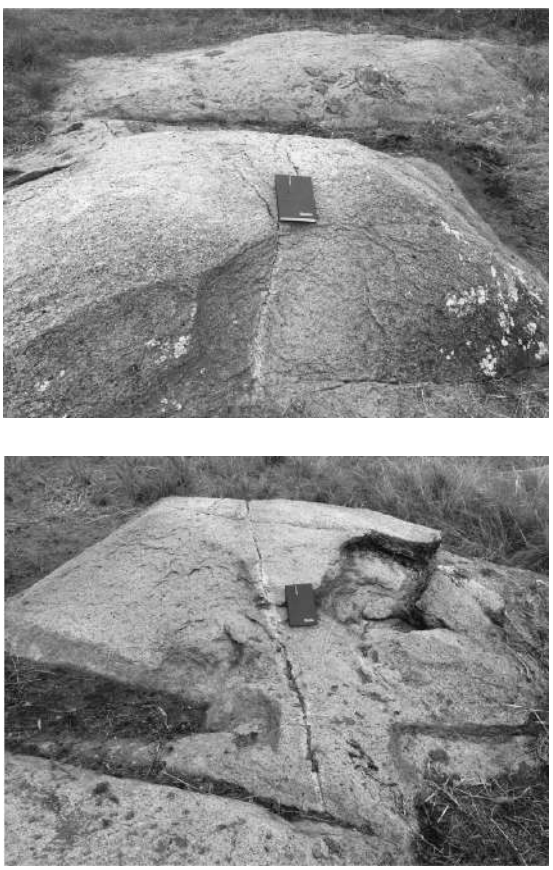

Figure 2. Fractured granite outcrops in old dump.

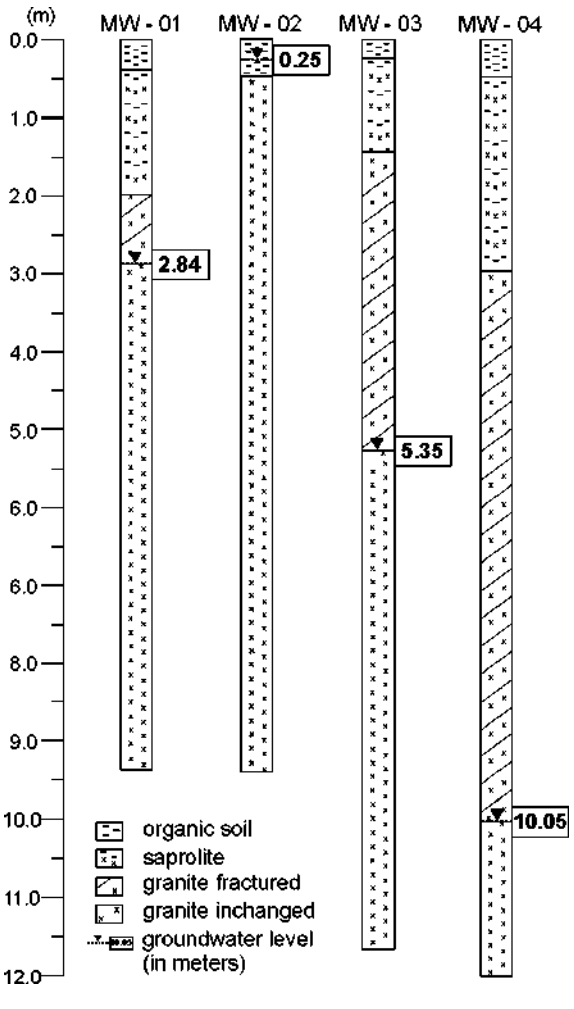

Figure 3. Geological profile of the monitoring wells, with groundwater levels.

Chemical analyses in water samples collected in the set of wells installed in the area reveal changes in various parameters analyzed, with results above the Brazilian Standards (Table 1).

The geochemical anomalies related to the metallic elements such as lead, iron, manganese and aluminum, can be associated with the weathering of sulphide ores and micas, contained in quartz veins outlined in various exhibitions of the São Sepé Granite, resulting from hydrothermal processes occurring in the final stages of magmatic crystallization (Matos *et al,* 2004; Gastal & Ferreira, 2013).

However, it is notable the significantly increased levels of iron, manganese, mercury, nitrate and conductivity in well MW-03, in addition to other geochemical anomalies in the other wells. The pH variation is also relevant in terms slightly acid (between 6.04 and 6.96) and the very high levels of sodium, sulphate, nitrate and total alkalinity. However, the vast majority of elements analyzed occur at values below the limit of contamination stipulated by the federal law.

Materials and methods

The selection of the DC Resistivity geophysical method is based on history of use and occupation, coupled with previous data obtained through the monitoring wells, in addition to the contrast of electrical properties provided by the eventual presence of leachate in the soil and aquifer on comparisons with measurements of references to natural conditions for the area (Georgaki *et al*., 2008; Moreira *et al*., 2015).

Electric Resistivity Tomography (ERT) was used in a dipole-dipole array. The existence of fractures and faults with a high angle in the region and the possibility of contaminant flow in these locations, justified the selection of this dipole-dipole array. This array is characterized by the contrast of spread in electrical and potential fields, sensitivity and highlight in the recognition of similar structures (Arango-Galván *et al*., 2016; Delgado-Rodríguez *et al*., 2014; Moreira *et al*., 2016).

This array consists in the installation of pairs of metal electrodes along the line of research, for transmission of electric current and generation of electric field in depth (current electrodes), and later reading through pairs of reception electrodes (potential electrodes). The appropriate form of current and potential electrodes positioning allows to record electrical resistivity for different depth levels in the investigated line (Telford *et al.*, 1990; Milson & Erikssen, 2011).

The data acquisition in the field was based on the following settings: 5m spacing between electrodes and measurements of electrical resistivity in 20 depth levels. Nine lines of electrical resistivity tomography routing were performed, five lines being 110m and four lines 160m extension, placed in mesh with spacing of 25 m between them (Figure 4).

Table 1. Chemical analyzes in the groundwater samples

Limit *	MW-01	MW-02	MW-03	MW-04	
Aluminium	0.2	1.39	1.330	1.776	0.78
Cadmium	0.005	<0.0006	<0.0006	<0.0066	<0.0006
Lead	0.010	0.051	0.042	0.044	0.041
Chloride	250	21.8	32.7	102	4.04
Condutivity	-	518.4	899.7	1129.7	76.08
Chrome	0.05	0.06	<0.003	<0.003	<0.003
Iron	0.300	3.473	1.076	3.318	0.783
Manganese	0.100	0.720	0.530	1.691	0.529
Mercury	0.001	0.0003	0.0038	0.0016	<0.0002
Nitrite	1.0	<0.006	0.530	1.691	0.529
pH	-	6.96	6.45	6.49	6.04
Sodium	200	35.8	54.5	104	4.54
Total dissolved solids	1000	342	594	732	44
Sulfate	250	30.5	74.6	67.8	1.14

*Defined by CONAMA 396/08
(National Counsel of Environment - Ministery of Environment - Brazil)

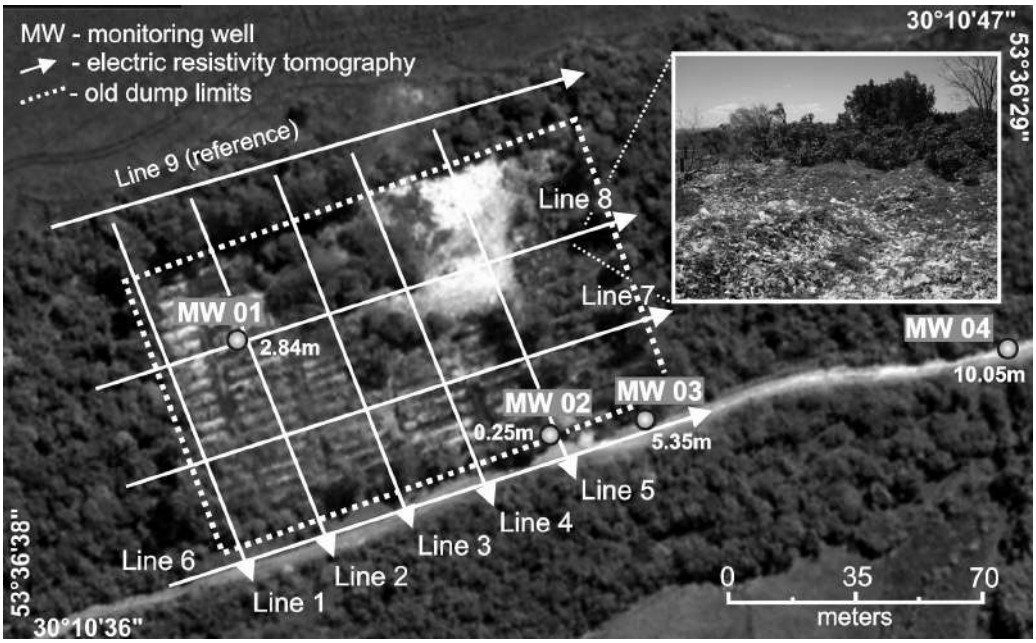

Figure 4. Electrical resistivity tomography lines and monitoring wells, with detail of residues exposed and groundwater level (in meters).

The positioning of the lines in the field considered the intersection of the main systems of fractures regionally recognized, in addition to the local topography and existing approaches in the area of study. It was possible to ascertain during the data acquisition in the field, that trees cover a large part of the waste and there are only some areas covered by grass allowing the recognition of partially exposed waste.

The equipment used was the resistivity meter Syscal Pro, manufactured by Iris (France) with a resolution of 1mV. This equipment is calibrated for measurements of resistivity through periodic cycles of alternating electric current and low frequency, a procedure that allows the filtering of noise from the acquired signal (IRIS Instruments, 2006).

The field measurements were initially processed with the software Res2Dinv, where, from the smoothed by inversion method (*smooth inversion*) bi-dimensional resistivity models were generated for the subsurface that consider the topography adjustment (Geotomo Software, 2013). The sections are presented in terms of distance x depth, with logarithmic graphic scale and intervals of interpolation of color values.

The method of inversion by smoothing uses the mathematical method of least squares, and through it, the software recognizes the terrestrial subsurface as rectangular blocks that have constant values for the investigated parameter (Geotomo Software, 2013). This optimization aims to reduce the difference between the apparent resistivity values, calculated and measured in the field, by adjusting the resistivity of the block model, whose difference is expressed by the RMS error (*Root Mean Squared*) (Loke & Baker, 1996).

After the 2D inversion, the data were gathered in single file, later used as a database for generating 3D maps and depth models. This process was developed in the Oasis Montaj platform, where the 2D data obtained with Res2Dinv program were interpolated and modeled by means of the minimum curvature method for enhancement of the extreme values in models of three-dimensional blocks, where the ERT lines were positioned. The works of Vieira *et al*., (2016) and Cortês *et al*., (2016) describe in detail the elaboration of 3D visualization models used in this work.

Results and discussion

An analysis of the main chemical and physical characteristics of the leachate from dumps and landfills is extremely important, often composed by several groups of pollutants (Christensen *et al*., 1994). These groups are: dissolved organic matter, expressed by the

demand of chemical oxygen or total organic carbon, including CH_4, volatile fatty acids and compounds more resistant as humic and fulvic; inorganic components such as Ca, Mg, Na, K, NH_4^+, Fe, Mn, Cl, SO_4^{2+} and HCO_3^-; heavy metals such as Cd, Cr, Cu, Pb, Ni and Zn; organic compounds derived from petroleum, which include aromatic hydrocarbons, phenols and aliphatic chlorinated.

The set of anomalous values described in the analytical results of groundwater samples in the site can be directly correlated to the percolation of leachate from the decomposition of organic matter, whose characteristic of acid pH also contributes to the dissolution and solubility of metals, eventually contained in waste or minerals from bedrock that support the aquifer (Farquhar, 1989; Kjeldsen *et al*., 2002).

This saline solution that makes up a set of inorganic elements, organic and metal typical of leachate from garbage dumps and landfills, is completely miscible in water and reaches the aquifer initially by gravity flow, then conditioned to the gradient of groundwater flow. In this sense, the possible leachate presence on the aquifer is recognized by increasing the electrical conductivity (Meju, 2000; Knödel *et al*., 2007).

The analysis of 2D inversion models allows to recognize areas of low electrical resistivity, values below 150 Ohm.m, compared to the values of reference for the area, limited to150 Ohm.m minimum value (Figure 5).

The integration between the geophysical and geological data reveals the complexity of the geological environment of the area of study.

In the absence of previous geophysical surveys, the monitoring wells were drilled in the area according to the topographical criterion, i.e. MW-01 well was placed in the highest part of the area, followed by wells of lower elevation. This criterion was apparently based on the principle of a groundwater flow gradient parallel to the topography.

The weathering intensified by water infiltration and hydration of the rock forming minerals in the fracture plans contrasts with the process that applies at intervals of massive rock, occurring slowly and resulting in large blocks of rock. The differential weathering produces highly complex flow paths and the soil cover makes it difficult on the surface, to estimate groundwater flow or contamination of surface origin.

In the 2D inversion models a delimitation of the interval of 150 Ohm.m was possible, revealing a wide variation in lateral depth of the bedrock, responsible for supporting the aquifer, besides of discontinuities which hinder the communication in the lateral and vertical direction of the fluid. The differential weathering has provided an unconfined configuration system for the aquifer (lines 2, 3 and 7), aquifer partially confined (lines 1, 5 and 6) and fractured system (lines 1, 2 and 4). The vertical and side discontinuities should reflect the presence of bedrock in blocks between systems partially isolated from the fractured rock.

Due to the total miscibility of leachate in groundwater, the percolation of the pollutant in groundwater aquifer is subject to the elements of flow present in the area of study.

The lateral complexity in terms of structural, flow discontinuities, and their reflections in the pattern of groundwater flow can be analyzed from the integration of 2D models in 3D visualization models, for different depths.

Up to 5m depth a large area occurs with values related to the presence of leachate (below 150 Ohm.m), in a range where soil and saprolite predominate, with portions of high resistivity which indicate the presence of non-altered bedrock (values above 1500 Ohm.m) (Figure 6).

However, the analysis of geological and hydrogeological data of the wells profile reveals a great variation in thickness of soil, saprolite, fractured rock, depth of non-fractured rock and, as a consequence, in the position of the aquifer level. The great lateral variation on the groundwater level between wells MW-02 and MW-03 is a clear indicator in this sense.

At 9m depth a substantial reduction of areas of low resistivity occurs, concentrated in two distinct areas. From 13m there is a predominance of resistivity values, which indicate the growing predominance of bedrock, but with the existence of vertical fracturing which probably affects the groundwater flow towards greater depths. The range of low resistivity between 13m and 19m suggests a conic geometry with channeling of flow at depth, with a tendency to continuity below 19m (Figure 6).

The areas of low resistivity relating to the presence of leachate were modeled in isosurfaces of 50 Ohm.m, in an attempt to analyze three-dimensional architecture and

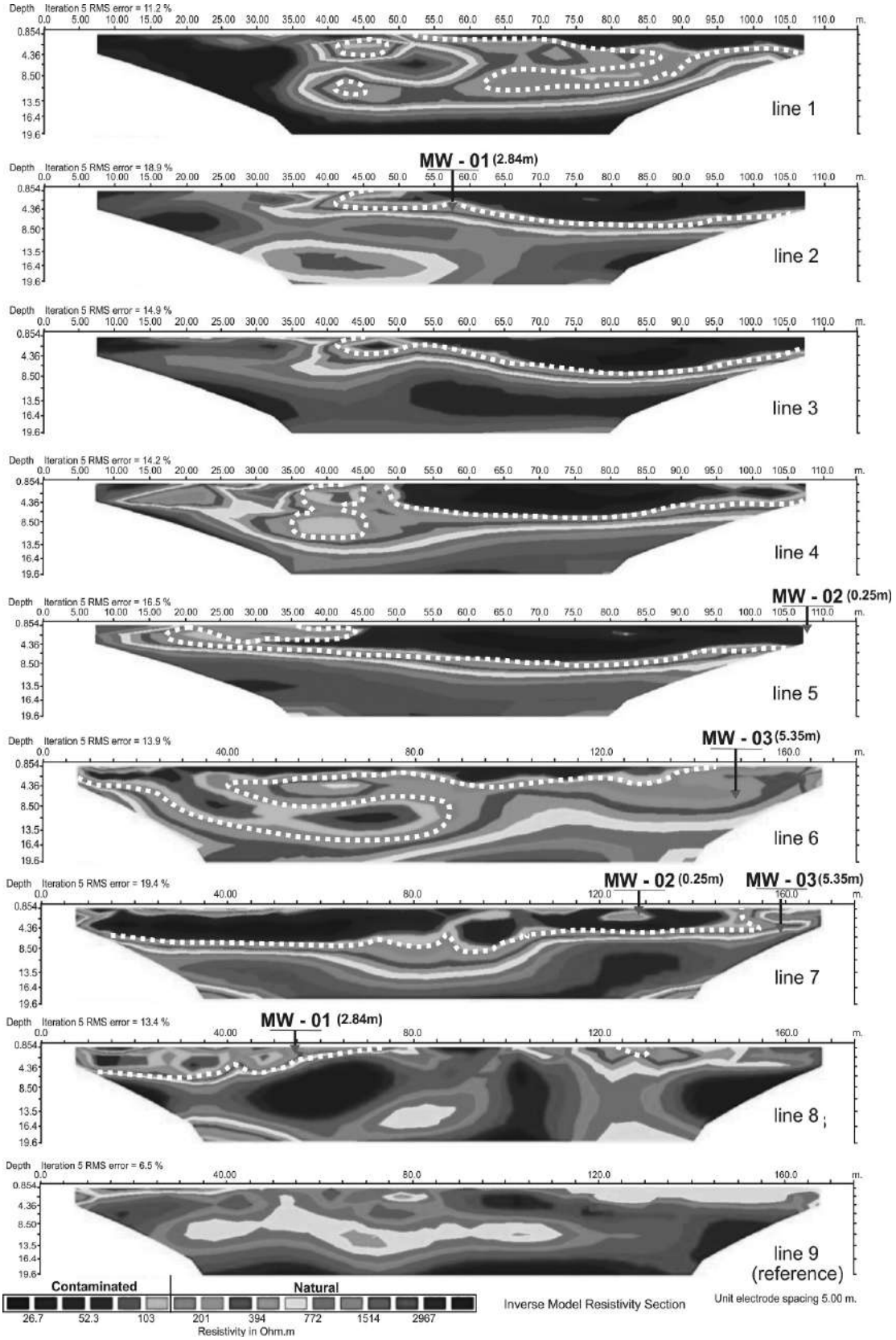

Figure 5. Inversion models of electric resistivity tomography, with limits of contaminated areas (white lines) and groundwater level in meters (red triangle).

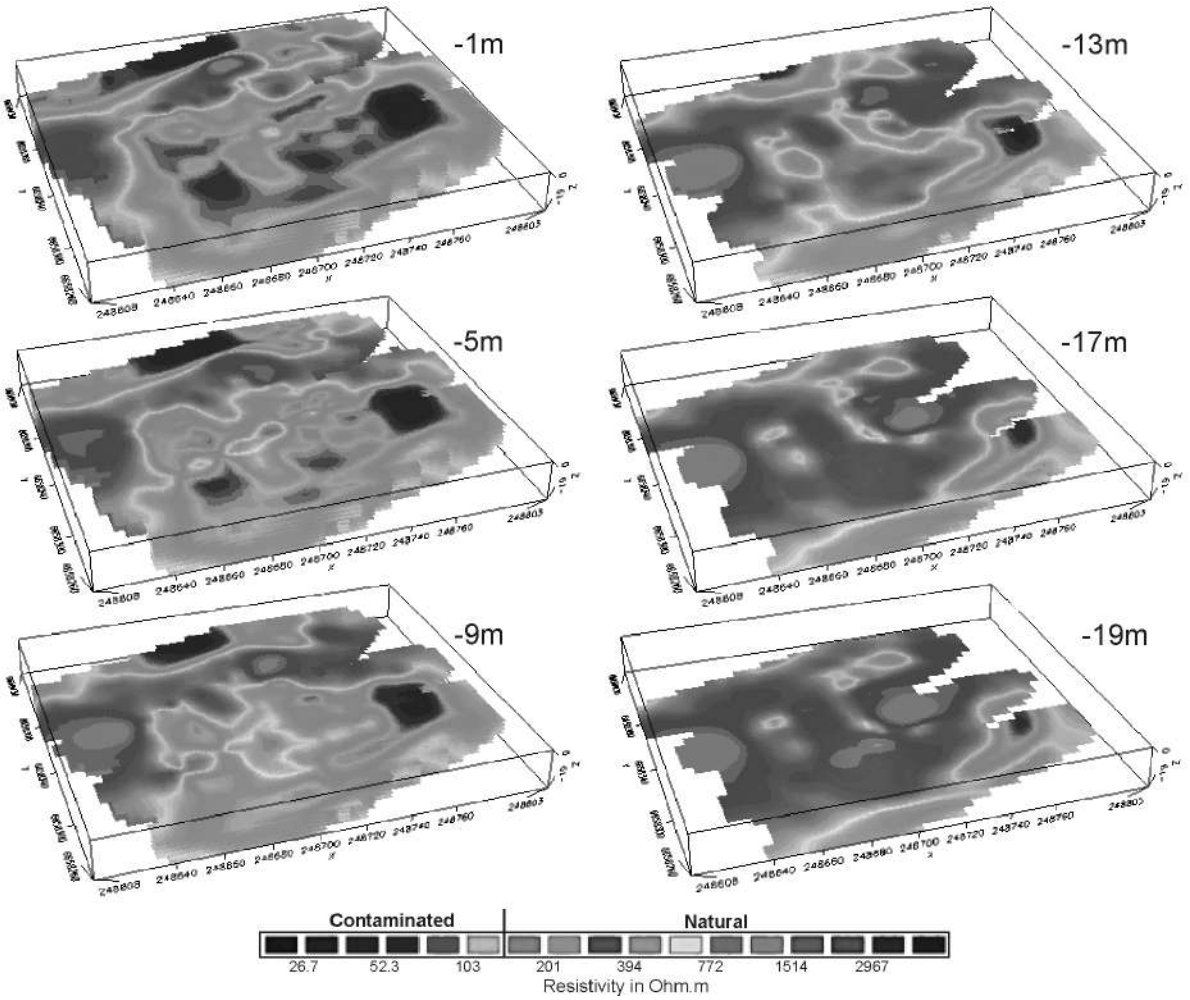

Figure 6. Resistivity maps for six distinctive depths.

its relations with the geological structures. The existing zone in the NW has an elongated shape in the N58° direction, conic geometry and a tendency to close at 13m depth (Figure 7).

The existing zone in the SE portion is also characterized by the tendency to closing at depth, although in this case, with ellipsoid shape and possibly conditioned to a system of joint fractures at N38° and N170° directions, which provides the shaping of isosurface modelling at 15m depth, but with an indication of flow beyond the maximum depth of geophysical investigation (Figure 7).

The position of the monitoring wells does not coincide with the areas of low resistivity, an indication of inadequate leasing of drilling. Well MW-01 presents, in comparison, the lowest levels of salts (sulfate, sodium, nitrate, chloride, total dissolved solids and electrical conductivity) (Table 1). This well was placed near the areas of bedrock outcrop, with shallow aquifer level and tending to lateral flow in the opposite direction to the well, as per crosschecks of data with line 8 (Figure 5).

Wells MW-02 and MW-03 were positioned near a zone of low electrical resistivity and have high levels of salts. Well MW-03 is very close to the area of low resistivity of the SE portion of the area and presents higher values of electrical conductivity and total dissolved solids as compared to well MW-02, more distant from this zone.

Conclusion and recommendations

Past issues about the deposition of household solid waste result in environmental problems today and require solutions in terms of research and technical planning in the management of

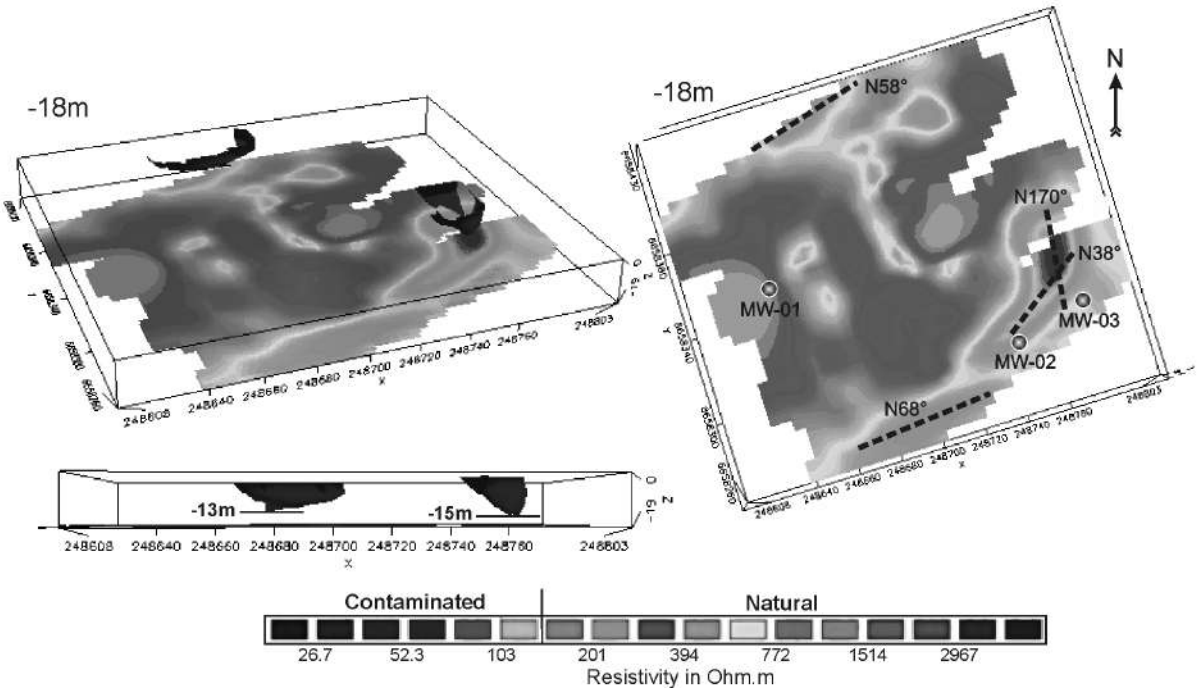

Figure 7. Resistivity map for -19m depth, with isosurface of the 50 Ohm.m, monitoring wells and directions of fracture planes

soil and groundwater contamination. Geological circumstances, such as groundwater flow in a fractured system and the complete miscibility of inorganic contaminants in groundwater, are factors that make the research and the treatment planning actions of these areas something substantially complex.

Preliminary investigations in the area of study consisted of a history of use and occupation of the area, followed by the installation of four monitoring wells, for determining the thickness of soil and rock horizons, depth of the aquifer level and water collection for chemical analyses. The wells were aligned according to the local slope, based on the premise that groundwater flows on a surface parallel to the topography.

Joint analyses of regional structures and local geology revealed the high local hydrogeological complexity due to the existence of a system of structural discontinuities in a granite batholith, set that supports an aquifer partially unconfined and partially fractured. The variation in the degree of weathering between fractured and massive areas resulted in thicknesses of soil and saprolite laterally variables, in addition to the existence of bedrock surrounded by soil. These factors provide a wide variation in the depth of the aquifer, as well as a migration from systems partially confined in the fractured system.

The analyses of 2D inversion models shows details about lateral variations and indicates the existence of a salt solution that makes the aquifer an electrical conductor in the dump area, when compared to natural data obtained in the reference line of natural electrical resistivity. Results of chemical analyses in monitoring wells showed changes in several parameters, with emphasis on elements that typically constitute the leachate, in addition to some metals possibly leached by acid attack in quartz veins, which has the potential of hydrothermal mineralization by sulfides in the bedrock.

The interpolation of tomographic sections in 3D visualization models, integrated with geological and structural data, provide a well-suited analysis of the groundwater flow. The ranges up to 5m depth are characterized by large areas of low resistivity associated with the leachate percolation in soil and saprolite, within a context of groundwater flow in a predominantly porous system. From 13m depth large areas of high resistivity dominate and isolated and targeted to low resistivity concentrations, possibly aligned in zones of

flow in the fractured system in granite, where it is possible to highlight two expressive zones positioned in portions NW and SE in the area. Modeling of these zones indicates a conical geometry with channeling of flow in depth related to fractures and joints of fractures.

The geophysical data reveal the inappropriate location of the monitoring wells due to disregard of groundwater flow in the fractured system, although they provide results that reveal the groundwater contamination. Proper planning for treating the contaminated area necessarily depends on direct investigations in order to prove the geophysical clues.

The geophysical results revealed the hydrogeological complexity on the site and the inadequacy of the procedure of direct investigation. The correlation of low resistivity areas with chemical analyses showed the contamination of the aquifer, The existence of preferential zones of flow and accumulation of leachate, showed the relevance and effectiveness of the method in the investigation of complex contaminated areas and in the planning of treatment actions.

Factors such as the closure of the area for final disposal of solid waste in 2004, the restriction of new contributions of organic matter and the action of processes of consumption and conversion of this material over the last 12 years, provide the increasing exhaustion of the generation source of leachate.

Based on the definition of preferential flow and the accumulation of leachate zones mainly in the context of the fractured rock, the installation of wells for pumping and treatment of contaminated water is recommended, in an attempt to restrict the pollutants flow and a progressive decontamination of the old dump area.

References

ABRELPE, 2014, Panorama dos resíduos sólidos no Brasil. Abrelpe, São Paulo, 120 pp.

Arango-Galván C., Flores-Márquez E.L., Hernández-Espriú J.A., Arias-Paz A., Sagahón-López E.J., 2016, Shallow geoelectrical characterization of a small portion of the Basin of Mexico aquifer: Towards a better resource management. *Geofísica Internacional*, 55, 3, 215-225.

Belmonte-Jiménez S., Jimenez-Castañeda M.E., Pérez-Flores M.A., Campos-Enríquez J., Reyes-López J.A., Salazar-Peña L., 2012, Characterization of a leachate contaminated site integrating geophysical and hydrogeological information. *Geofísica Internacional*, 51, 4, 309-321.

BRASIL, 2010, Lei n. 12.305 de 2010 - Política Nacional de Resíduos Sólidos. Governo Federal, Brasília.

Bizzi L.A., Schobbenhaus C., Vidotti R.M., Gonçalves J.H., 2003, Geologia, Tectônica e Recursos Minerais do Brasil - texto, mapas & SIG. CPRM, Brasília, 643 pp.

CEMPRE, 2013, Review. Cempre, São Paulo, 24 pp.

Chambers J.E., Kuras O., Meldrum P.I., Ogilvy R.D., Hollands J., 2006, Electrical resistivity tomography applied to geologic, hydrogeologic, and engineering investigations at a former waste-disposal site. *Geophys.*, 71:231-239.

Christensen T.H., 2001, Solid Waste Technology & Management. John Wiley and Sons, Ltd, Chichester, 1022 pp.

Christensen T. H., Kjeldsen P., Albrechtsen H. J., Heron G, Nielsen P.H., Bjerg P. L., 1994, Attenuation of landfill leachate pollutants in aquifers. Critical Review in *Environ. Sci. Technol.*, 24, 2, 119-202.

CONAMA – Conselho Nacional do Meio Ambiente, 2008, Resolução n° 396 de 3 de abril de 2008 - Dispõe sobre a classificação e diretrizes ambientais para o enquadramento das águas subterrâneas e dá outras providências. CONAMA, Brasília.

Côrtes Con z em linea 312 A.R.P., Moreira C.A., Veloso D.I.K., Vieira L.B., Bergonzoni F.A., 2016, Geoelectrical prospecting for a copper-sulfide mineralization in the Camaquã sedimentary basin, Southern Brazil. *Geofísica Internacional*, 55, 3, 107-117.

CPRM – Companhia de Pesquisa e Recursos Minerais, 2000, Folha Cachoeira do Sul, Rio Grande do Sul, Escala 1:250.000. CPRM, Brasília, 86 pp.

Delgado-Rodríguez O., Flores-Hernández D., Amezcua-Allieri M.A., Shevnin V., Rosas-Molina A., Marín-Córdova S., 2014, Joint interpretation of geoelectrical and volatile organic compounds data: a case study in a hydrocarbons contaminated urban site. *Geofísica Internacional*, 53, 183-198.

Dena O.S., Griselda Obeso C., Doser D., Leyva J.E., Rascon E., Gómez, F., Domínguez M.A., 2012, Using subsurface geophysical methods in flood control: A resistivity survey to define underground storage capacity of a sand body in Ciudad Juárez, Mexico. *Geofísica Internacional*, 51, 3, 225-249.

Farquhar G.J., 1989, Leachate: production and characterization. Canadian J. Civ. Engin., 16, 317 – 325.

Gastal M.C., Ferreira F.J.F., 2013, Discussão dos processos de construção do complexo granítico São Sepé, RS: feições geológicas e petrográficas. *Pesquisas em Geociências*, 40, 3, 233-257.

Georgaki I., Soupios P., Sakkas N., Ververidis F., Trantas E., Vallianatos F., Manios T., 2008, Evaluating the use of electrical resistivity imaging technique for improving CH_4 and CO_2 emission rate estimations in landfills. *Sci. Total Environ.*, 389, 522-531.

Geotomo Software, 2013, Rapid 2-D Resistivity & IP inversion using the least-squares method – Instruction Manual. Geotomo, Gelugor, 173 pp.

Hernández-Soriano M.C., 2014, Environmental risk assessment of soil contamination. InTech, New York, 905 pp.

IPEA – Instituto de Pesquisas Econômicas Aplicadas, 2012, Diagnóstico dos Resíduos Sólidos Urbanos. Governo Federal, Brasília, 82 pp.

IBGE 2010, Instituto Brasileiro de Geografia e Estatística. e-cidades. www.ibge.gov.br. Acesso em 02/08/2016

IRIS Instruments, 2006, Syscal Pro-User´s Manual. Standard & Switch (48 - 72 - 96 - 120) Version. IRIS, Orléans, 87 pp.

Kjeldsen P., Barlaz M.A., Rooker A.P., Baun A., Ledin A., Christensen T.H., 2002, Present and long-term composition of MSW landfill leachate: a review. Critical Reviews in Environ. Sci. Technol., 297-336.

Knödel K., Lange G., Voigt H.J., 2007, Environmental Geology: Handbook of fields methods and case studies. Springer, Hannover, 1357 pp.

Lehr J., Hyman M., Gass T.S., Servers W.J., 2001, Handbook of complex environmental remediation problems. McGraw-Hill Handbooks, New York, 606 pp.

Lema J., Mendez R., Blazquez R., 1988, Characteristics of landfill leachates and alternatives for their treatment: a review. *Water, Air, and Soil Pollution*, 40, 223-250.

Loke M.H., Baker R.D., 1996, Rapid least-squares inversion of apparent resistivity pseudosections by quasi-Newton method. *Geophys. Prospect.*, 44, 131-152.

Matos I.C., Mexias A.S., Formoso M.L.L., 2004, Alteração hidrotermal a SW do Complexo Granítico São Sepé – São Sepé/RS. *Geochim. Brasil.*, 18,1, 12-27.

Meju M.A., 2000, Geoelectrical investigation of old/abandoned, covered landfill sites in urban areas: model development with a genetic diagnosis approach. *J. App. Geophys.*, 44, 115–150.

Milsom J.J., Eriksen A., 2011, Field Geophysics. John Wiley & Sons Ltd, Chichester, 297pp.

Moreira C.A., Braga A.C.O., Godoy L.H., Sardinha D.S., 2013, Relationship between age of waste and natural electric potential generation in Sanitary Landfill. *Geofísica Internacional*, 52, 4, 375-383.

Moreira C.A., Munhoz T., Cavallari F., Helene L.P.I., 2015, Electrical resisitivity to detect zones of biogas accumulation in a landfill. *Geofísica Internacional*, 54, 4, 353-362.

Moreira C.A., Lapola M.M., Carrara A., 2016, Comparative analyzes among electrical resistivity tomography arrays in the characterization of flow structure in free aquifer. *Geofísica Internacional*, 55, 2, 119-129.

Ochoa-González G.H., Carreón-Freyre D., Cerca M., López-Martínez M., 2015, Assessment of groundwater flow in volcanic faulted areas. A study case in Queretaro, Mexico. *Geofísica Internacional*, 54, 3, 199-220.

Reddy P.J., 2011, Municipal Solid Waste Management: Processing, Energy Recovery, Global Examples. CRC Press, Boca Raton, 470 pp.

Remus, M.V.D.; Mcnaughton, N.J.; Hartmann, L.A.; Fletcher, I.R., 1997, U-Pb SHRIMP Zircon Dating and Nd Isotope Data of Granitoids of the São Gabriel Block, Southern Brazil:

evidence for an Archaean/Paleoproterozoic basement. In: International Symposium on Granites and Associated Mineralizations, 2, Salvador: CBPM/SGM, p.271-272.

Rubin Y., Hubbard S.S, 2005, Hydrogeophysics. Springer, Dordrecht, 527 pp.

Sara M., 2003, Site assessment and remediation handbook. 2°ed., Lewis Publishers, Florida, 1161 pp.

Sartori P.L., Rüegg N.R., 1979, O complexo Granítico de São Sepé, Rio Grande do Sul e a evolução das rochas graníticas da região orogênica do Sudeste. *Boletim IG – USP*, 10, 69-78.

Shevnin V., Delgado-Rodríguez O., Fernández-Linares L., Zegarra-Martinez H., Mousatov A., Ryjov A.A. 2005. Geoelectrical characterization of an oil contaminated site in Tabasco, Mexico. *Geofísica Internacional*, 44, 3, 251-263.

SNIS - Sistema Nacional de Informações sobre Saneamento. 2013. Diagnóstico dos Serviços de Água e Esgotos. Ministério das Cidades, Brasilia. 432 pp.

Tchobanoglous G., Theisen, H. Vigil S., 1993, Integrated solid waste management: Engineering principles and management issues. McGraw–Hill, New York, 978 pp.

Tchobanoglous G., Kreith F., 2002, Handbook of solid waste management. McGraw-Hill, New York, 834 pp.

Telford W.M., Geldart L.P., Sheriff R.E., 1990, Applied Geophysics. 2° ed., Cambridge University Press, Cambridge, 770 pp.

Twardowska I., Allen H.E., Häggblom M.H., Stefaniak S., 2006, Soil and water pollution: monitoring, protection and remediation. Nato Science Series, Springer, Krakom, 662 pp.

Vesilind P.A., Worrell W., Reinhart, D., 2002, Solid waste engineering. Brooks/Cole, Pacific Grove, 1052 pp.

Vieira L.B., Moreira C.A., Côrtes A.R.P., Luvizotto G.L., 2016, Geophysical modeling of the manganese deposit for Induced Polarization method in Itapira (Brazil). *Geofísica Internacional*, 55, 2, 107-117.

Yung-Tse H., Wang L.K., Shammas N.K., 2014, Handbook of environment and waste management: land and groundwater pollution control – volume 2. World Scientific, Toh Tuck Link, 1114 pp.

Geofísica Internacional (2017) 56-4: 359-375

Original paper

Effects of the soil properties on the sea pressure profile due to seismic motions

Alejandro Rodríguez-Castellanos*, Rafael Ávila-Carrera, Ernesto Pineda-León, Víctor Martínez-Calzada and Francisco José Sánchez-Sesma

Received: October 27, 2016; accepted: August 25, 2017; published on line: October 01, 2017

Resumen

Un gran número de sismos tienen epicentros en áreas fuera de la costa y sus efectos son preocupantes. Este artículo aplica, para problemas bidimensionales, el Método Indirecto de Elementos Frontera para calcular el perfil de presiones sísmicas, en toda la profundidad del agua, debida a la incidencia de ondas P y SV sobre un fondo marino, el cual se caracteriza por su relación de Poisson. Se hace énfasis también en las amplificaciones del fondo marino. Nuestra formulación puede ser considerada como una implementación numérica del Principio de Huygens, en el cual las ondas difractadas son construidas desde las fronteras desde las cuales son radiadas. Esto es equivalente al teorema de representación de Somigliana. Los resultados numéricos muestran la importancia de las propiedades del suelo marino debido a que el perfil de presiones muestra mucha dependencia respecto a ellas. En algunos casos, las amplificaciones de las presiones son seis veces entre valores extremos del suelo. Se incluyen también, resultados de modelos con estratos y se evidencia que las amplificaciones sísmicas que pueden alcanzarse se encuentran entre 15.57 y 18.36 veces la onda incidente P y SV, respectivamente.

Palabras clave: Método Indirecto de Elementos Frontera, ondas elásticas, fondo marino, sismo marino, perfil de presiones sísmicas, relación de Poisson.

Abstract

Large number of earthquakes have epicenters in offshore areas and their effects are a matter of great concern. This paper applies, for two dimensional problems, the Indirect Boundary Element Method to calculate the seismic pressure profile with the water depth due to the incidence of P- and SV-waves on the seabed, which can be characterized using the soil properties. Moreover, seismic amplifications of the seabed are highlighted. Our formulation can be considered as a numerical implementation of the Huygens' Principle in which the diffracted waves are constructed at the boundary from which they are radiated. Thus mathematically, it is fully equivalent to the classical Somigliana's representation theorem. Numerical results show the importance of knowing the properties of the marine soil because the pressure profile has an enormous dependence with respect to them. In some cases, pressure amplifications of six times between extreme values of soil materials can be expected. In addition, results from a layered numerical model evince that large seismic amplifications may be found, they can reach values up to 15.57 and 18.36 times the incident P- and SV-waves, respectively.

Keywords: Indirect Boundary Element Method; elastic waves; seabed; seaquake, seismic pressure profile; Poisson's ratio.

A. Rodríguez-Castellanos*
R. Ávila-Carrera
Instituto Mexicano del Petróleo
Eje Central Lázaro Cárdenas 152
Gustavo A. Madero, 07730
México CDMX, México
*Corresponding author: arcastel@imp.mx

A. Rodríguez-Castellanos*
V. Martínez-Calzada
Escuela Superior de Mecánica y Eléctrica
Instituto Politécnico Nacional
Unidad Profesional Adolfo López Mateos s/n
México CDMX, México

E. Pineda-León
Escuela Superior de Ingeniería y Arquitectura
Instituto Politécnico Nacional
Unidad Profesional Adolfo López Mateos s/n
México CDMX, México

F. José Sánchez-Sesma
Instituto de Ingeniería
Universidad Nacional Autónoma de México
Ciudad Universitaria
Delegación Coyoacán, 04510
México CDMX, México

Introduction

A large number of earthquakes have epicenters in offshore areas (Mangano *et al,.* 2011). Seaquakes are characterized by the propagation of vertical earthquake motion on the sea bottom as a compressional wave and cause damage to ships, and their effect on floating structures is a matter of great concern (Takamura *et al*., 2003). When the seabed is vibrating due to a seaquake, the compressional waves propagate with the water depth due to compressibility of water.

An analytical approach that can predict the dynamic response of a flexible circular floating island subjected to seaquakes was studied by Tanaka *et al.* (1991). The floating island was modeled as an elastic circular plate, and the anchor system to be composed of tension-legs. Linear potential flow theory applied to flexible floating island subjected to wind-waves and seaquakes was presented in Hamamoto *et al.* (1991), where the hydrodynamic pressure generated on the bottom surface of the island was obtained in closed form. The nonlinear transient response of floating platforms to seaquake-induced excitation was studied by Arockiasamy *et al.* (1983), where cavitation effects were considered.

A special boundary method for earthquake-induced hydrodynamic pressures on rigid axisymmetric offshore structures, including both the water compressibility and seabed flexibility, was presented by Avilés and Li (2001). A boundary integral equation was derived assuming that the seabed is a semi-infinite homogeneous elastic solid in order to analyze the seaquake-induced hydrodynamic pressure acting on the floating structure (Takamura *et al.,* 2003). Boundary integral equations have been also used to calculate the hydrodynamic pressure caused by seaquake in layered media (Higo, 1997), and for three dimensional cases in Jang and Higo (2004). Recently, the boundary element method and the discrete wave number method have been used to determine pressures near the interface of fluid-solid models (Flores-Mendez *et al.,* 2012, Rodríguez-Castellanos *et al.,* 2011, 2014).

The Boundary Element Method (BEM) has been applied extensively to solve problems related to fluid-solid media subjected to seismic excitations. For instance, Schanz (2001) applied the BEM to study the dynamic responses of fluid-saturated semi-infinite porous continua subjected to transient excitations such as seismic waves. Moreover, irregular fluid-solid interfaces of oceanic regions or gulf areas under seismic wave propagation were analyzed in Qian and Yamanaka (2012), here important simulations of the water reverberation in the sea due to an explosive source were dealt, which show the applicability of the BEM to marine ambient. The dynamic response of a concrete gravity dam subject to ground motion and interacting with the water, foundation and bottom sediment was studied using the Boundary Element (Dominguez and Gallego, 1996). The model is able to represent continuous media with water, viscoelastic and fluid-filled pore-elastic zones. On the other hand, the dynamic response of liquid storage tank, including the hydrodynamic interactions, subjected to earthquake excitations was studied by the combinations of the boundary element and finite element methods (Hwang and Ting, 1989). Another application of BEM is focused on the seismic response of fluid-filled boreholes. In this way, in Tadeu *et al*. (2001), the BEM is used to evaluate the three-dimensional wave field caused by monopole sources in the vicinity of fluid-filled boreholes.

It is well known that Poisson´s ratio and Young´s modulus are sufficient parameters to linearly describe the stress-strain response under hysteretic conditions. In this work, a study of the sea water pressure profiles due to seismic actions of P- and SV-waves is presented. In fact, the ratio of P- to SV-wave velocities is a function of the Poisson´s ratio, only. Bowles (1988) and Wade (1996) classify the soils using its Poisson´s ratio. While, Sánchez-Sesma and Campillo (1991), Rodríguez-Castellanos *et al.* (2005) and recently Alielahi *et al.* (2015) used this criterion to characterize the soil where the wave propagation takes place. Hence, this criterion was followed as well.

This paper applies, for 2D problems in plane strain conditions, the Indirect Boundary Element Method to calculate the seismic pressure profile with the water depth due to the incidence of P- and SV- waves on the seabed (Figure 1), which is characterized by its soil properties. Wave amplifications are also highlighted. The formulation can be considered as a numerical implementation of the Huygens' Principle in which the diffracted waves are constructed at the boundary from which they are radiated. Thus, mathematically, it is fully equivalent to the classical Somigliana's representation theorem. The results are compared with those previously published. In the following paragraphs a brief explanation of the BEM applied to sea bottom subjected to seismic motions is given.

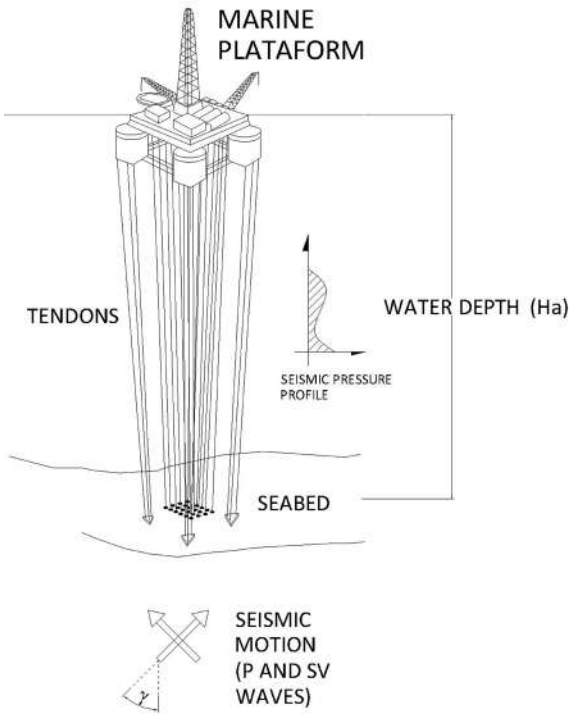

Figure 1. Marine facilities under the incidence of seismic movements.

Formulation of the method

Consider the movement of an elastic solid, homogeneous and isotropic, of volume delimited by its boundary (Figure 2), subjected to body forces $b_i(\xi, t)$ and null initial conditions. Introducing fictitious force densities $\phi_i(\xi, t)$ in Γ, the fields of displacements and tractions could be written as Banerjee and Butterfield (1981):

$$u_j(x,t) = \int_\Gamma G_{ij}(x,\xi,t) * \phi_i(\xi,t) d\Gamma_\xi + \int_\Omega G_{ij}(x,\xi,t) * b_i(\xi,t) d\Omega_\xi + u_j^o(x,t)$$
$$t_j(x,t) = \int_\Gamma T_{ij}(x,\xi,t) * \phi_i(\xi,t) d\Gamma_\xi + \int_\Omega T_{ij}(x,\xi,t) * b_i(\xi,t) d\Omega_\xi + t_j^o(x,t) \quad (1)$$

where $u_j^o(x, t)$ and $t_j^o(x, t)$ are free terms depending of the elastic wave that impinges on the body, for this research the incident P- and SV-waves propagating at some angle in a homogeneous half-space are considered. The symbol $(*)$ indicates the convolution integral in time domain, $\xi=\{x, z\}$ and $x=\{x, z\}$. $G_{ij}=\{x, \xi, t\}$ and $T_{ij}=\{x, \xi, t\}$ are Green functions for displacements and tractions, respectively. These functions are available in Rodríguez-Castellanos *et al*. (2005).

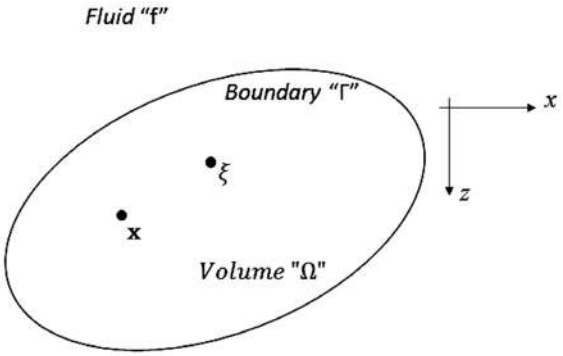

Figure 2. Elastic solid, homogeneous and isotropic, of volume Ω delimited by its boundary Γ.

For Eqs. (1), it is acceptable that these boundary integrals are valid for the main value of Cauchy. Then, if point x is allowed to approach to the boundary from inside of the region, at that time, Eqs. (1) are transformed to the next boundary equations:

$$u_j(x,t) = \int_\Gamma G_{ij}(x,\xi,t) * \phi_i(\xi,t) d\Gamma_\xi + \int_\Omega G_{ij}(x,\xi,t) * b_i(\xi,t) d\Omega_\xi + u_j^o(x,t)$$
$$t_j(x,t) = \frac{1}{2}\phi_j(x,t)\delta_{ij} + \int_\Gamma T_{ij}(x,\xi,t) * \phi_i(\xi,t) d\Gamma_\xi + \int_\Omega T_{ij}(x,\xi,t) * b_i(\xi,t) d\Omega_\xi + t_j^o(x,t) \quad (2)$$

were δ_{ij} is Kronecker´s delta.

The problem was changed to the frequency domain, accepting that the incident waves have harmonic dependency with time, of type $e^{i\omega t}$ (i.e. $u_j(x, t)= u_j(x, \omega)e^{i\omega t}$), where ω is the circular frequency and "i" is the imaginary unit. The displacements and tractions can be expressed as follow:

$$u_j(x,\omega) = \int_\Gamma G_{ij}(x,\xi,\omega)\phi_i(\xi,\omega) d\Gamma_\xi + \int_\Omega G_{ij}(x,\xi,\omega) b_i(\xi,\omega) d\Omega_\xi + u_j^o(x,\omega)$$
$$t_j(x,\omega) = \frac{1}{2}\phi_j(x,\omega)\delta_{ij} + \int_\Gamma T_{ij}(x,\xi,\omega)\phi_i(\xi,\omega) d\Gamma_\xi + \int_\Omega T_{ij}(x,\xi,\omega) b_i(\xi,\omega) d\Omega_\xi + t_j^o(x,\omega) \quad (3)$$

If the body is a fluid of volume Ω_w delimited by its boundary Γ_w then the next functions represent the displacement and pressure fields:

$$u_n^f(x,\omega) = \frac{1}{2}\psi(x,\omega) + \frac{1}{\rho\omega^2}\int_{\Gamma_W} \frac{\partial G^f(x,\xi,\omega)}{\partial n} \psi(\xi,\omega)d\Gamma_{W\xi} + \frac{1}{\rho\omega^2}\int_{\Omega_W} \frac{\partial G^f(x,\xi,\omega)}{\partial n} b^f(\xi,\omega)d\Omega_{W\xi}$$

$$pf(x,\omega) = \int_{\Gamma_W} G^f(x,\xi,\omega)\psi(\xi,\omega)d\Gamma_{W\xi} + \int_{\Omega_W} G^f(x,\xi,\omega)b^f(\xi,\omega)d\Omega_{W\xi}, \quad (4)$$

where $\psi(x, \omega)$ is the force density of fluid, ρ is the fluid density, $G^f(x, \xi, \omega)$ is the Green function for fluid pressure and is given by $Gf(x, \xi, \omega)=(\rho\omega^2)/4i\, H_0^{(2)}(\omega r/c^f)$, $H_0^{(2)}$ is the Hankel´s function of second kind and zero order, r is the distance between x and ξ, and c^f is the velocity in the fluid. The super index f denotes the fluid.

The boundary conditions of the problem, according to Figure 1, are:

On the free water surface, the pressure is null, it means:

$$p^f(x,\omega) = 0. \quad (5)$$

Onthe seabed:

Continuity of normal displacement:

$$u_i(x,\omega)n_i = u_n^f(x,\omega). \quad (6)$$

Null shear in solid-water interface:

$$(\delta_{ij} - n_i n_j)t_j(x,\omega) = 0. \quad (7)$$

The tractions on the solid are balanced with water´s pressures

$$t_i(x,\omega)n_i = -p^f(x,\omega), \quad (8)$$

where n_i is the unit normal vector associated to direction "i", $u_n^f(x, \omega)$ is the normal displacement with respect to surface of interface and $u^f(x, \omega)$ is the water pressure.

If the boundary conditions, Eqs. (5)-(8) are expressed, using the integral representations, Eqs. (3) and (4), neglecting the body forces, and if the boundaries (Γ and Γ_w) are discretized in Nel boundary elements, then the following system, known as Fredholm´s system of integral equations of second kind and zero order is found.

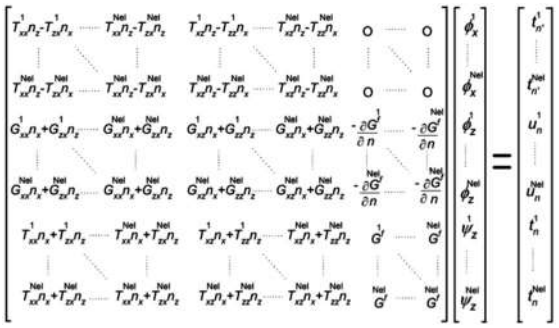

Once the solution of equation (9) is obtained, the displacement and pressure fields of equations (3) and (4), respectively, can be calculated. Additional details on the treatment to obtain the system of integral equations (9) can be consulted in Rodríguez-Castellanos *et al*. (2014).

Verification of the method and numerical examples

Verification

Wong (1982) and Kawase (1988) reported the seismic amplifications for the case of a topography with semicircular canyon shape of radius "a" (Figure 3d). They considered an elastic solid medium (with the properties shown in Table 1) in contact with an acoustic (vacuum) medium showing seismic amplifications in the solid surface between $-2 \le \frac{x}{a} \le 2$, for a frequency of $n = \frac{\omega a}{\pi\beta} = 2$. The incidence of seismic waves are P- and SV- waves with incident angles γ=0º and γ=30º, for each one.

In the present formulation, it is possible to consider that the high of the acoustic medium is approaching to infinity ($H_a \longrightarrow \infty$) (and such properties are from the air (Table 1). H_a is the water depth. Moreover, this method can deal with a solid-vacuum interface; the same problem studied by Wong (1982) and Kawase (1988) will be exactly resolved in the present study. The obtained results for the acoustic (air or vacuum) medium in contact with a solid one are displayed in Figures 3 and 4. The receivers are located on the seabed. Circles represent results by Wong and squares by Kawase. The present results are plotted with lines. In general, it is possible to appreciate a good match between the results found with the current formulation and those from the mentioned references, for both displacements and P- and SV-wave incidences.

Table 1. Elastic properties for elastic and acoustic media.

	$\alpha\left(\frac{m}{s}\right)$	$\beta\left(\frac{m}{s}\right)$	$\rho\left(\frac{m}{m^3}\right)$	Observations
Air Bedford and Drumheller (1994)	330	------	1.29	only for Verification
Elastic medium Wong (1982) and Kawase (1988)	1998	1000	2500	only for Verification

The use of the Green's functions for infinite spaces, expressed in terms of Hankel's functions of second kind, is an advantage of our integral formulation. Green's functions for a half space can be also used in problems where a free surface is present. However, these functions are more complex than those for the infinite space and do not represent substantial save in computational requirements. On the other hand, we only modeled a finite part of the water and interface. Such truncation induces artificial perturbations caused by diffractions at the edges of the numerical model. However, these perturbations are characterized by small amplitudes and their reflections inside the model are negligible. The simplest solution is to choose a surface length large enough that the fictitious perturbations fall outside the observational space-time window. Then, edge effects due to the finite size of the discretized boundaries can be neglected; therefore, absorbing boundaries are not required.

The use of dimensionless frequencies has been usually employed to express the displacement fields of soil structures under seismic motions. In this context, several authors have used dimensionless frequencies to calculate strong ground motions or surface motions due to seismic movements. For instance, Trifunac (1973) (η=0.0 to 3.0), Wong (1982) (η=0.5,1.0,1.5,2.0), Sánchez-Sesma and Campillo (1991) (η=0.0 to 4.0), Rodríguez-Castellanos *et al.* (2005) (η=0.0 to

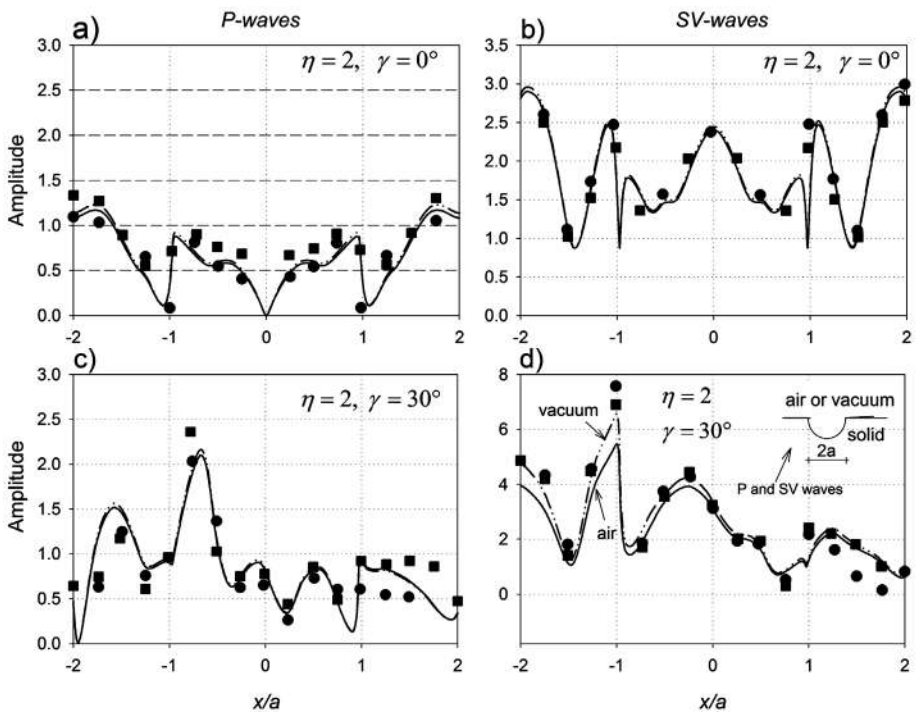

Figure 3. Comparison of results obtained by Wong (1982) (circles), Kawase (1988) (squares) and current formulation by BEM (lines). Solid line shows displacements in the x-direction for an air acoustic medium, while dash-dot-dot line shows displacements for a vacuum one.

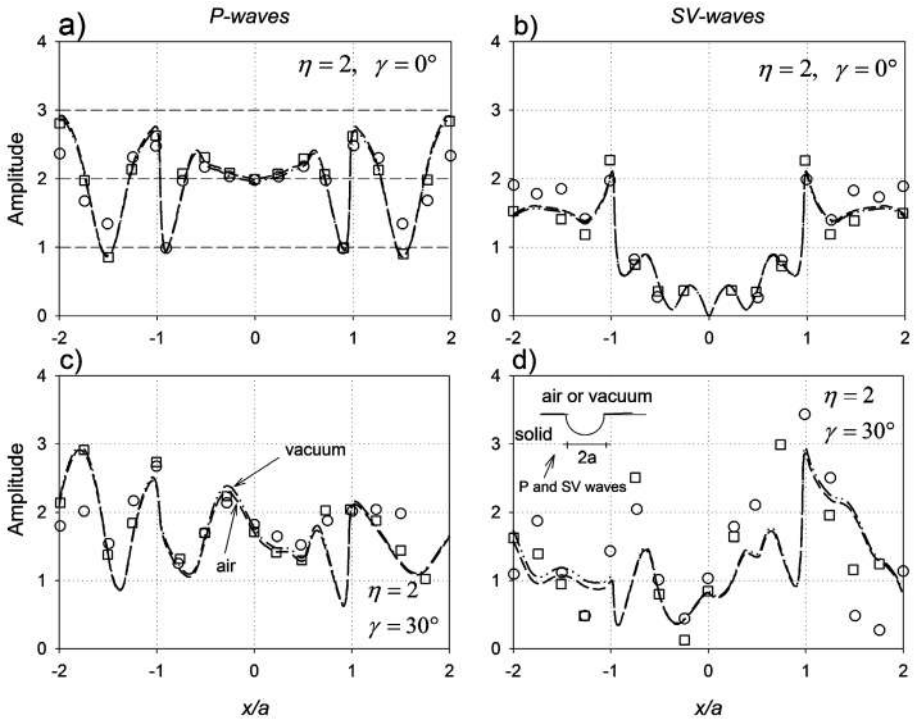

Figure 4. Comparison of results obtained by Wong (1982) (circles), Kawase (1988) (squares) and current formulation by BEM (lines). The striped line represents displacements in *z*-direction for an air acoustic medium, while dash-dot-dot line shows displacements for a vacuum one.

3.0) and recently Alielahi *et al.* (2015) (η=0.5, 1.0) used this criterion. In this work, results using η=0.0 to 4.0 are presented, this interval can be considered within the range of interest in earthquake engineering and seismology.

Numerical Examples

In order to develop numerical examples and show the influence that soil properties have on the propagation of compressional and shear waves that affect the sea bottom, and subsequently in pressure states with the water depth, the following elastic parameters were used for the analyses (see Table 2).

The pressure profiles show many different behaviors that depend mainly on the soil properties and the type of incident wave. For example, in Material 1, a lower amplification of pressures due to P-wave incidence is obtained, compared with the amplification obtained for Material 5 (see Figure 5). In Figure 5, the pressure profiles for the non-dimensional frequency of $n = \dfrac{\omega a}{\pi\beta} = 2$ and Materials 1 to 5. In Figure 5a, the pressure obtained for Material 5 is 10 times higher than the one obtained for Material 1. This effect decreases as the incident angle of P- wave increases (i.e. γ=60º). For all cases presented in this figure, the condition of zero pressure in the water surface is satisfied. In general, the incident SV-waves produces less pressure than that obtained for P-waves. In Figure 5b, it is verified that SV-wave with normal incident (γ=0º) does not generate any pressures state, for any material. Figure 5f indicates that a marine soil of Material 1 produces an oscillatory behavior with water depth. In most of the studied cases, the maximum pressure obtained is near the seabed; this is important to be considered for the design of facilities attached on the seabed.

For Material 1, the underlying solid pressure variation with the water depth shows relatively small values for P-wave incidences with the three selected angles (0, 30 and 60 degrees) because of the impedance contrast between solid and fluid. On the other hand, for incoming SV-waves and large incidence angle (60 degrees) the horizontal phase velocity is quite large, as compared with the propagation velocity within the fluid. This and the polarization of motion induce significant emission of waves within the solid for a quasi- vertical direction.

Table 2. Parameters used for analyses

Elastic medium	SV-wave velocity (β) (m/sec)	Density (ρ) (kg/m^3)	Poisson's ratio (υ)	Reference
1	3000	2100	0.25	
2	400	1700	0.35	Huerta-Lopez *et al*.
3	190	1400	0.40	2003 and 2005
4	90	1300	0.45	
5	20	1320	0.495	Roever *et al*., 1959

Figure 6 depicts the behavior of pressures when P- and SV-waves impact a sinusoidal bathymetry (see detail in Figure 6f). The material properties and incident angles of the elastic waves are the same as in Figure 5. For the case of P-waves, the pressure field shows small variations in comparison with a flat interface. However, for the case of SV-waves, diffracted pressure waves are present for an incident angle γ=0º. For angles of γ=30º and γ=60º the pressures describe patterns similar to those for a flat interface (Figure 5), but they reach lower values.

Figure 7 shows the pressure fields obtained at several water depths. These pressures were calculated at six locations (H/H_a=0, -0.20, -0.40, -0.60, -0.80 and -1.0) for a frequency range of $0<\eta<4.0$. The soil has the properties of Material 1, according to Table 2. In this case, normal (γ=0°) and oblique (γ=30°) P- and SV-wave incidences on a flat interface (Figure 7a) are considered. It must be emphasized that for all the cases null pressures are obtained on the water surface (Figures 7b-e), as expected. On the other hand, null pressures are obtained, when an SV-wave impacts with an angle γ=30°

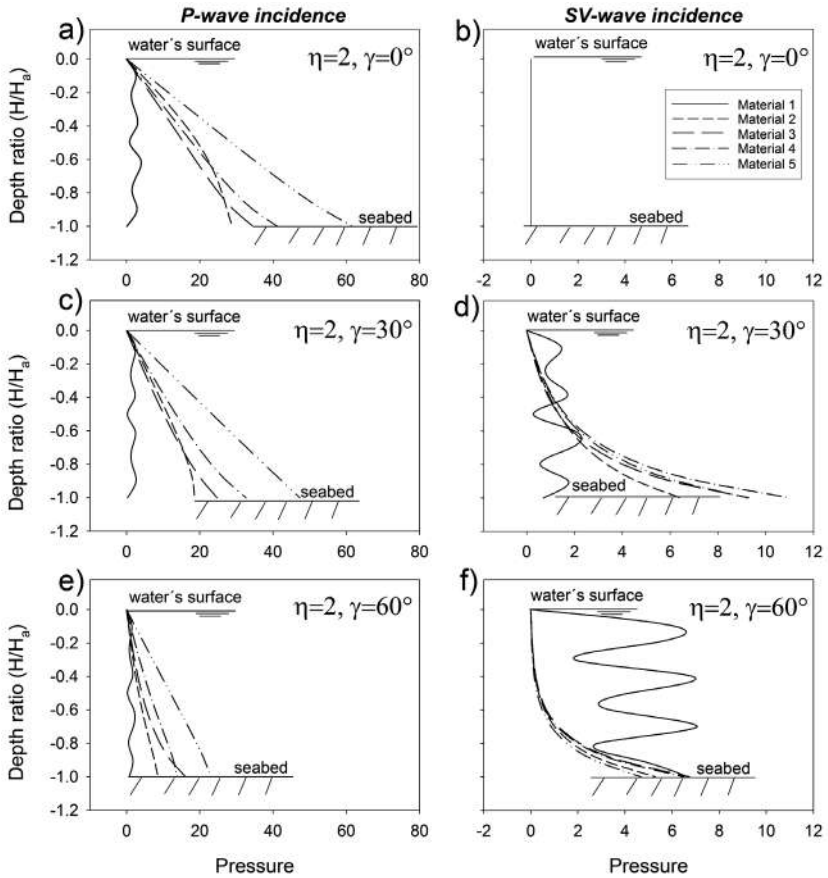

Figure 5. Pressure spectrum for different soil properties of seabed and incident angle of P- and SV-waves, for a flat bathymetry.

(Figures 7c, g, k, o, s, and w). It can also be said that several peaks are present in the graphs, which are associated with the resonances generated by waves interacting between the water surface and the seafloor. These peaks appear clearly in the case of normal P-wave incidence and near to the seafloor (H/H_a = -1.0, Figure 7v). In addition, it is noticeable that the oblique P- and SV-wave incidences (γ= 30°) generate pressure fields at the six mentioned locations. However, these pressures show less amplitude than those generated by a normal P-wave incidence. In general terms, the greatest pressures are present in the proximity of the seafloor (Figures 7v, x and z), which have been also highlighted in the previous analyzes.

Figure 8 displays the propagation of P-waves calculated in 51 receivers spaced 0.04 H/H_a. The propagation is presented for five types of seabed, according to Table 2, for Materials 1 to 5. The first 25 receivers are located in the solid, see bottom figures showing displacements in the z-direction. Displacements for the x-direction are zero when a normal P-wave impacts the interface. The last 26 receivers are located in the water, see top figures showing the pressure generated by the incidence of P-waves. A normal incidence (γ=0°) of P-waves that impinges on a flat and horizontal surface does not create diffraction in the x-direction. In general terms, an incident wave that is propagating in the solid is transmitted to the fluid generating a pressure field. It can also be seen that the water surface causes the reflection of waves that propagate in the opposite direction. Later, in Figure 10 pressures obtained nearby seabed are discussed.

In Figure 8, the displacements for 64 frequencies up to 15.39 Hz at the mentioned receivers were computed in the frequency domain. In order to simulate the motion with the time we used the FFT algorithm to calculate synthetic seismograms using a Ricker wavelet. This pulse has a temporal dependence given by:

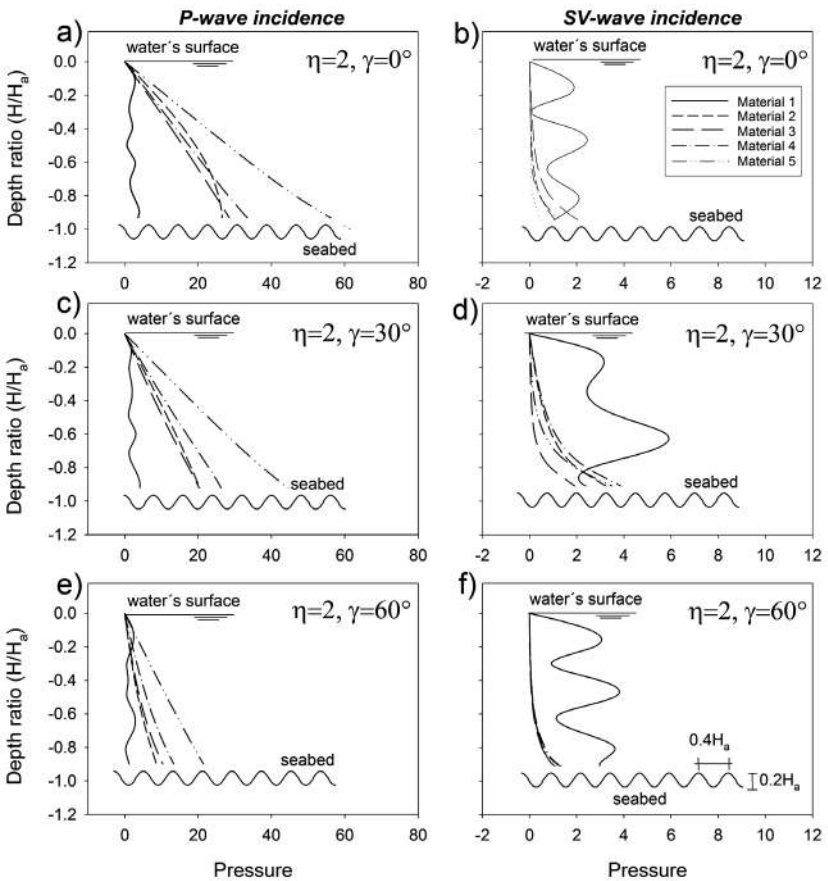

Figure 6. Pressure spectrum for different soil properties of seabed and incident angle of P- and SV-waves, for a sinusoidal bathymetry.

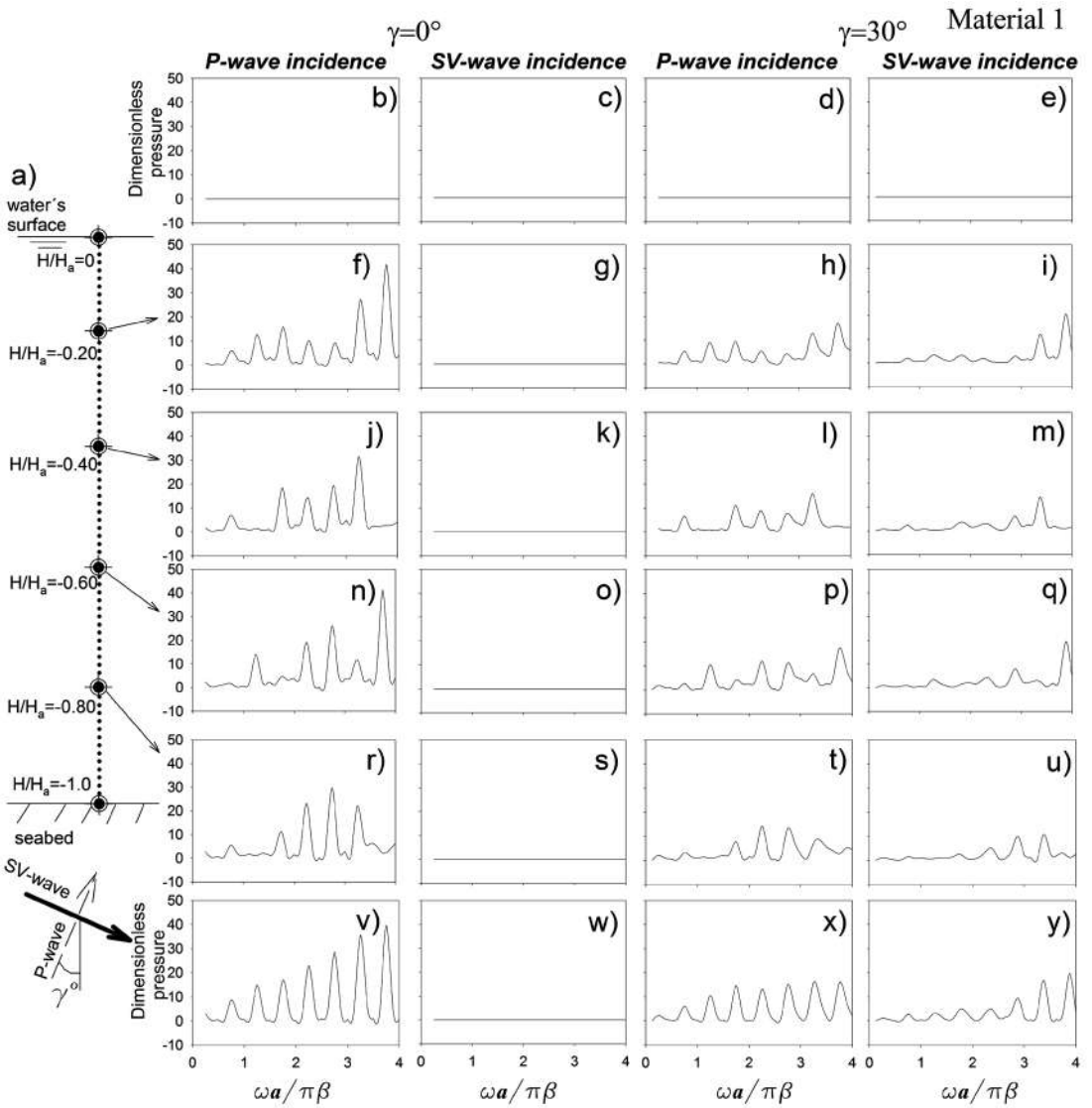

Figure 7. Pressure spectrum at several water depths. The range of dimensionless frequency is $0<\eta<4.0$.

$$R(t) = a(t) - \frac{1}{2} e^{-a(t)}, \qquad (14)$$

where

$$a(t) = \frac{(t - t_S)}{t_p}^2, \qquad (15)$$

t_p = characteristic period, and t_s = time-lag or offset. In the present computations t_p = 0.259 sec and t_s = 0.779 sec were used. The time scale is given by $\beta t/H_a$ (normalized time).

Physically, η represents the ratio of the water depth (H_a) to the incident wavelength. The range of frequency (64 frequencies up to 15.39 Hz) permits to generate a Ricker pulse with a wavelength that can "feel" the interface and the water surface. According to this, Figure 8 makes clear that several wave diffractions and reflections take place in the water, for the selected wavelength.

In Figure 8, the incidence of elastic waves on the interface produces the phenomenon of reflection and refraction of waves and also the appearance of interface waves (Scholte

waves). This last type of wave appears once the interface is excited. The energy that carries this wave dissipates during its travel, radiating energy towards the fluid and the solid medium. In Figures 8a-j, the interface waves continue to radiate energy and generate variations in pressure after the first reflections and refractions have taken place. These pressure variations can be seen from 1.7 to 2 seconds for the case of Figure 8a, from 1.5 to 1.7 seconds in Figure 8b, from 1.3 to 1.8 seconds in Figure 8c and from 1 to 1.5 seconds in Figure 8d. In all these cases, the influence of the Poisson ratio on the pressure state in the fluid can be observed. A detailed study of the interface waves and their effect on pressure can be found in Borejko (2006).

The incidence of P- and SV-waves on the seabed could cause displacements in x and z-directions. The calculated amplitudes are dependent on the type of the seabed material and the incident angle of the seismic movements. Figure 9 shows the displacements produced in the seabed at frequency η=2 for incident P- and SV-waves at angles=0º, 30° and 60°. Materials 1 to 5 were analyzed. In general terms, the normal incidence of P-waves causes amplitudes of vertical displacement (z) close to 3 (Figure 9c). For other angles of incidence the displacement is lower. The normal incidence of SV-waves gives zero displacements in the vertical direction (Figure 9d), while for other angles of incidence such displacements are small compared to those caused by P-waves. The maximum displacement in the x-direction is produced by the normal incidence of SV-waves, these displacements decrease as the incidence angle increases. The diffraction caused by P-waves is very small for the incidences and 30°, whereas for γ=60º it reaches a value near to 2 for Material 1.

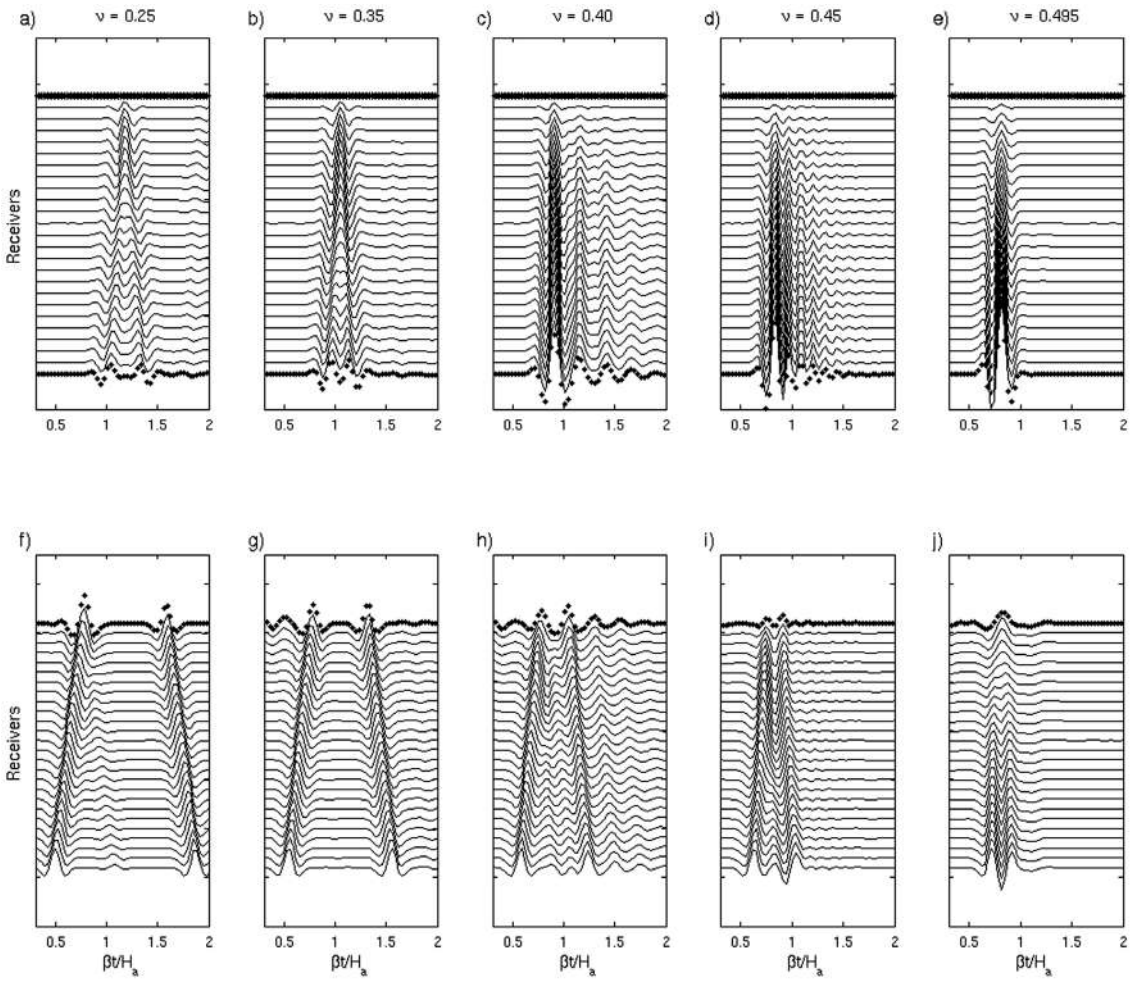

Figure 8. Propagation of compressional waves recorded at 51 receivers for different materials: water pressure (top figures) and displacement in z-direction in the solid (bottom figures).

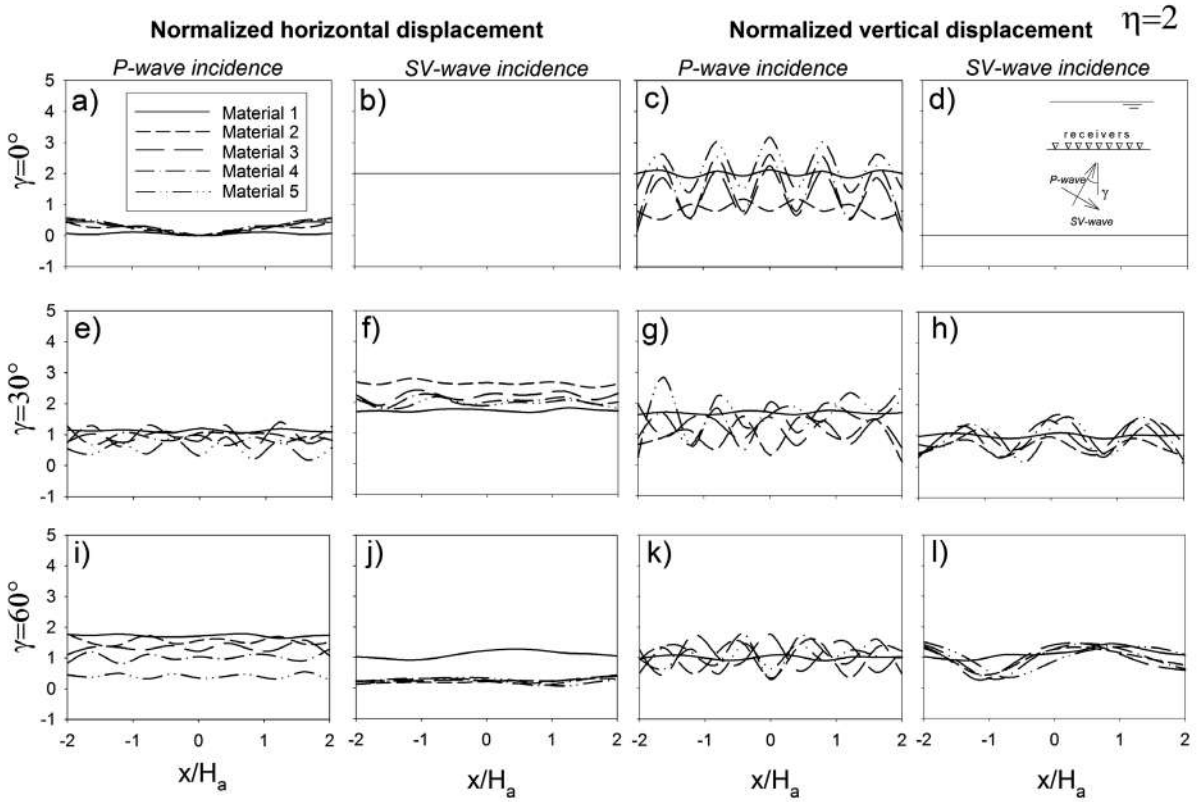

Figure 9. Displacement amplitudes calculated on seabed resulting from incidence of P- and SV-waves with angles of γ=0°, 30° and 60°.

Figure 10 presents the pressures in time domain, obtained in the vicinity of the seabed for Materials 1 to 5 and for normal incidence of P-waves. It is clear that for Material 5 strong amplifications in the range of 6.05 times are obtained in comparison with Material 1 (see Figure 10e). This result shows the importance of adequately characterizing the type of soil where marine structures will be located since strong amplifications of seaquakes can be present.

Now, results for a layered medium are displayed. This medium is composed of an elastic half space (Material 1), a layer (Material 2) and the sea water. The elastic properties of the solid medium can be found in Table 2. The studied model is detailed on Figure 11e, where the localization of receivers 1 and 2 are also shown. Receiver 1 is located on the seafloor and receiver 2 is between the two solid materials. We studied two layer thicknesses, one of h/H_a=0.025 (Figures 11c and d) and another of h/H_a=0.05 (Figures 11a and b). These figures show the calculated seismic amplifications in such receivers for a frequency range $0<\eta<4.0$. For this purpose, the normal incidence (γ=0°) of P- and SV-waves on the stratified medium (Figure 11e) is considered. In this figure, it is remarkable that the greatest seismic amplifications are obtained at Receiver 1, reaching a value of 15.57 for the incidence of P-waves (Figure 11a) and 18.36 (Figure 11b) for SV-waves. These values correspond to the case of a layer thickness of h/H_a=0.05. In fact, in this case, the layer with greater thickness generates larger seismic amplifications with respect to the layer of reduced thickness. In the case of h/H_a=0.025, the maximum amplifications obtained correspond to 11.08 (Figure 11c) for the incidence of P-waves and 16.25 (Figure 11d) for SV-waves. In addition, the presence of the layer causes more oscillations in the response associated with the P- waves, in comparison to the SV-waves. Such interactions generate sharp peaks in the response obtained. It should be noted that in all cases, the displacements calculated for the receiver 2 had an average value of 2. Strong amplifications by soft layer have been previously reported in the field of earthquake engineering and seismology. For example,

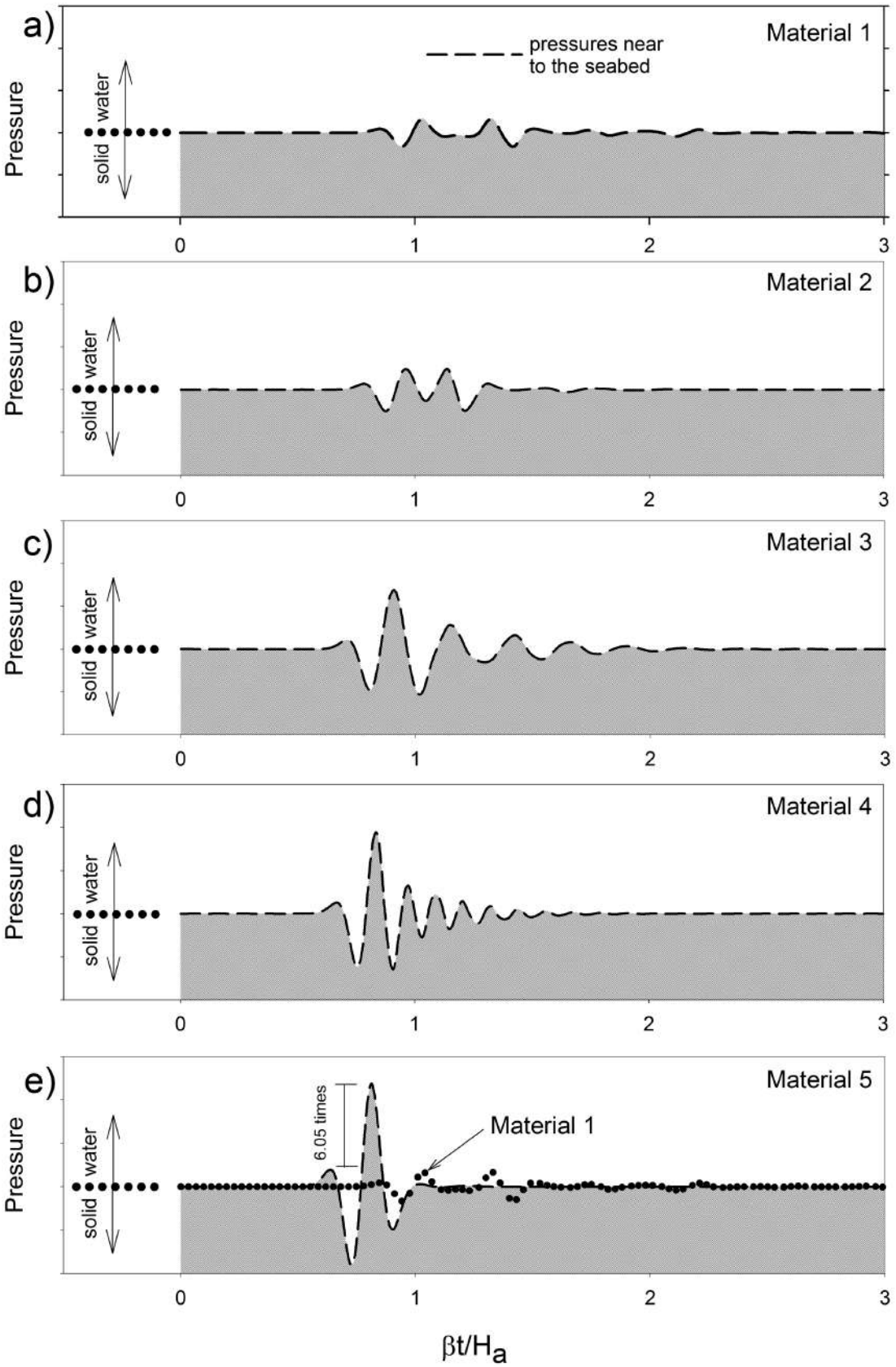

Figure 10. Maximum pressures calculated nearby the seabed for Materials 1 to 5, for normal incidence of P- waves.

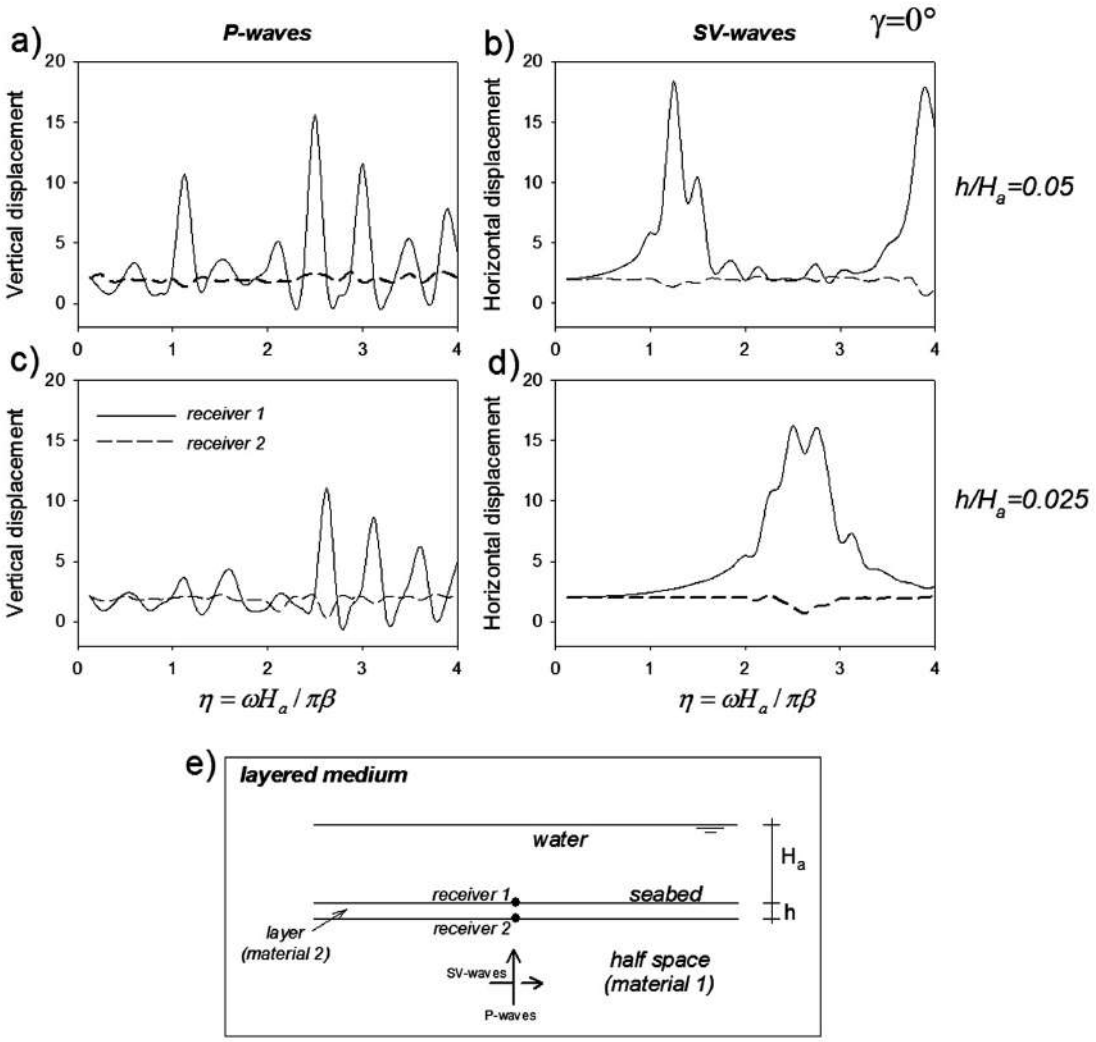

Figure 11. Vertical and horizontal amplifications due to the normal incidence of P- and SV-waves on a layered medium. The range of dimensionless frequency is $0<\eta<4.0$.

one of the first contributions on seismic amplifications is that of Trifunac (1971), where he showed amplifications around 20 times the incident wave, for the case of an SH-wave hitting an alluvial valley. It should be mentioned that the normal incidence of P- and SV-waves does not cause displacements in the horizontal and vertical direction, respectively. It is important to emphasize that the presence of a soft layer can generate large seismic amplifications, which must be taken into account in the design of marine installations.

In the case of an oblique incidence of elastic waves (P and SV), seismic amplifications are present for both components of displacement. Such amplifications can reach considerable values. Then, considering the models and materials of Figure 11, and hitting the medium with an incident angle of elastic waves of γ=30º, the seismic amplifications reach large values. For example, Figure 12c exhibits an amplification of 15.68 (at a frequency of η=3.62), which corresponds to the case of h/H_a=0.025 under the incidence of P-waves. On the other hand, the incidence of SV-waves generates amplifications of 15.11 (Figure 12h), which also corresponds to the case of h/H_a=0.025. This figure makes it clear that the oblique incidence of elastic waves can generate high seismic amplifications, for both components of displacement, although these amplifications are smaller than those obtained in the case of the normal incidence (γ=30º, Figure 11). It should be noted that Receiver 1 is again the one that reaches the largest seismic magnifications.

Finally, with the purpose of illustrating the effect that the presence of a layer has on the pressure field in the water, Figure 13 is included. Again, the models and materials used for the previous simulations were considered. But now the frequency of η=3.62 has been selected, which corresponds to the frequency where the greater amplification for previous case was obtained (Figure 12c). To display the pressure field in the water, three incident angles of elastic waves (γ=0º, 30° and 60°) were selected. The layer is formed by Material

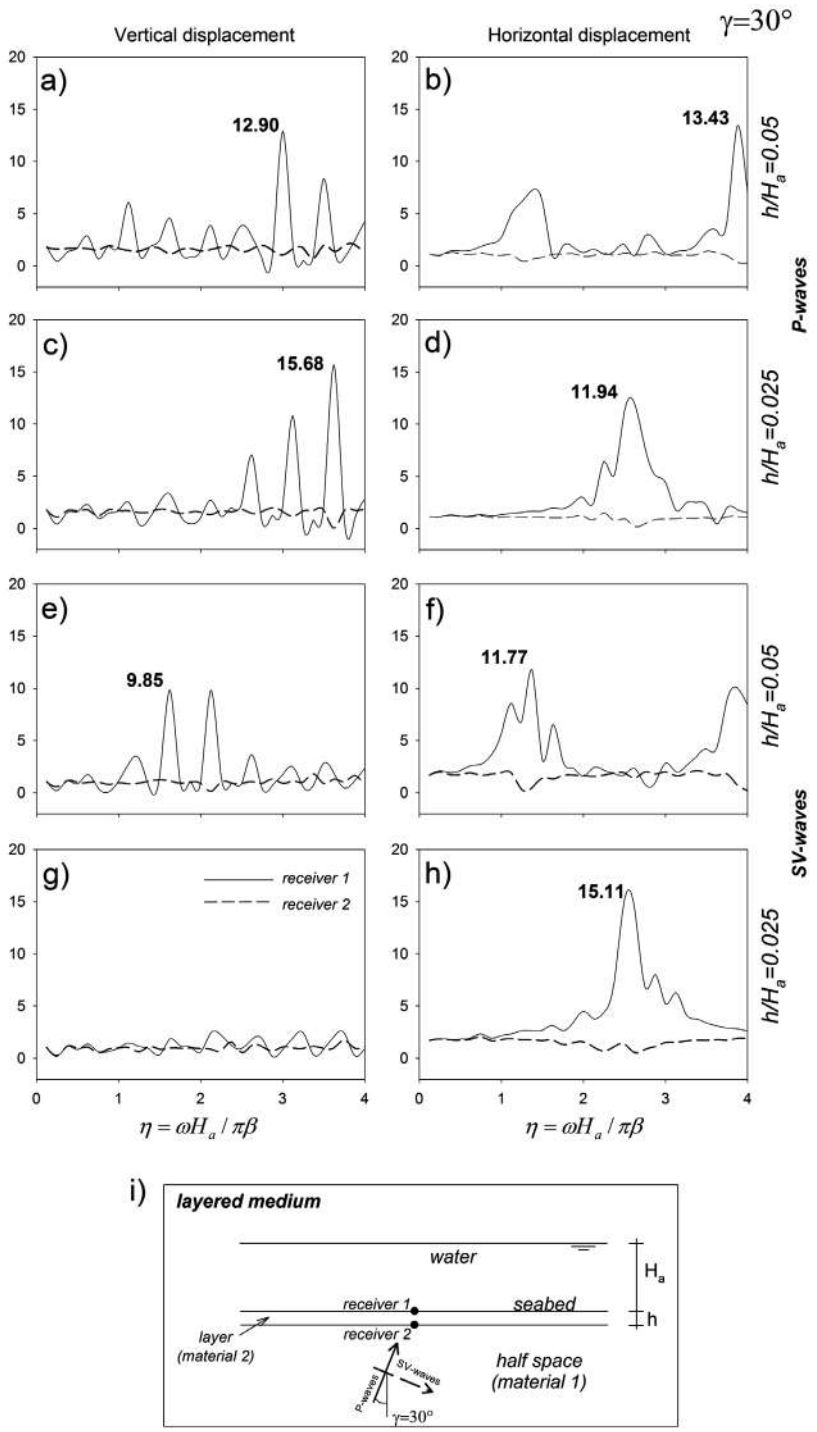

Figure 12. Vertical and horizontal amplifications due to the oblique incidence of P- and SV-waves on a layered medium. The range of dimensionless frequency is 0<η<4.0.

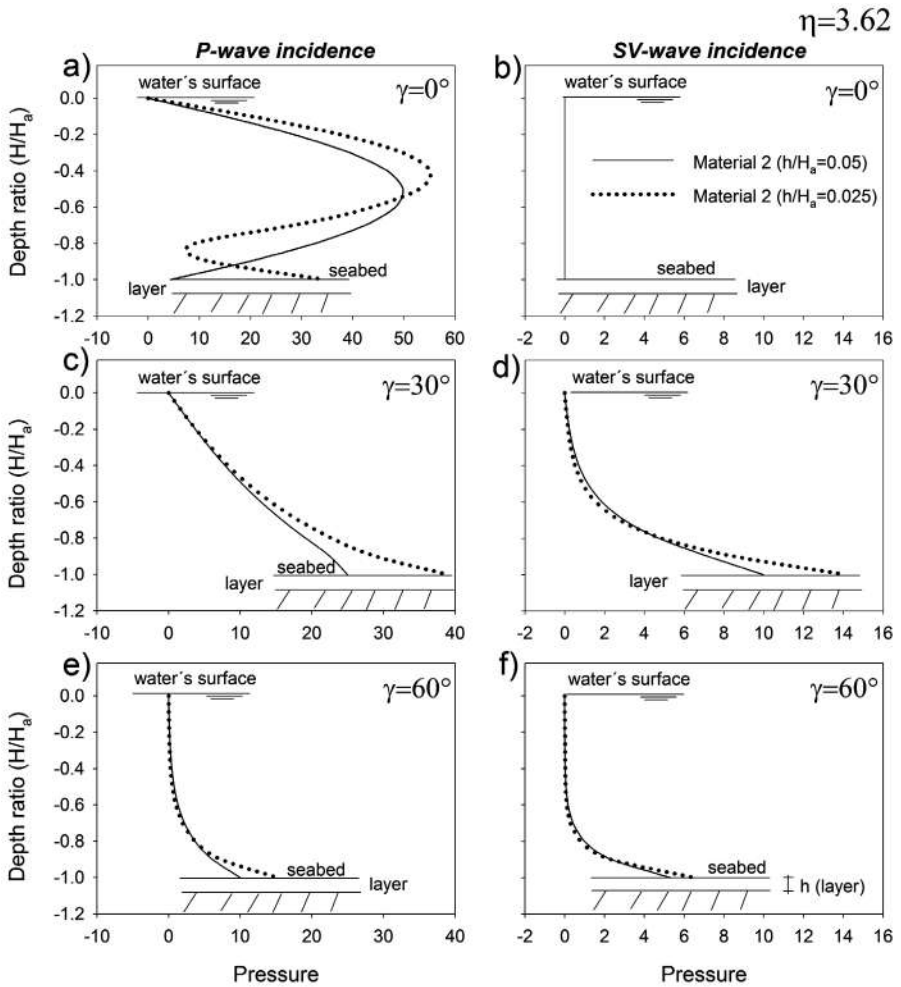

Figure 13. Pressure spectrum for layered media with various incident angles of P- and SV-waves.

2 and its thickness is given by h/H_a=0.025 and 0.05. The pressure field for the thinner layer is graphed with a dotted line, while for the thick layer a continuous line is used (Figure 13b). It should be noted that the presence of the layer causes variations in the pressures calculated throughout the water depth and mainly in the proximity of the sea bottom. It is important to emphasize that for these cases and for the frequency studied (η=3.62) greater pressures are achieved for the case of h/H_a=0.025. This result is more evident for the incidence of P- and SV-waves with an incident angle of γ=30º (Figures 13c and d). On the other hand, the incidence of SV-waves with γ=0º does not generate pressure fields in the water (Figure 13b). For the incidence of elastic waves with an angle of γ=60º, the pressure field practically remains unchanged, for both layer thicknesses.

Conclusions

This paper applies the Indirect Boundary Element Method to calculate the seismic pressure profile with the water depth due to the incidence of P- and SV-waves on the seabed. Two dimensional problems, in plane strain conditions, are considered. This formulation can be considered as a numerical implementation of the Huygens' Principle in which the diffracted waves are constructed at the boundary from which they are radiated. Thus, mathematically it is fully equivalent to the classical Somigliana's representation theorem. The results suggest that the pressure profile shows very different behaviors that depend mainly on the soil properties and the type of incident wave. Overall, the incidence of SV-waves produces a less pressure magnitude than that obtained for P-waves. In most cases

studied, the maximum pressure obtained is located nearby the seabed. This is important for the design of facilities supported on the seabed. Moreover, it has been shown that for a soil type of Material 5, seismic amplifications on the seabed are 6.05 times larger than those obtained for Material 1. Furthermore, results from the layered numerical model evidence that large seismic amplifications may be found, reaching values up to 15.57 and 18.36 times the incident P-and SV-wave, respectively. These results demonstrate the importance of adequately characterizing the type of soil where marine structures will be located.

Acknowledgments

Thanks are given to Dr. J. Efraín Rodríguez Sánchez for his useful revisions and comments, and to Instituto Mexicano del Petróleo – SENER-CONACYT Shale Gas/Oil Proyect (Y.60021).

References

Alielahi H., Kamalian M., Adampira M., 2015, Seismic ground amplification by unlined tunnels subjected to vertically propagating SV and P waves using BEM, *Soil Dyn. Earthq. Eng.*, 71, 63-79

Arockiasamy M., Munaswamy K., Swamidas A.S.J., Reddy D.V., 1983, Response of floating platforms to seismic excitation, *Eng. Anal.*, 1, 54-60.

Avilés J., Li X., 2001, Hydrodynamic pressures on axisymmetric offshore structures considering seabed flexibility, *Comput. Struct.*, 79, 2595-2606.

Banerjee P.K., Butterfield R., 1981, *Boundary Element Methods in engineering science*, Mc.Graw Hill. London.

Bedford A., Drumheller D.S., 1994, *Introduction to elastic wave propagation*, John Wiley & Sons, Chichester.

Borejko P., 2006, A new benchmark solution for the problem of water-covered geophysical bottom, *International Symposium on Mechanical Waves in Solids, Zhejiang University, Hangzhou, China,* 15-16 may 2006.

Bowles J.E., 1988, *Foundation analysis and design*, McGraw Hill, fourth edition, New York.

Dominguez J., Gallego R., 1996, Earthquake response of gravity dams including effects of porous sediments, *Proceedings of Engineering Mechanics, 2, 649-652, 1996; Conference: Proceedings of the 1996 11th Conference on Engineering Mechanics. Part 1 (of 2), May 19, 1996 - May 22, 1996; Sponsor: ASCE; Publisher: ASCE*.

Flores-Mendez E., Carbajal-Romero M., Ortiz-Alemán C., Rodríguez-Sánchez J.E., Rodríguez-Castellanos A., 2012, Modeling of fluid-solid interfaces by the Discrete Wave Number, *Kovove Mater.*, 50, 221-227.

Hamamoto T., Takahashi H., Tanaka Y., 1991, Stochastic responses of anchored flexible floating islands subjected to wind-waves and seaquakes, *Proceedings of the First International Offshore and Polar Engineering Conference,* 391-398.

Higo Y., 1997, Theoretical study on the effect of seaquakes on a two-dimensional floating body, *Proceedings of the International Offshore and Polar Engineering Conference,* 4, 480-484.

Huerta-Lopez C., Pulliam J., Nakamura Y., 2003, In situ evaluation of shear-wave velocities in seafloor sediments with a broadband ocean-bottom seismograph, Bull. Seism. Soc. Am., 93, 139-151.

Huerta-Lopez C.I., Stokoe II K.H., Valle-Molina C., Pulliam J., Roesset J,M., 2005, Modeling of Seafloor Soft Marine Sediments and Spectral Characteristics of Earthquakes Recorded on the Gulf of Mexico, *J. Offshore Mech. Arct. Eng.*, 127, 1-9.

Hwang I.T., Ting K., 1989, Boundary element method for fluid-structure interaction problems in liquid storage tanks, *J. Pressure Vessel Technol., Transactions of the ASME*, 111, 435-440.

Jang R.D., Higo Y., 2004, A study on seaquake forces acting on floating body due to seaquake by three dimensional time domain analysis, *Proceedings of the International Offshore and Polar Engineering Conference*, 492-496.

Kawase H., 1988, Time-domain response of a semicircular canyon for incident SV, P, and Rayleigh waves calculated by the discrete wave number boundary element method, *Bull. Seism. Soc. Am*., 78, 1415-1437.

Mangano G., D'Alessandro A., D'Anna G., 2011, Long term underwater monitoring of seismic areas: Design of an ocean bottom

seismometer with hydrophone and its performance evaluation, *OCEANS 2011 IEEE* – Spain.

Qian Z.H., 2012, An efficient approach for simulating seismoacoustic scattering due to an irregular fluid-solid interface in multilayered media, *J. Pressure Vessel Technol., Transactions of the ASME,* 189, 524-540.

Rodríguez-Castellanos A., Luzón F., Sánchez-Sesma F.J., 2005, Diffraction of seismic waves in an elastic cracked half-plane using a boundary integral formulation, *Soil Dyn. Earthq. Eng*., 25, 827–837.

Rodríguez-Castellanos A., Flores E., Sánchez-Sesma F.J., Ortiz-Alemán C., Nava-Flores M., Martin R., 2011, Indirect boundary element method applied to fluid-solid interfaces, *Soil Dyn. Earthq. Eng.*, 31, 470-477.

Rodríguez-Castellanos A., Martínez-Calzada V., Rodríguez-Sánchez J.E., Orozco-del-Castillo M., Carbajal-Romero M., 2014, Induced water pressure profiles due to seismic motions, *App. Ocean Res.,* 47, 9-16.

Roever W.L., Vining T.F., Strick E., 1959, Propagation of elastic waves motion from an impulsive source along a fluid/solid interface, *Philosophical Transactions of the Royal Society of London. Series A, Math. Phys. Sci.*, 251, 455-523.

Sánchez-Sesma F.J., Campillo M., 1991, Diffraction of P, SV and Rayleigh waves by topographic features; a boundary integral formulation, *Bull. Seism. Soc. Am*., 81, 1-20.

Schanz M., 2001, Application of 3D time domain boundary element formulation to wave propagation in poroelastic solids, *Eng. Anal. Bound. Elem.*, 25, 363-376.

Tadeu A., Santos J.B., Paulo F.A., 2001, 3-D wave propagation in fluid-filled irregular boreholes in elastic formations, *Soil Dyn. Earthq. Eng*., 21, 499-517.

Takamura H., Masuda K., Maeda H., Bessho M., 2003, A study on the estimation of the seaquake response of a floating structure considering the characteristics of seismic wave propagation in the ground and the water, *J. Mar. Sci. Tech.*, 7, 164-174.

Tanaka Y., Hamamoto T., Kamura H., 1991, Seaquake response of floating circular plates, *Theoret. App. Mechan.*, 40, 81-92.

Trifunac M.D., 1971, Surface motion of a semi-cylindrical alluvial valley for incident plane SH waves, *Bull. Seism. Soc. Am*., 61, 1755-1770.

Trifunac M.D., 1973, Scattering of plane SH waves by a semi-cylindrical canyon, *Earthq. Eng. Struct. D.*, 1, 267-281.

Wade R., 1996, *Practical foundation engineering handbook*, McGraw Hill, New York.

Wong H.L., 1982, Effect of surface topography on the diffraction of P, SV; and Rayleigh waves, *Bull. Seism. Soc. Am*., 72, 1167-1183.

Geofísica Internacional (2017) 56-4: 377-389

Original paper

A Simplified Method to Invert Slow Slip Events: Examples for the 2002, 2006 and 2014 events in Guerrero, Mexico

Oscar A. Castro Artola*, Arturo Iglesias, Vladimir Kostoglodov, Sara I. Franco-Sánchez, Vala Hjörleifsdóttir, Enrique Cabral-Cano and Miguel A. Santoyo

Received: February 02, 2017; accepted: August 11, 2017; published on line: October 01, 2017

Resumen

Se desarrolló un método eficiente para obtener un modelo simple de la distribución de deslizamientos en un plano de falla a partir de deformaciones estáticas observadas en mediciones continuas de GPS. Se calcularon funciones de transferencia; éstas representan el desplazamiento debido a una fuerza unitaria en un plano de falla (con una geometría predeterminada, subdividida en una malla densa de subfallas) para todas las combinaciones de estaciones y subfallas, considerando un medio estratificado. El problema directo se construye como una combinación lineal de parches elípticos de deslizamiento sobre el plano de falla y las funciones de transferencia. Para probar el método, se modelaron los eventos de deslizamiento lento (SSE, por sus siglas en inglés) de 2002, 2006 y 2014 en Guerrero, México, suponiendo que el movimiento ocurrió a lo largo de la interfase de subducción entre las placas de Cocos y Norteamérica. Se modeló la interfase de subducción como dos planos adyacentes, ambos con rumbo de 289° y por 600 km aproximadamente, y paralelos a la trinchera de América Central y con un ancho de 120 km (240 km de ancho total). El plano más somero comienza en la trinchera con un echado de 14°, mientras que el plano más profundo es sub-horizontal (2 ° dip). El plano de falla combinado está dividido en 120x48 subfallas de 5x5 km^2. Un conjunto pre-calculado de funciones de transferencia se guarda para futuros eventos, de modo que éstas sólo necesitan ser calculadas para nuevas estaciones GPS. Se encontró un buen ajuste entre las observaciones y los datos cos para todos los eventos analizados, así como consistencia con resultados reportados en estudios previos.

Key words: Slow slip events, slip inversion, GPS application, Middle America trench, subduction, Guerrero seismic gap.

Abstract

An efficient method to obtain a simple model of the slip distribution on a fault plane was developed from estimates of static offsets from continuous GPS measurements. Transfer functions were computed for the displacement due to a unit force on a fault plane (with a predetermined geometry, subdivided in a dense grid of subfaults) for all combinations of stations and subfaults, considering a layered media. The forward problem is built as a linear combination of elliptical slip-patches over the fault plane and the transfer functions between each patch and each station. To test the method, the 2002, 2006 and 2014 slow slip events (SSE) were modeled in Guerrero, Mexico, assuming that slip occurred along the subduction interface between the Cocos and North America plates. This subduction fault was modeled as two adjacent planes, both striking 289° for 600 km approximately parallel to the Middle America trench and with a width of 120 km (240 km total width). The shallower plane starts at the trench and dips 14° and the deeper plane is sub-horizontal (2° dip). The merged fault plane is segmented in 120x48, 5x5 km^2 subfaults. A pre-calculated set of transfer functions is kept for future slow slip events, so that these only need to be computed for new GPS stations. A strong agreement between observations and synthetic data was found for all analyzed events, and the results are consistent with those reported by previous studies.

Palabras clave: Eventos de deslizamiento lento, inversión de deslizamiento, aplicación de GPS, trinchera de Centro América, subducción, brecha sísmica de Guerrero.

O. A. Castro Artola*
Posgrado en Ciencias de la Tierra
Instituto de Geofísica
Universidad Nacional Autónoma de México
Ciudad Universitaria
Delegación Coyoacán, 04510
México CDMX, México
*Corresponding author: osacr.cas.art@gmail.com

A. Iglesias
Vladimir Kostoglodov
S. I. Franco-Sánchez
V. Hjörleifsdóttir
E. Cabral-Cano
Instituto de Geofísica
Universidad Nacional Autónoma de México
Ciudad Universitaria
Delegación Coyoacán, 04510
México CDMX, México

M. A. Santoyo
Instituto de Geofísica Unidad Michoacán
Universidad Nacional Autónoma de México
Morelia, Michoacán, México

Introduction

While modern computation capabilities allow the use of powerful methods (*e.g.* finite element and finite difference methods) based on data-intensive computing, the trade-off between parameterization and the non-uniqueness problem makes it difficult to find reliable solutions especially for underdetermined inverse problems. It is not always possible to add *a priori* information to constrain the inverse problem but sometimes a re-parameterization helps to reduce the non-uniqueness and allows obtaining simpler patterns. For example, measurements of deformation obtained by analyzing GPS time series have disclosed the existence of aseismic slip over active fault planes. However, frequently the number of GPS stations and the quality of data are not enough to adequately constrain the inverse problem, making it difficult to distinguish the details of slip distribution over the fault plane.

Okada's (1985 and 1992) approach is usually applied to obtain displacement at the surface due to slip on a fault plane embedded in a half-space. For example, in a global inversion scheme (Iglesias *et al.,* 2004) or a linear inversion method (Outerbridge *et al.,* 2010) it is used to get the distribution of magnitude and direction of slip. There are different approaches to retrieve slip distribution over a fault plane (*e.g.* Radiguet *et al.,* 2012, and 2016). Different methods using distinct approximations can provide equally good fits between data and synthetics with very different slip distributions (Mai and Beroza, 2000), which begs the question; which model is most realistic? To answer the question, Occam's razor principle was invoked assuming that the simplest solution is the most appropriate. Therefore, a modified version of a frequency domain scheme was used to find kinematic parameters from displacement records (Cotton and Campillo, 1995) to retrieve slip within a fault plane at depth. Re-parameterization was performed by introducing slip only on simple geometrical patches within the fault plane. This is a restriction in which slip is distributed symmetrically within each ellipse, reducing the model parameters and therefore the number of model solutions. Furthermore, the computational time and non-uniqueness of the problem are reduced by this simplification. A simulated annealing inversion procedure was used to search for the best model parameters, as this procedure has been proven effective to explore a set of models and find a good solution in a complex misfit space (*e.g.* Kirkpatrick *et al.,* 1983; Iglesias *et al.,* 2001).

The suggested approach requires a calculation of the predicted displacement at each GPS station, due to a unitary force on each sub-fault; reference to these displacements will be as transfer functions (TF). One of the main objectives of this work is to set up a library of TF in order to use them in future slow slip events in the region. As the fault plane geometry will not change with time, the functions for every station could be readily used for impending SSE.

The Guerrero Pacific coast is an over 400 km long, active seismic region, within the Mexican Subduction Zone (MSZ). This region has been intensively studied because its NW part has been defined as a mature ~100 km length seismic gap (Singh *et al.,* 1981) which has not produced any large earthquake since 1911. Several important cities in central Mexico were strongly affected by earthquakes occurred in the MSZ (*e.g.* 1911: M~7.5, 1957: 7.8, 1985: 8.0, 1995: 7.3, etc.). The first permanent GPS station deployed in the region began to operate early 1997 and at the beginning of 1998 a signal corresponding to a transient displacement was recorded (Lowry *et al.,* 2001), later attributed to a slow slip event. Since then, the GPS networks have grown gradually and have recorded slow slip events with different complexity, about every 4 years. Slow slip events could have an important role in the seismic cycle, not only because slip may have reached the seismogenic (coupled zone) part of the subduction interface (Graham *et al.,* 2015) but also because they may trigger large magnitude subduction thrust earthquakes (*e.g.* Graham *et al.*; 2014; Radiguet *et al.,* 2016).

Methodology

Forward model

A frequency domain representation was modified to model the faults kinematics assuming a discretized fault plane on which the kinematic parameters (slip, rise time and timing of rupture initiation) change from subfault to subfault (Cotton and Campillo, 1995). This approach has been successfully applied in several previous studies (e.g., Hernandez *et al.,* 2001, Castro-Artola, 2013). A static problem is considered, so there is no rise time and initiation of rupture, only cumulative slip. The displacement (u_i) on the surface due to a slip distribution within elliptical patches on a fault plane at depth is described by:

$$u_i = \sum_{k=1}^{n} g_{ki} \cdot F_k \left[x_0, y_0, sma, sme, deg, slip_{max} \right], \quad (1),$$

where F_k is the function that represents slip distribution within elliptical patches, $slip_{max}$ is the maximum slip on each patch, x_0 and y_0 are the location of the center of the ellipse within the fault plane, *sma* and *sme* are the semi-major and -minor axes, *deg* is the rotation angle and g_{ki} are the TF for each sub-fault-station pair. This formulation requires a computation of TF which represent the elastic response of the medium to an impulse for a specific geometry. To compute TF, the discrete wave-number method (Bouchon, 1981) was used in the implementation by Cotton and Coutant (1997) and a velocity model estimated from surface waves (Iglesias *et al*., 2001). The crustal velocity model chosen covers the same area as the fault plane and it reflects the Moho discontinuity as interpreted by Iglesias *et al.* (2001), which also agrees with the depth of the subhorizontal part of the modeled fault plane. We keep the TF of each sub-fault/station pair in order to reuse them in inversions of future SSE events, so if a new GPS station is installed, only the TFs of that particular station should be computed. For example, TF of CAYA station were only calculated once (for the 2002 SSE) and were re-used for the 2006 and 2014 SSEs. The fault plane was defined following the geometry used by Radiguet *et al.*, (2011) which is formed by two parts. The first plane is dipping 14° from the trench to ~120 km inland while the second is a sub-horizontal (2° from horizontal) plane from 120 to ~240 km. The fault azimuth is 289°, the rake is 90°, the length is 600 km and the combined width is 240 km. It is divided into 120x48 sub-faults of 5x5 km^2 each. Figure 1 shows the configuration of the fault plane defining the interface between the Cocos (CO) and North America (NA) plates.

The surface displacement is then calculated by the product of the transfer functions with the slip distribution defined by the elliptical shapes (Equation 1). For the forward problem the first term of seismograms in the frequency domain (zero frequency) was calculated,

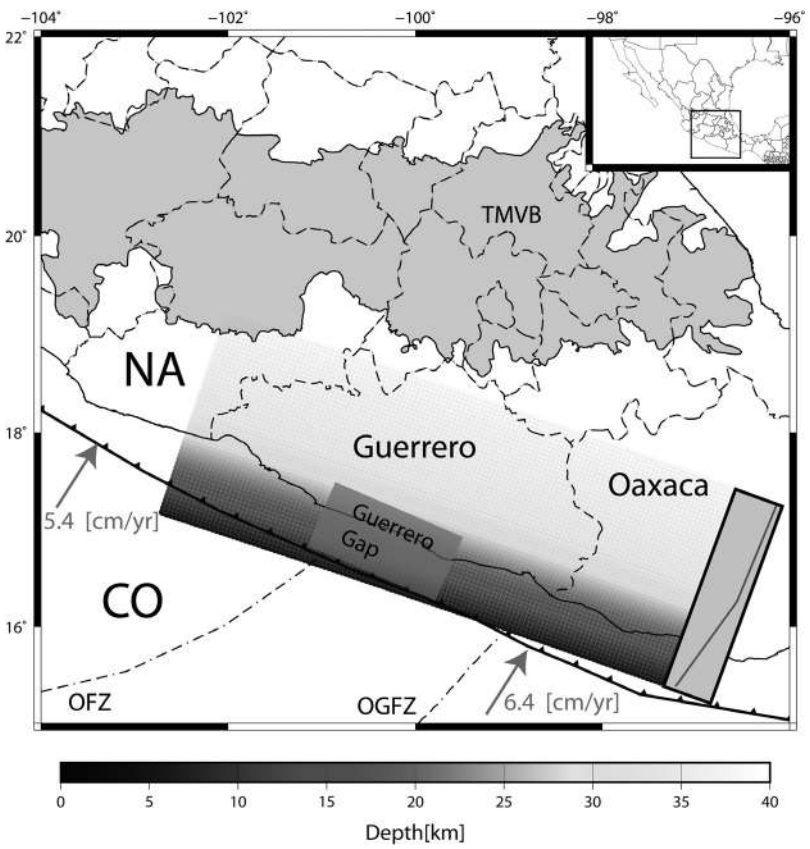

Figure 1. Map showing the discretized plane used in this study to approximate the subduction interface and the tectonic settings of the region. Red line within a black box is the vertical projection of the fault plane model. The Trans Mexican Volcanic Belt (TMVB) is the brown shaded area. The gray shaded area represents the Guerrero seismic gap. Green arrows are the Cocos (CO)-North America (NA) convergence velocity vectors from the Morvel 2010 model (DeMets *et al*., 2010). Trench is represented by black line with triangles. OFZ and OGFZ are the Orozco and O'Gorman fracture zones, respectively.

which represents the static displacement of a point on the surface due to a slip at a point at depth. The simplifications, introduced by the geometrical patch parameterization, make the problem nonlinear and this will be taken into account by the inversion scheme.

Simplified scheme: geometrical patches

A first approach to determine the slip distribution of regular earthquakes could be the use of geometrical slip patches on the fault (Vallé and Bouchon, 2004; Peyrat *et al.,* 2010; Di Carli *et al.,* 2010; Twardzik *et al.,* 2011, Castro-Artola, 2013). This approach permits to obtain a simple solution to fit the observed data. In many cases different slip distributions were reported for the same earthquake (e.g. 1999 Izmit, Turkey earthquake, Valleé and Bouchon, 2004), and sometimes results disagree from each other, not only in the details but also in the main features. Therefore, in order to achieve a solution that represents the main features of the slip a scheme that introduces one or more elliptical patches which distribute slip within them was adopted. Each ellipse has six parameters: position within the fault plane (x_0 and y_0), semi-major and -minor axes (*sma* and *sme*) which control the size of the ellipses, a rotation angle (*deg*) and the maximum slip ($slip_{max}$, see Equation 1).

Distribution of slip within the ellipses is made by introducing the maximum slip ($slip_{max}$) on the center of the ellipse and then start building bigger ellipses decreasing its maximum slip amplitude by a factor depending on the ratio between semi-major and -minor axes. The slip is able to vary between zero and $slip_{max}$, but if slip of two or more ellipses is found in the same sub-fault, then their amplitudes will be added and, therefore, could reach more than $slip_{max}$ if the inversion requires it.

Inversion scheme

A simulated annealing (SA) inversion scheme (Kirkpatrick *et al.,* 1983) was used, which is a global inversion method, in order to retrieve slip from the maximum SSE displacements observed by GPS stations. Simulated annealing methods are based on the cooling process that every mineral has to experience in order to optimize their physical properties (*e.g.* hardness, cleavage, optical properties, heat conductivity, electrical conductivity, etc). When a mineral is losing heat slow enough and for long times, then their crystals will get its optimum properties. With this analogy, an algorithm is used to guide a specific problem to find the best solution by optimizing an objective function, *i.e.* minimizing the misfit function which in the present case was the L2-norm

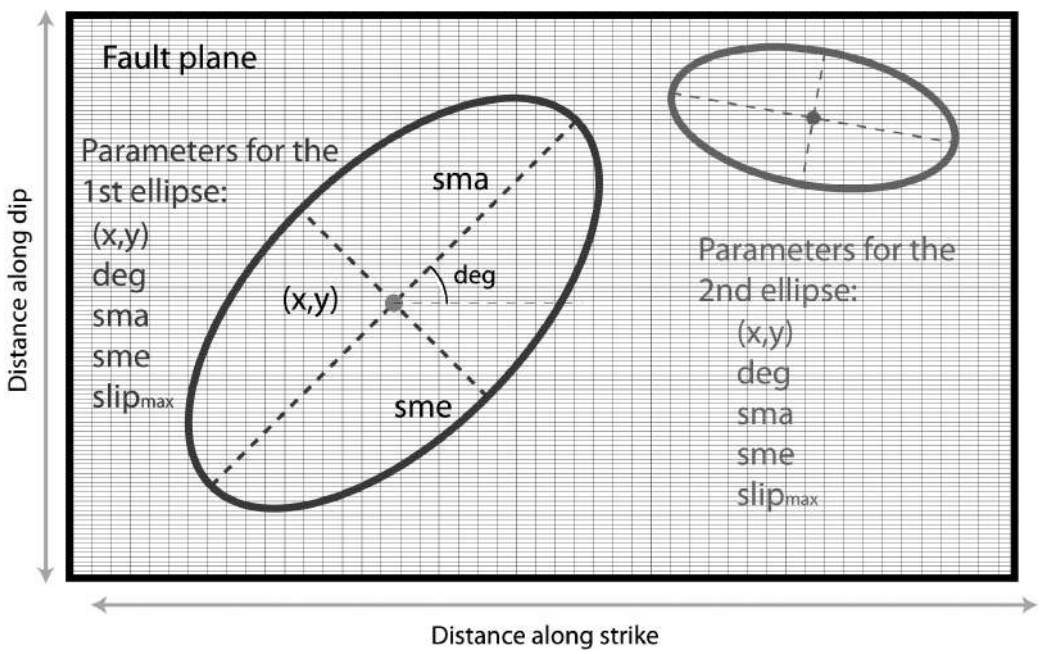

Figure 2. Description of the elliptical patches used to distribute slip. Each ellipse can be described by six parameters: position within the fault plane (x,y, deg), size: (sma,sme) and maximum slip ($slip_{max}$).

In the inversion process an initial model is evaluated, this could be either random or the lower or upper boundary values that control the process; then the parameters are modified using the SA scheme and another model is evaluated. If the misfit is smaller than for the previous parameters then the new model is accepted and the process starts again with the new model. If not, a Metropolis criteria (Kirkpatrick *et al.,* 1983) is evaluated in order to possibly accept this new worse model (Equation 2). In this criteria, a parameter to take into account is the temperature (*T,* see Equation 2), it affects the probability to test a worse model in order not to be trapped in a local minimum. This is done in order that the inversion process could be able to explore the majority of the models in the solution space. Because T is decreasing with each iteration, the probability of accepting new worse solutions (P_s, in terms of misfit difference ΔE - and temperature -T-) is lower and therefore will preferentially look for better models similar to the most recent model.

$$P_S = e^{\frac{-\Delta E}{T}}, \qquad (2),$$

A solution may be non-unique if the parameterization is not describing the phenomena accurately or if there is a trade-off between parameters. The consequence is that more than one model will fit observed data equally well. One way to minimize this problem is by decreasing the number of model parameters, so that the solution space is reduced. In this work the problem was re-parameterized by including elliptical patterns that distribute slip within them, so instead of inverting one parameter for each sub-fault (in this case would be 120x48=5760 parameters), only 6 parameters were inverted for each ellipse.

Slow slip events in Guerrero, Mexico

Tectonic settings

The largest earthquakes in Mexico occur along the subduction zone, where the Cocos plate subducts beneath the North American plate. The subduction angle varies along the trench where the northwestern part has a steeper angle while, in the state of Guerrero, the slab is almost horizontal, and in the southeast the dip angle increases again. The convergence rate between the two plates increases from NW to SE. In the northern part the CO plate converges with about 5.4 cm/year while in the southern part the slip rate is about 6.7 cm/year (Morvel 2010 model, DeMets *et al.,* 2010). There are two major fracture zones that subduct below the NA plate: the Orozco Fracture Zone (OFZ) and the O'Gorman Fracture Zone (OGFZ). Another characteristic of the subduction zone is the fact that non-parallelism exists with the volcanic arc; the Trans Mexican Volcanic Belt (TMVB) differs from most of the subduction zones in the world because it is oblique to the trench (see Figure 1).

The subduction interface of the CO and NA plates is divided into different zones. The seismogenic zone extends from 50 to 90 km from the trench and around 5 to 25 km depth, where the largest amount and the biggest earthquakes occur. Downdip, around 90 to 170 km from the trench and about 40 km depth is the transient zone, where several phenomena takes place: intermediate to small magnitude earthquakes, slow slip events, tectonic tremors and very low frequency earthquakes.

Different studies (*e.g.* Radiguet *et al.,* 2012; Rousset *et al.,* 2015) have shown low coupling values, slip in the seismogenic zone could suggest decreasing stress (Kostoglodov *et al.,* 2003); slip in front of the gap could modify the return period of large earthquakes since most of the accumulated elastic strain is released aseismically (Radiguet *et al.*, 2016). Therefore, it is very important to monitor and assess the slip balance on the plate interface in order to better understand the role of SSE in the seismic cycle and to evaluate the seismic hazard in the zone.

Slow slip events in Guerrero, Mexico

During 1995 and 1996 GPS campaign measurements on the Guerrero coast showed unusual displacements that strongly contrasted with the usual directions of motion of the GPS sites, which are almost parallel to the convergence vectors. Further analysis revealed that these displacements corresponded to the first SSE recorded in Guerrero (Larson *et al.,* 2004). In 1998 westward changes in the position of CAYA station and leveling studies identified another SSE. According to Lowry *et al.* (2001), this event released from 2 to 5 percent of the accumulated elastic energy accumulated on the transition zone of the plate interface over around six months. The estimate of equivalent moment magnitude of this SSE was M_w=6.5-6.8. Later in 2001-2002, a new GPS network recorded S-SW displacements up to 6 cm at some stations, which corresponded to a large SSE with a moment comparable to a M_w 7.5 earthquake (Kostoglodov *et al.,* 2003). Different studies share the idea that some amount of the aseismic slip invades the deepest

part of the seismogenic zone but the main slip occurs within the transition zone, down dip of the Guerrero seismic gap (*e.g.* Iglesias *et al.,* 2004; Yoshioka *et al.,* 2004; Graham *et al.,* 2015). Records at two stations, CAYA and YAIG, separated by ~120 km, showed that the SSE started simultaneously at the coast and inland, which implies that the slip was occurring on both the transient segment as well as the deepest portion of the seismogenic zone at the same time. The observed duration of this SSE is between 4 to 15 months depending on the location of the records. The event propagated towards the east (Vergnolle *et al.,* 2010).

In 2006 a third SSE was recorded in Guerrero, this time by a denser network, covering an area of 75 km along the coast by 275 km perpendicular, providing a better coverage than for previous events. The new records confirmed earlier observations where one slip was seen down-dip of the seismogenic zone (Kostoglodov *et al.,* 2010). Kostoglodov *et al.* (2010) found evidence that tectonic tremor (TT) activity followed the SSE of 2006. Although they did not find any spatial relationship, there were four bursts of TTs during the SSE. These took place around 170 km from the trench while the SSE usually goes from ~80 to 170 km from the trench. Inversion of GPS data showed a 300 by 150 km^2 slip patch parallel to the trench, between the bottom of the seismogenic to the transition zone (Vergnolle *et al.,* 2010; Radiguet *et al*., 2011; Graham *et al.,* 2015). Velocity changes associated (Rivet *et al.,* 2011) with the 2006 SSE were found using seismic noise correlations, also associated with some bursts of TTs although not all the TTs could be correlated with the SSE.

According to previous observations, there is a recurrence period of about 4-4.5 years (Cotte *et al.,* 2009) for SSE in Guerrero, so it was expected in 2009-2010 a new SSE would occur in the region. Using a dislocation model for a half-space to recover displacements at the interface, Walpersdorff *et al.* (2011) used data from 17 GPS stations to found that slip occurred mainly down-dip of the seismogenic zone to 150 km from the trench and between 10 to 25 km depth. Radiguet *et al.,* (2012) showed that the best solution requires slip at the bottom of the seismogenic zone. Another study (Zigone *et al.,* 2012) suggests that seismic waves generated by the Maule, Chile mega earthquake (M_w=8.8) triggered a second subevent. Graham *et al.,* (2015) modeled the 2009-2010 SSE as two events and showed that Coulomb stress was increased by the first event in the region where the second event occurred, and suggested a causal relationship.

Inversion results

The actual method was tested with data sets for the 2002, 2006 and 2014 slow slip events in order to retrieve the slip distribution on the fault plane. For each inversion test one, two or three ellipses were introduced and the inversion configuration parameter (number of iterations, temperature, etc.) was fixed for every case in order to compare the results with each other.

The velocities at the stations which recorded the three SSE show a consistent NE orientation pattern during inter-SSE period, and migrate SW during SSE; since this behavior does not change drastically with time, the same discretized fault plane and TF for each pair sub-fault-stations which are computed as indicated in the Forward modeling Section were used.

2002 slow slip event

The best model has three ellipses. It has the lowest misfit value and converges whether it begins in a random model or in the upper- or lower-bound. Furthermore, fits for each three component station are good and comparing the results with those obtained by other studies (Iglesias *et al.,* 2004; Yoshioka *et al.,* 2004; Radiguet *et al.,* 2012), the maximum amplitude slip patch of the present model matches approximately in extent, location and amplitude with the other three studies. A maximum slip (0.24 m) located at the deepest part of the seismogenic zone is predicted and occurs down-dip of the Guerrero gap. The slip patch with the highest slip extends parallel to the trench mainly in the sub-horizontal part of the plate, deeper than the maximum amplitude found (see Figure 3). Another patch is found near OAXA and PINO stations. Since our model only reproduces static slip, we have no information about the direction of propagation, but given the results of Franco *et al.* (2005), this elongated shape could be the signature of a trench parallel propagation.

Another interesting feature is that the smallest slip values delimit the end of the seismogenic zone. The same observation was made by the three studies mentioned above. Since surface displacements are very sensitive to the spatial extension of the slip at depth, data fit is good for stations close to the biggest patches (CAYA, ACAP and OAXA). For the vertical components fits are good for all the stations except YAIG, which was not included in the inversion because the data uncertainty was very high.

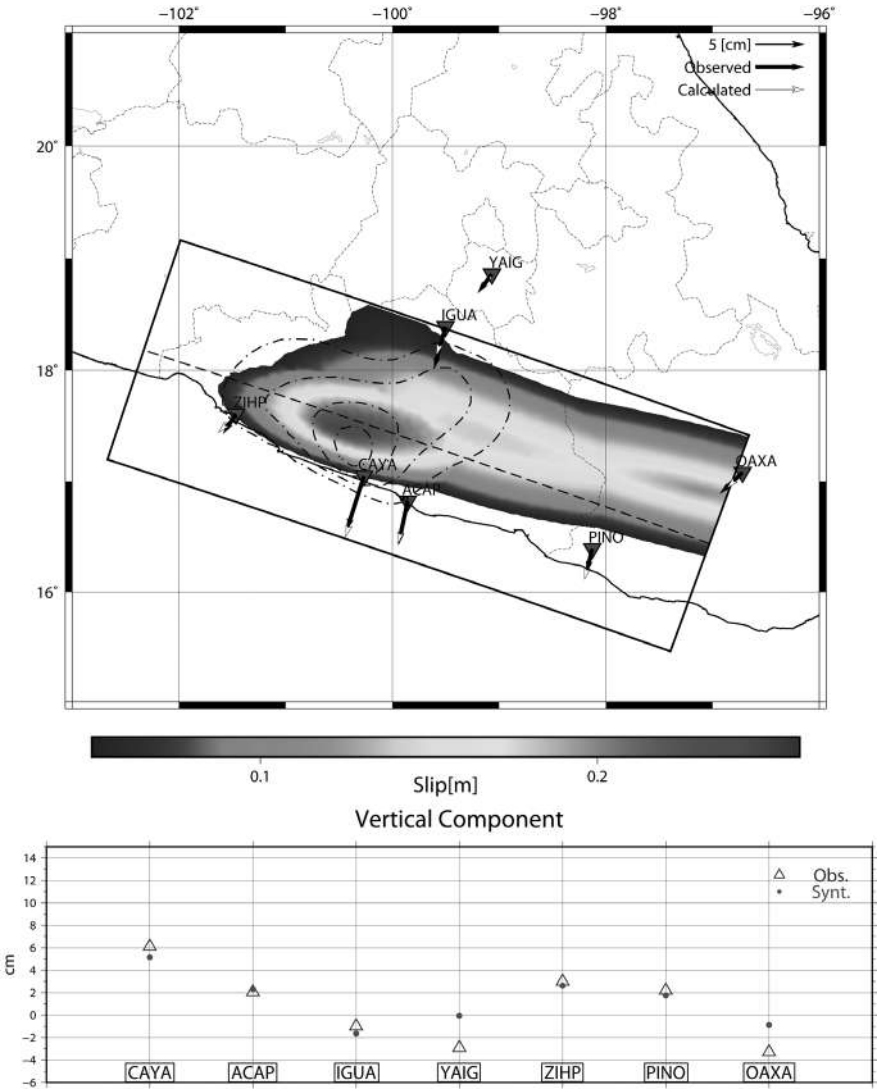

Figure 3. TOP: Slip distribution of the 2002 slow slip event in Guerrero, Mexico. Black dotted and dashed contours are for the slip distribution for 6, 10, 14 and 18 cm in Radiguet *et al*., (2012). Three slip ellipses describe the SSE. Thin and thick arrows are the calculated and observed displacements. Black arrows are the horizontal displacements. Red inverted triangles show GPS stations used. BOTTOM: Fits for the vertical component.

2006 slow slip event

For the 2006 event the difference of misfit values for all the models are less than 4% which shows the non-uniqueness of the problem. For this reason we prefer the two-ellipse model; it is the simplest of the models which converges from any initial solution and has the lowest misfit value.

This model predicts two patches perpendicular to each other and having almost the same size. The first is perpendicular to the trench and it extends from the seismogenic zone to the deepest part of the slab, the maximum slip (around 0.3 m) is located in the transition zone and in front of the Guerrero gap. The second patch is parallel to the trench and it extends on the transition zone with a maximum amplitude of around 0.25 m.

The model found by Radiguet *et al.,* (2012) has slip near the trench and the shape of the patch does not extend laterally in the slab but instead is approximately perpendicular to the trench. The biggest amplitudes coincide in space but differ in amplitude.

This two-ellipse model does not have slip near the trench, which agrees with observations in other parts of the world (Schwartz and Rokosky, 2007) and no restriction about this was needed. Data fit is comparable for tests with one, two or three ellipses and are better for stations near the coast. Fit for the vertical data is good for all stations, even for the stations far away from the biggest slip. Vertical displacements from stations in the northernmost part show good agreement, better than the horizontal components even though their amplitudes are very small.

Data from continuous GPS time series revealed that PINO station is affected by an early SSE in Oaxaca. The end of this SSE coincides in time with the beginning of the 2006 SSE in Guerrero, contributing with slip at PINO station. Since no separation of observed displacements from these two SSE is possible, PINO station was not included in the inversion process.

2014 slow slip event

An SSE was observed on the GPS network around February, 2014. Two months later, on 18 April, a M_w 7.2 thrust earthquake occurred just below the northern part of Guerrero coast (UNAM Seismology Group, 2015). Radiguet *et al.* (2016), determined that the stress changes produced by the earliest stage of the SSE triggered the April 18, earthquake, based on the slip distribution of the SSE. Permanent displacements due to this earthquake were recorded at some stations of the GPS network

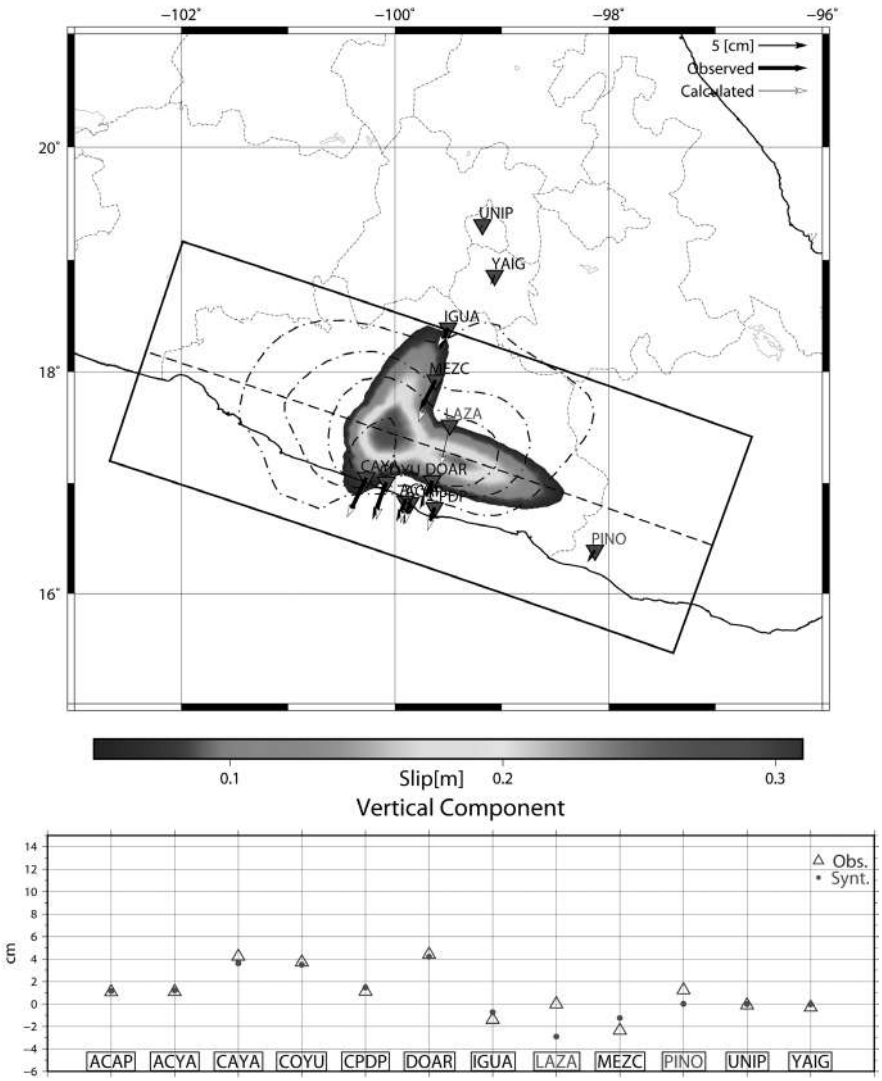

Figure 4. TOP: Slip distribution for the 2006 slow slip event in Guerrero, Mexico. Contours are the same as Figure 3. Red inverted triangles show GPS stations used. BOTTOM: Fits for the vertical component. PINO and LAZA (red letters) stations were not used in the inversion.

(PAPA, ZIHU, CAYA, ARIG and TCPN), combined with the postseismic and/or the SSE signal. The coseismic and postseismic phase of the earthquake led to bigger displacements for stations closer to the rupture zone (*e.g.* PAPA, ZIHU, CAYA, ARIG and TCPN). To remove the coseismic signal, the static displacements were calculated using the slip distribution obtained by UNAM Seismology Group (2015), and subtracted from the original data. Despite this, the postseismic effect is very challenging to model and its contribution continued to affect the data. In order to deal with this different inversion scenarios were used.

First, the parameters of each ellipse were allowed to vary freely; the resulting model fits are good but the tectonic implications have never been observed; *i.e.*, big slip near the trench or even bigger slip on the deepest portion of the fault plane. Second, the first ellipse was let to vary freely and found the best solution, then a second ellipse was added, fixing the first ellipse to the previous solution and allowing the second one to vary each parameter within half of the upper bound value of the previous ellipse, then invert for three ellipses fixing the first two to the previous solution and so on. The strategy is to incorporate more complexity into the solution with every new ellipse. The model for three ellipses was found to differ less than 3% from other models (1, 2, 4 and 5 ellipses) and was tectonically representative for what has been observed (Radiguet *et al.,* 2016).

The best model found (Figure 5) is a patch made of three ellipses with a maximum amplitude of ~40 mm and a 7.56 moment magnitude. We think that the effect of the Papanoa earthquake (coseismic and afterslip) could be responsible for the big displacements found during the inversion, so for this model it was chosen to restrict the slip not to reach depths shallower than 8 km. The first ellipse represents a big area with low amplitude (~17 mm, biggest ellipse on Figure 5) and encloses areas where previous SSEs have been observed. The second and third ellipses are smaller in area but because of the summation of the stacked ellipses they have bigger amplitudes (24 and 30 mm, respectively).

The second ellipse is down-dip of the Papanoa earthquake rupture area (dashed black polygon on Figure 5), near the limit between the seismogenic and transition zones. This patch could represent the afterslip of the Papanoa earthquake combined with the slow slip event; unfortunately, using only static displacements, it is not possible to separate the contribution of each one. Displacement at station TCPN shows a difference in direction with respect to PAPA and CAYA, which could be explained in part by the coseismic slip of the two aftershocks.

The third ellipse is the smallest one but the highest in amplitude and represents slip occurring down-dip of the Guerrero gap, within the transition zone at a depth of approximately 40 km, which confirms previous observations of slip in this region (Radiguet *et al.,* 2012 and 2016 and the ones found in this work).

Following the April 18, 2014, Papanoa earthquake, two aftershocks with magnitudes 6.4 and 6.1 occurred within the Guerrero seismic gap where TCPN (Técpan de Galeana, Guerrero; Figure 5) station is located, and therefore their coseismic signature was recorded by at least this station. Because there is not enough information to retrieve the slip distributions for both earthquakes we cannot correct for this effect and the mismatch of TCPN displacement vector could be explained for this reason.

Observed and calculated displacements show good agreement. The difference in direction of the MEZC station could be explained by the afterslip of the Papanoa earthquake as well as the occurrence of the two aftershocks. In general, vertical displacements are difficult to fit. Nevertheless, results show good agreement with the vertical component for almost all stations. The largest misfits correspond to the stations closest to the rupture zone of the Papanoa earthquake (PAPA and ZIHP, Figure 5).

Discussion

The method has demonstrated to be efficient when following our proposed inversion strategy. This means that if the inversion leaves all parameters free, the solution found might not be physically representative, but if some *a priori* constraints are taken into account, the solution will have more validity. Several strategies were followed in order to find a more general approach. Starting with the inversion from one to five ellipses, with every new ellipse the misfit should change; lower misfit values do not necessarily mean that the model found is better than the previous one. For example, if the misfit for a two-ellipse model is lower than for a one-ellipse model could be due to the fact that the second ellipse is just trying to improve the misfit for one particular station instead of improving the overall misfit. This normally happens (for models of more than one ellipse) if the extra ellipse is isolated from the others.

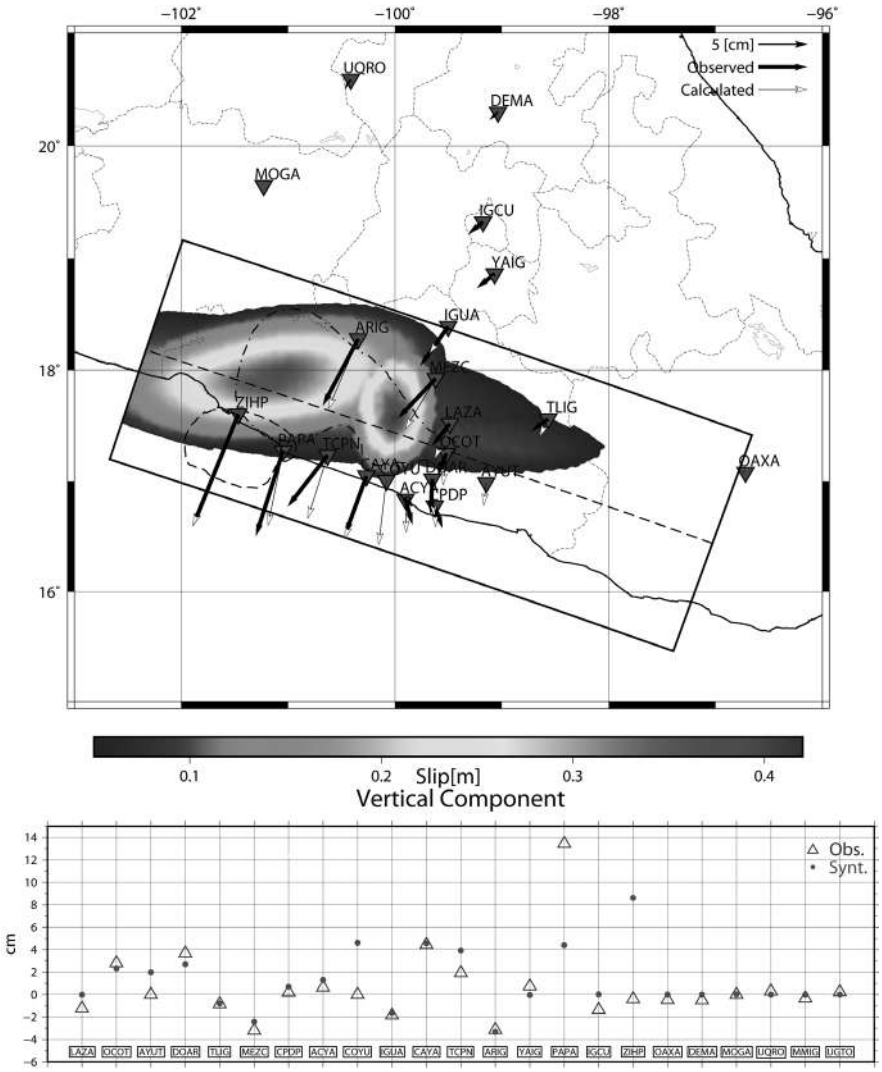

Figure 5. TOP: Slip distribution for the 2014 slow slip event. Dotted and dashed line is the isocontour from 12.5 cm from Radiguet et al., (2016). Dashed contour is the rupture area of the Papanoa earthquake. Three ellipses were necessary to fit data, one big ellipse and two small ones with the highest amplitudes. Thin and thick arrows are the calculated and observed displacements. Black arrows are the horizontal displacements. Red inverted triangles show GPS stations used. BOTTOM: Fits for the vertical component.

The number of ellipses to invert could be one of the key steps in the process. First, it is recommended to invert one ellipse and keep adding more if the latter solution does not fit data equally good for all stations. Second, with every new ellipse, the previous solution should be fixed in order to let the new ellipse fit the rest of the data.

The initial model can be chosen as a random solution or by either the lower or upper bound of the parameter values. After hundreds of tries it was found that every initial model, evaluated with the same parameters (i.e. number of iterations, temperature, lower and upper bound parameters, etc), converges to a unique solution.

The best results for all events resulted when inverting for the first ellipse and find the best model, then fix that ellipse and invert for two ellipses leaving the second one free. Then invert for three ellipses keeping fixed the first two and so on. With this, the fit can progressively improve as a new ellipse is introduced. Also, the size and biggest amplitude of the ellipses should be restricted to at least half of the size of the fault plane and with every new ellipse

the size restrictions should decrease (*e.g.*, by half the size). Another strategy is to let one ellipse to be the biggest in area but with the lowest in amplitude and let the other ellipses to be smaller but with greater amplitudes.

Conclusions

A method to obtain a first approximation for the slip patterns of SSE was developed. The present implementation of the method considers a library of TF between the GPS stations operating in the Guerrero-Oaxaca region and each sub-fault. This library could be used for futures SSE and, if a new station is deployed in the region, then only that particular TF could be easily computed. Slow slip events have occurred every ~4 years at least since 1998 in the Guerrero region and it is reasonable to expect that another SSE may develop in ~2018.

The method was tested for three major slow slip events in the Guerrero region. For all the SSEs the method found models that fits data reasonably well even with the strong restrictions (geometry of the subducted plate and the shape of slip patterns). The low number of parameters to invert (18 for the three ellipse model) make the process fast enough to test different sets of parameters within a short time (all models were found within 10 min using an Intel Xeon CPU E5-2680 v2 @ 2.80GHz processor). Another important consequence of the low number of parameters is that it reduces the non-uniqueness, nevertheless, the best solution was found when *a priori* information was introduced. Locating the biggest observed displacements and restricting parameters related to the size and amplitude of the ellipses will improve the performance of the inversion process.

The number of ellipses does not seem to represent complexity of the event, but it contributes to finding a better fit, though this does not necessarily lead to a better model. Although more ellipses help to improve the fit we found that more than three will complicate the tectonic implications of the model. At least two ellipses were needed to fit data for the 2006 SSE model, while for the 2002 and 2014 three ellipses models were the best.

This method is thus a good approach to find slip patches within a plane at depth from surface static displacements. It reduces the number of parameters and is a simple good approach to be used in the Guerrero region of the Mexican Subduction Zone.

Acknowledgements

We are grateful to all the field engineers who participated in the GPS networks installation, operation and maintenance: We specially acknowledge field operation support from J. A. Real-Pérez, L. Salazar-Tlaczani, the Servicio Sismológico Nacional field operations and IT personnel, the Servicio Mareográfico Nacional as well as Nicole Cotte from Géoazur National Seismological Service, National Tidal and Sea Level Service,, and N. Cotte from Géoazur. This work was partially supported by UNAM-PAPIT- Project IN110015 (Iglesias). Portions of the GPS network operations were supported by the National Science Foundation under award EAR-1338091 and by UNAM-PAPIIT projects IN104213-2 and IN109315-3 (Cabral-Cano). Other parts of the GPS data was operated by the Servicio Sismológico Nacional and Servicio Mareográfico Nacional. We also thank the Laboratorio de Geodesia Satelital (LaGeoS) of Instituto de Geofísica, UNAM for their support on data processing.

References

Bouchon M., 1981, A simple method to calculate Green's functions for elastic layered media. *Bull. Seismol. Soc. Am.*, 71, 4, 959-971.

Castro-Artola O.A., 2013, Esquema simplificado de inversión cinemática de la ruptura: Aplicación a sismos en México (Master thesis). Universidad Nacional Autónoma de México, Mexico.

Cotte N., Walpersdorf A., Kostoglodov V., Vergnolle M., Santiago J.A., Campillo M., 2009, Anticipating the next large silent earthquake in Mexico. *Eos, Trans. Am. Geophys. U.*, 90, 21, 181-182.

Cotton F., Campillo M., 1995, Frequency domain inversion of strong motions: application to the 1992 Landers earthquake. *J. Geophys. Res.: Solid Earth,* (1978–2012), 100, B3, 3961-3975.

Cotton F., Coutant O., 1997, Dynamic stress variations due to shear faults in a plane-layered medium. *Geophys. J. Int.*, 128, 3, 676-688.

DeMets C., Gordon R.G., Argus D.F., 2010, Geologically current plate motions. *Geophys. J. Int.*, 181, 1, 1-80.

Di Carli S., François-Holden C., Peyrat S., Madariaga R., 2010, Dynamic inversion of the 2000 Tottori earthquake based

on elliptical subfault approximations. *J. Geophys. Res.: Solid Earth,* (1978–2012), 115 ,B12), pp. 1-14

Franco S.I., Kostoglodov V., Larson K.M., Manea V.C., Manea M., Santiago J.A., 2005, Propagation of the 2001-2002 silent earthquake and interplate coupling in the Oaxaca subduction zone, Mexico. *Earth, Planets Space*, 57, 10, 973-985.

Graham S.E., DeMets C., Cabral-Cano E., Kostoglodov V., Walpersdorf A., Cotte N., Brudzinski M., McCaffrey R., Salazar-Tlaczani L., 2014, GPS constraints on the 2011–2012 Oaxaca slow slip event that preceded the 2012 March 20 Ometepec earthquake, southern Mexico. *Geophys. J. Int.*, 197, 3, pp.1593-1607.

Graham S., DeMets C., Cabral-Cano E., Kostoglodov V., Rousset B., Walpersdorf A., Cotte N., Lasserre C., McCaffrey R., Salazar-Tlaczani L., 2015, Slow slip history for the Mexico subduction zone: 2005 through 2011. *Pure App. Geophys.*, 173, 3445-3465.

Hernandez B., Shapiro N.M., Singh S.K., Pacheco J.F., Cotton F., Campillo M., Alcántara L., 2001, Rupture history of September 30, 1999 intraplate earthquake of Oaxaca, Mexico (MW= 7.5) from inversion of strong-motion data. *Geophys. Res. Lett.*, 28, 2, 363-366.

Iglesias A., Cruz-Atienza V.M., Shapiro N.M., Singh S.K., Pacheco J.F., 2001, Crustal structure of south-central Mexico estimated from the inversion of surface-wave dispersion curves using genetic and simulated annealing algorithms. *Geofísica Internacional,* México, 40, 3, 181-190.

Iglesias A., Singh S.K., Lowry A.R., Santoyo M., Kostoglodov V., Larson K.M., Mikumo T., 2004, The silent earthquake of 2002 in the Guerrero seismic gap, Mexico (Mw= 7.6): Inversion of slip on the plate interface and some implications. *Geofísica Internacional*, México, *43*, 3, 309.

Kirkpatrick S., Gelatt C.D., Vecchi M.P., 1983, Optimization by simulated annealing. *Science*, 220, 4598, 671-680.

Kostoglodov V., Singh S.K., Santiago J.A., Franco S.I., Larson K.M., Lowry A.R., Bilham R., 2003, A large silent earthquake in the Guerrero seismic gap, Mexico. *Geophys. Res. Lett.*, 30, 15.

Kostoglodov V., Husker A., Shapiro N.M., Payero J.S., Campillo M., Cotte N., Clayton R., 2010, The 2006 slow slip event and non-volcanic tremor in the Mexican subduction zone. *Geophys. Res. Lett.*, 37, 24.

Larson K.M., Lowry A.R., Kostoglodov V., Hutton W., Sánchez O., Hudnut K., Suárez G., 2004, Crustal deformation measurements in Guerrero, Mexico. *J. Geophys. Res.: Solid Earth,* (1978–2012), 109, B4.

Lowry A.R., Larson K.M., Kostoglodov V., Bilham R., 2001, Transient fault slip in Guerrero, southern Mexico. *Geophys. Res. Lett.*, 28, 19, 3753-3756.

Mai P.M., Beroza G.C., 2000, Source scaling properties from finite-fault-rupture models. *Bull. Seismol. Soc. Am.*, 90, 3, 604-615.

Okada Y., 1985, Surface deformation due to shear and tensile faults in a half-space. *Bull. Seismol. Soc. Am.,* 75, 4, 1135-1154.

Okada Y., 1992, Internal deformation due to shear and tensile faults in a half-space. *Bull. Seismol. Soc. Am.*, 82, 2, 1018-1040.

Outerbridge K.C., Dixon T.H., Schwartz S.Y., Walter J.I., Protti M., Gonzalez V., Rabbel W., 2010, A tremor and slip event on the Cocos-Caribbean subduction zone as measured by a global positioning system (GPS) and seismic network on the Nicoya Peninsula, Costa Rica. *J. Geophys. Res.: Solid Earth* (1978–2012), 115(B10).

Peyrat S., Madariaga R., Buforn E., Campos J., Asch G., Vilotte J., 2010, Kinematic rupture process of the 2007 Tocopilla earthquake and its main aftershocks from teleseismic and strong-motion data, *Geophys. J. Int.*, 182, 1411–1430.

Radiguet M., Cotton F., Vergnolle M., Campillo M., Valette B., Kostoglodov V., Cotte N., 2011, Spatial and temporal evolution of a long term slow slip event: the 2006 Guerrero Slow Slip Event. *Geophys. J. Int.*, 184, 2, 816-828.

Radiguet M., Cotton F., Vergnolle M., Campillo M., Walpersdorf A., Cotte N., Kostoglodov V., 2012, Slow slip events and strain accumulation in the Guerrero gap, Mexico. *J. Geophys. Res.: Solid Earth* (1978–2012), 117, B4.

Radiguet M., Perfettini H., Cotte N., Gualandi A., Valette B., Kostoglodov V., Campillo

M., 2016, Triggering of the 2014 Mw7. 3 Papanoa earthquake by a slow slip event in Guerrero, Mexico*. Nat. Geosci.,* 9, 11, 829-833.

Rivet D., Campillo M., Shapiro N.M., Cruz-Atienza V., Radiguet M., Cotte N., Kostoglodov V., 2011, Seismic evidence of nonlinear crustal deformation during a large slow slip event in Mexico. *Geophys. Res.Lett.*, 38, 8.

Rousset B., Lasserre C., Cubas N., Graham S., Radiguet M., DeMets C., Socquet A., Campillo M., Kostoglodov V., Cabral-Cano E., Cotte N., Walpersdorf A., 2015, Lateral variations of interplate coupling along the mexican subduction interface: Relationships with long-term morphology and fault zone mechanical properties. *Pure App. Geophys.,* 172, 10-11, 3467-3896

Schwartz S.Y., Rokosky J.M., 2007, Slow slip events and seismic tremor at circum-Pacific subduction zones. *Rev. Geophys.*, 45, 3 pp. 1-32.

Singh S.K., Astiz L., Havskov J., 1981, Seismic gaps and recurrence periods of large earthquakes along the Mexican subduction zone: a reexamination, *Bull. Seism. Soc. Am.*, 71, 827-843.

Tary J., Cotton F., Campillo M., Cotte N., Walpersdorf A., Vergnolle M., 2007, Inversion of Geodetic Data Monitoring the 2002 Silent Earthquake in the Guerrero Seismic gap: Resolution and non-Uniqueness Analysis, *Eos Trans. AGU*, 88(52), Fall Meet. Suppl., Abstract S53C-06.

Twardzik C., Madariaga R., Das S., Custodio S., 2011, Robust features of the source process for the 2004 Parkfield, California, earthquake from strong-motion seismograms, *Geophys. J. Int.*, 191, 1245–1254.

UNAM Seismology Group, 2015, Papanoa, Mexico earthquake of 18 April 2014 (Mw 7.3), *Geofísica Internacional,* 54, 4, 363-386.

Vallée M., Bouchon M., 2004, Imaging coseismic rupture in far field by slip patches, *Geophys. J. Int.*, 156, 615–630.

Vergnolle M., Walpersdorf A., Kostoglodov,V., Tregoning P., Santiago J.A., Cotte N., Franco S.I., 2010, Slow slip events in Mexico revised from the processing of 11 year GPS observations. *J. Geophys. Res.: Solid Earth* (1978–2012), 115, B8.

Walpersdorf A., Cotte N., Kostoglodov V., Vergnolle M., Radiguet M., Santiago J.A., Campillo M., 2011, Two successive slow slip events evidenced in 2009–2010 by a dense GPS network in Guerrero, Mexico. *Geophys. Res. Lett.*, 38, 15 .

Yoshioka S., Mikumo T., Kostoglodov V., Larson K.M., Lowry A.R., Singh S.K., 2004, Interplate coupling and a recent aseismic slow slip event in the Guerrero seismic gap of the Mexican subduction zone, as deduced from GPS data inversion using a Bayesian information criterion. *Phys. Earth and Plan. Int.*, 146, 3, 513-530.

Zigone D., Rivet D., Radiguet M., Campillo M., Voisin C., Cotte N., Kostoglodov V. , 2012, Triggering of tremors and slow slip event in Guerrero, Mexico, by the 2010 Mw 8.8 Maule, Chile, earthquake. *J. Geophys. Res.: Solid Earth*, 117, B9.